# A MODEL BASED STROKE REHABILITATION MONITORING SYSTEM USING INERTIAL NAVIGATION SYSTEMS

by

AMR MARZOUK
B. Sc., Arab Academy for Science and Technology, 2007

THESIS SUBMITTED IN PARTIAL FULFILLMENT OF THE REQUIREMENTS FOR THE DEGREE OF

MASTER OF APPLIED SCIENCE

In the
School
of
Engineering Science

Mechatronic Systems Engineering

SIMON FRASER UNIVERSITY

Summer 2009

# APPROVAL

**Name:** **Amr Marzouk**

**Degree:** **Master of Applied Science**

**Title of Thesis:** **A Model Based Stroke Rehabilitation Monitoring System using Inertial Navigation Systems**

**Examining Committee:**

**Chair:** **Dr. Siamak Arzanpour**
Assistant Professor of Engineering Science

**Dr. M. F. Golnaraghi**
Senior Supervisor
Professor of Engineering Science

**Dr. Mehrdad Moallem**
Supervisor
Associate Professor of Engineering Science

**Dr. Edward Park**
Internal Examiner
Associate Professor of Engineering Science

**Date Defended/Approved:** July-29-2009

# ABSTRACT

In this thesis, a low-cost rehabilitation monitoring system based on Inertial Navigation System (INS) techniques is developed. The purpose of this system is to provide practitioners with data sufficient-enough to characterise a post-stroke patient's arm motion. We propose an inertial sensor-based system to characterize the motion trajectory. The system is composed of two main components: joint angle estimation and local positioning of points of interest.

Joint angles are estimated using an Extended Kalman Filter by fusing data from different sensors. Local positioning is done using forward kinematic solutions: homogenous transformation, Denavit Hartenberg's method and dual quaternions that approximating the arm as a serial robot.

As a result, the relative joint angles and 3D positioning of points of interests on the human are calculated accurately. The data obtained prove useful for reconstructing the arm's three-dimensional motion trajectories and provide feedback to stroke survivor patients or (remotely) the rehabilitation practitioner.

**Keywords:** Inertial measurement units; Attitude and Heading Reference System; Human Arm Model; Human arm forward kinematics; Arm Joint Angle Estimation; Inertial Rehabilitation Monitoring System; Virtual Rehabilitation; Extended Kalman Filter;

*To my beloved wife and family,*

*for always being there for me*

# ACKNOWLEDGEMENTS

I would like to thank Dr. Golnaraghi for his invaluable support throughout my graduate studies so far. His guidance and strong motivation has enlightened my research path with every step. The patience he showed in hard times has been outstanding. I have learned from him not only scientific wise but also in many other life aspects.

Moreover, I would like to thank my readers, Dr. Siamak Arzanpour, Dr. Mehrdad Moallem and Dr. Ed Park for kindly reviewing my thesis.

I also would like Mr. Jacques Desplaces for the full scholarship he offered for finishing my master degree. His encouragement has given me the chance to explore and dream high.

I greatly appreciate the tremendous efforts of Dr. Neda Parnian. This research would have completed without your on-going advice and help.

In addition, I would like to thank our coop undergraduate student Sunny Sandhu for helping me develop the PCB and the arm model.

I greatly appreciate the help of the Phoenix Technologies Inc. staff for letting us use their VZanalyzer tracker vision-based motion capture system as position truth data.

I humbly thank all of my lab mates, Parvind Grewal, Masih Hosseini, Vahid Zakeri, and Hossein Mansour for helping me in one way or another. Your support and the times we spent together in the lab have been priceless.

Special thanks to senior lecturer Lakshman One, your extreme scientific background has taught me something new with every meeting we had. Furthermore, your help correcting my misunderstood scientific concepts is greatly appreciated.

I would like to thank my roommate, Khaled Hamdan for his extreme patience during my busy times. In addition, many thank to my other roommate Dr. Ali Hayek, they both have been and will always be my older brothers.

# TABLE OF CONTENTS

**Approval** ii

**Abstract** iii

**Dedication** iv

**Acknowledgements** v

**Table of Contents** vi

**List of Figures** viii

**List of Tables** xi

**Chapter 1: Introduction** 1

1.1 Literature Review 3

1.1.1 Stroke 3

1.1.2 Post-Stroke Rehabilitation 5

1.2 Research Objectives 11

1.3 Thesis Overview 12

**Chapter 2: Attitude and Heading Reference System** 13

2.1 Inertial Measurement Units 15

2.1.1 MEMS Gyroscopes 16

2.1.2 MEMS Capacitive Accelerometers 25

2.1.3 MEMS Magnetometers 36

2.2 Orientation Determination 45

2.2.1 Orientation Determination using Directional Cosine Matrix 45

2.2.2 Orientation Determination using Quaternions 48

**Chapter 3: Attitude Estimation Using Extended Kalman Filter** 51

3.1 Sensor Measurement Models 52

3.2 Euler-based Orientation Estimation Algorithm 56

3.2.1 Euler Angles Estimator Design 56

3.2.2 Estimator Experimental Results 60

3.3 Quaternion-based Orientation Estimation Algorithm 64

3.3.1 Quaternion Estimator Design 65

3.3.2 Estimator Experimental Results 71

**Chapter 4: Human Arm Biomechanical Model** 75

4.1 Model Structure and Description 76

4.2 Homogenous Transformation Method 78

4.3 Forward Kinematics using Denavit-Hartenberg's Convention 82

4.4 Forward Kinematics using Dual Quaternions ... 88
4.5 Experimental Results ... 97

**Chapter 5: Experimental Studies ... 102**

5.1 System Design Criteria ... 102
5.1.1 Body Area Network (BAN) ... 104
5.1.2 Host PC System Design ... 111
5.2 Sensor Calibration ... 113
5.3 Orientation Validation Test Setup ... 116
5.4 Position Validation Test Setup ... 120

**Chapter 6: Conclusion and Future work ... 123**

6.1 Conclusion ... 123
6.2 Future Work and Recommendations ... 125

**Appendices ... 126**

Appendix A: ADIS 16350 Inertial Sensor Specifications ... 127
Appendix B: PNI MicroMag-3 Magnetic Sensor Specifications ... 128

**References ... 129**

# LIST OF FIGURES

Figure 2.1: Drift error comparsion for different INS grades .................................. 14

Figure 2.2: AHRS using inertial sensor triads..................................................... 15

Figure 2.3: Coriolis acceleration vector illustration............................................. 18

Figure 2.4: Tuning fork analogy to measure angular rate using Coriolis force......... 19

Figure 2.5: iMEMS gyroscope from Analog Devices™....................................... 20

Figure 2.6: Raw angular rate vs. angular orientation data about x-axis ................... 21

Figure 2.7: Raw angular rate vs. angular orientation data about y-axis ................... 21

Figure 2.8: Raw angular rate vs. angular orientation data about z-axis ................... 22

Figure 2.9: Angular rate data after static bias compensation.................................. 24

Figure 2.10: Accelerometer approximated mass-spring model................................ 25

Figure 2.11: Piezo-resistive vs. capacitive accelerometers structure ........................ 27

Figure 2.12: MEMS accelerometer internal circuit (Analog Devices™)................... 28

Figure 2.13: ECEF Vs sensor coordinate frame..................................................... 29

Figure 2.14: Raw linear acceleration along x-axis with sensor module fixed ............ 30

Figure 2.15: Raw linear acceleration along y-axis with sensor module fixed ............ 30

Figure 2.16: Raw linear acceleration along z-axis with sensor module fixed ............ 31

Figure 2.17: Pitch angle measurement theory using single axis accelerometer.......... 32

Figure 2.18: Roll angle using unbiased accelerometer values ................................. 34

Figure 2.19: Pitch angle using unbiased accelerometer values ................................ 35

Figure 2.20: Forward /Reverse bias (courtesy of PNI™ Corp.) ............................... 37

Figure 2.21: Geographic, Magnetic north versus sensor heading angle .................... 38

Figure 2.22: Normalized magnetic flux density in the x-axis .................................. 39

Figure 2.23: Normalized magnetic flux density in the y-axis .................................. 39

Figure 2.24: Normalized magnetic flux density in the z-axis .................................. 40

Figure 2.25: Magnetic flux density frequency counts performing 360 loops............. 41

Figure 2.26: Heading angle output using tilt compensated magnetometers............... 43

Figure 3.1: Estimated-roll using Euler-based EKF ............................................... 60

Figure 3.2: Zoomed estimated-roll angle using Euler-based EKF .......................... 61
Figure 3.3: Estimated-pitch using Euler-based EKF ............................................ 61
Figure 3.4: Zoomed estimated-pitch angle using Euler-based EKF ......................... 62
Figure 3.5: Estimated-yaw angle using Euler-based EKF .................................... 62
Figure 3.6: Zoomed estimated-yaw angle using Euler-based EKF .......................... 63
Figure 3.7: Estimated-roll using quaternion-based EKF....................................... 71
Figure 3.8: Zoomed estimated-roll angle using quaternion-based EKF................... 71
Figure 3.9: Estimated-pitch using quaternion-based EKF .................................... 72
Figure 3.10: Zoomed estimated-pitch angle using quaternion-based EKF ................ 72
Figure 3.11: Estimated-yaw using quaternion based EKF...................................... 73
Figure 3.12: Zoomed estimated-yaw angle using quaternion-based EKF ................. 73
Figure 4.1: Human arm biomechanical model .................................................... 76
Figure 4.2: Forward kinematics using Homogenous Transformation...................... 78
Figure 4.3: Arm model initial condition............................................................ 79
Figure 4.4: Arm model decoupled joints with assigned DH frames........................ 82
Figure 4.5: Matlab robotics toolbox model........................................................ 87
Figure 4.6: Illustration of the dual angle between two vectors ............................... 89
Figure 4.7: Input angles for comparing DH and DQ algorithms' performance......... 94
Figure 4.8: Simulation 3D position trajectory.................................................... 95
Figure 4.9: Add/Subtract computational cost for DH vs. DQ algorithms ................ 95
Figure 4.10: Multiplication computational cost for DH vs. DQ algorithms............... 96
Figure 4.11: EKF performance on elbow-joint positioning (x-axis)......................... 97
Figure 4.12: EKF performance on elbow-joint positioning (y-axis)......................... 98
Figure 4.13: EKF performance on elbow-joint positioning (z-axis) ......................... 98
Figure 4.14: EKF performance on a 3D pitch motion trajectory.............................. 99
Figure 4.15: EKF performance on a 3D yaw motion trajectory .............................. 99
Figure 4.16: Error chart for local positioning (x-axis)......................................... 100
Figure 4.17: Error chart for local positioning (y-axis)......................................... 101
Figure 4.18: Error chart for local positioning (z-axis) ......................................... 101
Figure 5.1: Total hardware system structural design.......................................... 103
Figure 5.2: Sensor communication network following the Star topology ............. 104
Figure 5.3: Sensor module internal circuitry structure ........................................ 107

Figure 5.5: PCB implementation of an integrated sensor module ......................... 108
Figure 5.4: Sensor module PCB CAD model.................................................... 108
Figure 5.6: Main controller modular circuit structure ......................................... 109
Figure 5.7: 16-Bit SPI word using 2x8-bit sequences ........................................ 111
Figure 5.8: Wireless communication to the host PC using Zigbee™ .................... 111
Figure 5.9: LabVIEW implemented Graphical User Interface (GUI).................... 112
Figure 5.10: Sensor Module in Equilibrium state ............................................... 114
Figure 5.11: Five DOF arm CAD model .......................................................... 115
Figure 5.12: Implemented arm model used in experimental tests .......................... 115
Figure 5.13: Microstrain GX-2 AHRS system.................................................... 116
Figure 5.14: Roll testing in different orientations ............................................... 116
Figure 5.15: Pitch testing in different orientations .............................................. 117
Figure 5.16: Yaw testing in different orientations............................................... 117
Figure 5.17: Heading angle without hard-iron disturbances .................................. 118
Figure 5.18: Heading angle with hard-iron disturbances (iron handle) ................... 118
Figure 5.19: Heading angle with hard-iron disturbances (wrist watch)................... 118
Figure 5.20: Implemented sensor mounted on reference sensor............................ 119
Figure 5.21: Visualeyez motion tracking system by Phoenix Technologies ............ 120
Figure 5.22: Active markers placed on the arm model for position validation......... 121
Figure 5.24: Yaw motion positioning validation test........................................... 122
Figure 5.23: Pitch motion positioning validation test .......................................... 122

# LIST OF TABLES

Table 2.1: Angular rate data-statistics summary ................................................ 22

Table 2.2: Acceleration data statistics summary ................................................ 31

Table 2.3: Roll and pitch angles' statistics calculated using accelerometers ........... 35

Table 2.4: Magnetometer data statistics summary.............................................. 40

Table 2.5: Yaw angle  statistics summary ......................................................... 43

Table 2.6: Sensor methods for obtaining Euler angles......................................... 44

Table 3.1: Error analysis for the Euler-based EKF estimator results ..................... 63

Table 3.2: Error analysis for the quaternion EKF estimator results ....................... 74

Table 4.1: Joint angles description for the human arm model............................... 77

Table 4.2: Human arm model DH link description table...................................... 83

Table 4.3: Dual angles extracted from DH table ................................................. 91

Table 4.4: Comparison between Dual Quaternion and DH algorithms .................. 94

# Chapter 1: INTRODUCTION

Rehabilitation involves a variety of medical cases such as athletic and other sports-related injuries, post-accident rehabilitation. The number of inpatient rehabilitation clients in Canada has grown from approximately 17,700 subjects in 2002 to almost 32,700 in 2008 [1]. These rapidly growing numbers led to the formation of a number of research teams and attracted the attention of a wide variety of companies from many interdisciplinary research areas and interests. Their main aim is develop new technologies, to help stroke survivors to practice their daily exercises in a more efficient way either at home or in clinics.

Since the most preferable rehabilitation method for both youths and elderly subjects is non-invasive therapy, professional physiotherapists and practitioners have been using state-of-the art technologies for rehabilitation such as dedicated interactive virtual reality environments, rehabilitation robots and others. However, the relatively high cost of specialized rehabilitation systems limits their use in small rehabilitation centres and for personal home care.

Other aspects being considered include how system complexity and set-up time proportionally affect system efficiency, especially when the system is used on multiple subjects, with system tuning and modification needed for each individual subject. Consequently, a number of institutions and clinics have been using commercial video gaming consoles on a regular basis for patient stimulation in rehabilitation exercises. Some common low-cost systems are the Nintendo-Wii and Sony's Play-Station 3 because of their human-machine interactive nature, which needs the user to move in specific motion trajectories in order to accomplish progress in the virtual gaming environment. As a result of performing experiments, a number of post-stroke patients' progress have been noticed [2], proving that rehabilitation using interactive gaming and virtual environment interaction is more efficient than other traditional methods.

Furthermore, because these systems were built without taking their usage for rehabilitation purposes into design considerations, research results showed some downsides. The major downsides are that safety-related hazards and over excitement, especially for post-stroke patients, which can lead to even prohibition of some rehabilitation subjects of such gaming consoles. Other disadvantages include the fact that the required exercises cannot be pre-programmed for each individual patient according to his or her specific case, thus reducing the rehabilitation progress process.

The goal of this research is to develop an integrated low-cost motion monitoring system effective enough for post stroke rehabilitation. This thesis deals only with the human arm modelling and motion trajectory calculation. The scope of the research covers the kinematic modelling of the arm, numerical simulation of the system, as well as the design, development and implementation of an experimental sensory system as a proof of concept.

## 1.1 Literature Review

### 1.1.1 Stroke

The history of stroke definition and classification dates back to around 300 BC. Hippocrates, a famous Greek physician and referred to as “the father of medicine,” recognized the condition of apoplexy. In Greek, apoplexy roughly means “struck by lightning,” and the term was used to denote the sudden falling of a human being and the remaining of the person motionless on the ground. Physicians and doctors from the time of Hippocrates used the same term until the first half of the twentieth century [3], when the term CVA (short for Cerebro-Vascular Accident) started to emerge. The currently common definition of stroke is “the neurological deficit of cerebro-vascular cause that persists beyond 24 hours or is interrupted by death in 24 hours,” as stated by the World Health Organization, 1978 [4].

Among the most common natural causes of death, stroke takes second place worldwide after ischemic heart disease. In addition, it is considered the main cause of disabilities [5]. Stroke can be classified into two main categories: ischemic stroke and haemorrhagic stroke [6].

Ischemic stroke is a classification of a brain-related stroke caused by a decrease in the oxygen concentration in the blood stream feeding the brain tissue. This deficiency results in malfunction of the brain part affected by the lack of oxygen in the blood stream in that area. This can eventually affect the brain tissue, with long-term malfunctions, and can cause permanent damage to motor control functions.

Haemorrhagic stroke, also called Blood Pool, is the second major type of stroke. It is characterized by the accumulation of blood in a specific spot within the human skull. The accumulating blood in the brain causes pressure on some of the brain tissues, causing malfunctions.  It is also known that many haemorrhages actually start as ischemic strokes. The blood flow disruption causes pressure differences, resulting in blood outbreaks in other areas.

Stroke effects may vary widely according to subject. However, almost all stroke subjects require post-stroke attention and care whether in healthcare centres or in their homes. Statistics show that the median rehabilitation period in specialized facilities is about one month. This period has been almost constant between the years 2002 and 2008. Furthermore, in many cases the patients are advised by their doctors to seek medical care and to practice regular exercises on a predetermined basis.

The following section discusses the state-of-the-art systems used for post-stroke rehabilitation and the incorporation of new technologies in rehabilitation assistance, emphasising the new products being currently used.

### 1.1.2 Post-Stroke Rehabilitation

Rehabilitation for stroke survivors after hospitalization has to be either supervised by professional or a trained person (can be a family member) who is able to use rehabilitation- assisting devices efficiently. The systems and exercises performed by each patient have to be designed specifically for this purpose for eventually achieving positive outcomes [7]. This thesis concentrates on the rehabilitation of the upper extremities.

Patients suffering from motor malfunctions and gait instability following stroke have difficulties maintaining posture and performing stable motion trajectories with their limbs. Almost no stroke survivors can be adequately helped back to their normal lives by the use of medications only. Drug treatment approaches have not been very successful in stroke rehabilitation, a result paving the way for finding an alternative solution approaching the problem of motor function rehabilitation. This section investigates the various state-of-the-art technologies that are currently being used to provide the proper facilitation of monitoring, evaluating, and even governing the trajectory motion of the human arm during rehabilitation exercises.

Rehabilitation systems can be classified into three main categories according to the technologies used in each: vision-based, mechanical-based and inertial measurements -based systems. Nevertheless, fusion between them often takes place for achieving better system performance.

#### 1.1.2.1 Vision Based Rehabilitation Systems

This category of systems depends mainly on vision systems using cameras for either two-dimensional or three-dimensional positioning – if multi-cameras are available. Prange and Krabben [8] developed a one-camera-based rehabilitation interface for upper extremity motor functions. Their system captures a live feed picture of the subject's arm and displays it overlaid on the gaming interface. Because of the presence of the physiological stimuli, this method showed faster progress than regular rehabilitation methods. In this case, the stimulus is the gaming interface, where the patients can interact with a simple time-constrained bird-catching activity.

Mumford and Duckworth [9] built an accurate positioning system by using a high-resolution stereovision camera and a 40-inch TV set. The bi-camera system calculates the three-dimensional position of a predetermined marker shape fixed on top of a cylindrical tube-shaped object that the subject has to be holding while moving throughout the exercise. One of the main drawbacks of their system is that the subject undergoing rehabilitation is constrained within the visual field of the cameras. Another drawback is the cost of the system, which includes a high-resolution stereo camera systems and a 40-inch TV mounted horizontally acting as the visual feedback stimulus.

Furthermore, Cameirao and Badia [10] incorporated a vision camera with fibre optic-based flex sensors mounted on the hand in the form of a glove. Their Rehabilitation Gaming System (RGS) calculates the two-dimensional position of colour patches mounted on both the forearm and the upper arm. After that, the software algorithm calculates the joint angles between the colour patches. The fibre optic-based flex sensors are used for measuring finger flexion of the hand. Thus, the motion trajectory by means of sensor fusion can provide the motion pattern of the patient and provide visual feedback on the computer screen. Their developed game software asks the subject to move his or her arm in order to perform grabbing exercises. Some disadvantages of their proposed system are lack of accuracy (joint angle error is about 11 degrees) and the use of only one vision camera, which results in estimation of only the two-dimensional position of the mounted colour patches.

Attygalle and Duff [11] used the famous Nintendo Wii-remote gaming device as an infrared camera. Each Wii-remote (also called Wiimote) has an IR camera system that can track up to six moving infrared active markers. In the original game console, the Wii-mote tracks the three-dimensional position of a set of two groups of infrared light-emitting diodes (IR-LEDs) which the user has to mount on top of the TV set (mistakenly called Sensor-Bar). Their research team equipped the Wiimote itself with an IR-LED array placed around the IR-camera. In this case, the camera would be able to see not only active markers but also passive markers. The system requires the rehabilitation subject's arm to be tagged with a marker mounted on the forearm, which the cameras track by means of IR reflections emitted by the IR-LEDs mounted around the camera. In addition, they provide the subject undergoing the exercise with a force sensor shaped as a cone, with green and red LEDs mounted on top for grasping force visual feedback.

This arrangement would insure that the subject would not only reach the required position but also achieve grasping requirements. Since their system needs the subject to be sitting in an upright position facing the camera system tracking only one marker, the system can be manipulated to give good results by leaning forward to minimize the effort required.

#### 1.1.2.2 Mechanical Based Rehabilitation Systems

These systems depend on the use of mechanisms to sense, control and provide force feedback in the rehabilitation process. Balasubramanian and Wei [12] are developing a robot arm that acts as an exoskeleton-supporting robot to the rehabilitation patient. A computer that in turn takes the commands from the relevant physiotherapist or practitioner controls the robotic exoskeleton arm. The exoskeleton robot facilitates repetitive motion trajectories and can be used for daily rehabilitation exercises for which the patient needs assistance constantly. Nevertheless, haptic force feedback robots like RUPERT tend to be unstable within low-speed motions and trajectories. This limitation introduces a relatively dangerous hazard because it leads to sudden overshooting of the system that is actuated by strong pneumatic muscle actuators. In addition, the physiological side of having an older rehabilitation subject attach an arm into a strong mechanical exoskeleton might cause a barrier that slows down his or her rehabilitation progress.

Dellon and Matsuoka's mechanical system handles the safety problem mentioned previously [13]. Their system simply depends on dissipating the energy exerted by the trainee or the rehabilitation subject. However, since their system does not have any type of actuation, the weight of the robot might present difficulties, especially for old and young patients as well as subjects in weak stages of their rehabilitation.

#### 1.1.2.3 Inertial Measurements Based Systems

In inertial measurement systems, inertial measurement units (IMUs) are used. An inertial measurement unit is composed of tri-axes accelerometers and tri-axes gyroscopes. The addition of tri-axial magnetometers changes it.to an Attitude and Heading Reference System.

Pyk and Wille [14] have developed an integrated system that uses a combination of inertial, pressure and flex sensors. Their set-up calculates roll, pitch and yaw angles using accelerometers and magnetometers. The pressure sensor calculates the air pressure inside a bottle held by the rehabilitation subject to assess gripping ability. The main disadvantage is that using accelerometers only to measure tilt angle cannot differentiate between accelerations due to tilt with respect to earth's gravitational acceleration and linear accelerations by the hand movement.

Zhou, Stone and Hu [15] used multiple inertial sensors to obtain Euler angles and, thus, determine shoulder, elbow and wrist positions using Lagrangian optimization. Furthermore, Lanfermann and Willmann from Philips Research [16] developed a wireless network that combines data acquired by two inertial measurement units. Their system adds the computation of posture that is familiar to physiotherapists. Then, all data is displayed on a user-friendly graphical interface that displays sensor data as well as the computed biomechanical outputs.

Other research groups have also been working on posture estimation using inertial sensors for applications other than rehabilitation. Junker and Amft [17] used similar estimation methods for gesture recognition in order to understand basic human motion behaviour during daily activities.

In addition, computer animation and the movie-making industry in the twenty-first century rely on inertial as well as vision motion capturing techniques. Rotenberg  Per Slycke and Veltnik [18] have developed a complete human motion (Xsens-Moven) capturing system that is now being used by many computer animation and movie-making studios as well as for rehabilitation and kinesiology research.

Literature concerning inertial-based rehabilitation systems shows that the main used concept for posture estimation for rehabilitation is mainly built upon three-dimensional joint angle estimation. For many years, the de facto standard for the angle estimation using inertial measurement units has been established using the Extended Kalman Filter (EKF) algorithm. The composition and the theoretical basis of the algorithm will be discussed in detail in later chapters. This estimation method using low -cost MEMS sensors for rehabilitation research encouraged the ideas of tele-rehabilitation and home-based-rehabilitation, as discussed by Zheng and Black [19].

The focus of this research is to develop and deploy an inertial-based rehabilitation system characterized by low-cost and easiness of set-up as well as low power consumption. After the joint angle is estimated, the resulting data are fused with the human arm biomechanical model to acquire local position information. Description of each section of the developed system will be discussed in later chapters.

## 1.2 Research Objectives

The primary objective of this research thesis is to characterize the human arm motion in 3D space (orientation and local position) to facilitate post-stroke rehabilitation monitoring and assessment. These estimated kinematic parameters can be used in the future to evaluate the performance of a stroke survivor doing his daily-required exercises advised by a practitioner. Moreover, a template motion trajectory can be performed by a professional physiotherapist, saved then compared to the motion trajectory made by the patient.

The focus is on developing an inertial sensor network to obtain the arm-joint angles as well as 3D position of points-of-interest on the arm. Two Extended Kalman Filters are studied and implemented to estimate orientation angles combining triads of accelerometers, gyroscopes and magnetometers. These Extended Kalman Filters act as an Euler angles estimator and an orientation quaternion-based one.

Previous research data described the local position of given points based on inertial sensors. Results proved that positioning data calculated directly by double integrating accelerations are stable for only tens of seconds, showing the need for external aids (i.e. GPS, stereovision, etc.). In order to minimize these rapid growing errors, a biomechanical model is developed to obtain local position by applying forward kinematics methods given the by the EKF-estimated angles.

As a proof of concept, the estimated orientation angles are compared with those obtained by a manufacturer-calibrated Attitude and Heading Reference System (Microstrain GX-2). In addition, the estimated local positioning information is analyzed relative to the output of a vision-based tracking system manufactured by Phoenix Technologies Inc.

## 1.3 Thesis Overview

In Chapter 1, human stroke and its types are introduced. Then, a summary of the literature review of the state-of-the-art technologies applied in stroke rehabilitation is presented. Finally, the arm kinematic model is discussed with respect to previous research in this area.

Chapter 2 introduces the different sensors being used in this research and describes their theory of operation and structure. Orientation determination mathematics is shown in a comparative theme between different methodologies.

In Chapter 3, the sensor fusion algorithm is introduced. The basic non-linear Extended Kalman filter algorithm is applied to estimate joint angles of the arm. The algorithm's structure, system state model and measurement model are discussed in detail.

Chapter 4 emphasizes the development of the human arm kinematical model. The forward kinematics of the five degrees of freedom model is done using three methods: homogenous transformation, Denavit Hartenberg's and Dual Quaternions.

Chapter 5 explains the experimental designs used to prove the mathematical concepts derived during the research. The designs show a simple sensor network using embedded software. The embedded system transmits data wirelessly to a host PC for further more complex computations like orientation estimation and local positioning.

Chapter 6 presents the conclusions, describes future work, and provides recommendations for further research.

# Chapter 2: ATTITUDE AND HEADING REFERENCE SYSTEM

In many applications, inertial sensors are used for angle determination. The invention of inertial measurement units (IMUs) was intended for use in navigation systems for military applications. Based on navigation theory, an inertial navigation system is built using an inertial measurement unit, aided by external position determination means if necessary. Furthermore, by adding magnetometers an IMU is called an Attitude and Heading Reference System (AHRS).

In theory, position can be calculated directly by the double integration of linear acceleration readings from the accelerometers. Nevertheless, the main drawbacks of using inertial measurement sensors for position tracking are the size and double integration, which introduces errors due to the accompanying constants. One reason of errors due to integration is due using discrete integration methods that ignore some of the areas under the analogue signal curve .This increasing error propagation with respect to time restricts accurate position estimation to limited time intervals without the use of an external correction from other positioning systems, like Global Positioning Systems (GPS). As a result, IMUs are known for their extremely high cost (>$100,000), reflecting their accuracy and precision grading as shown by Foxlin [20] shown in Figure 2.1.

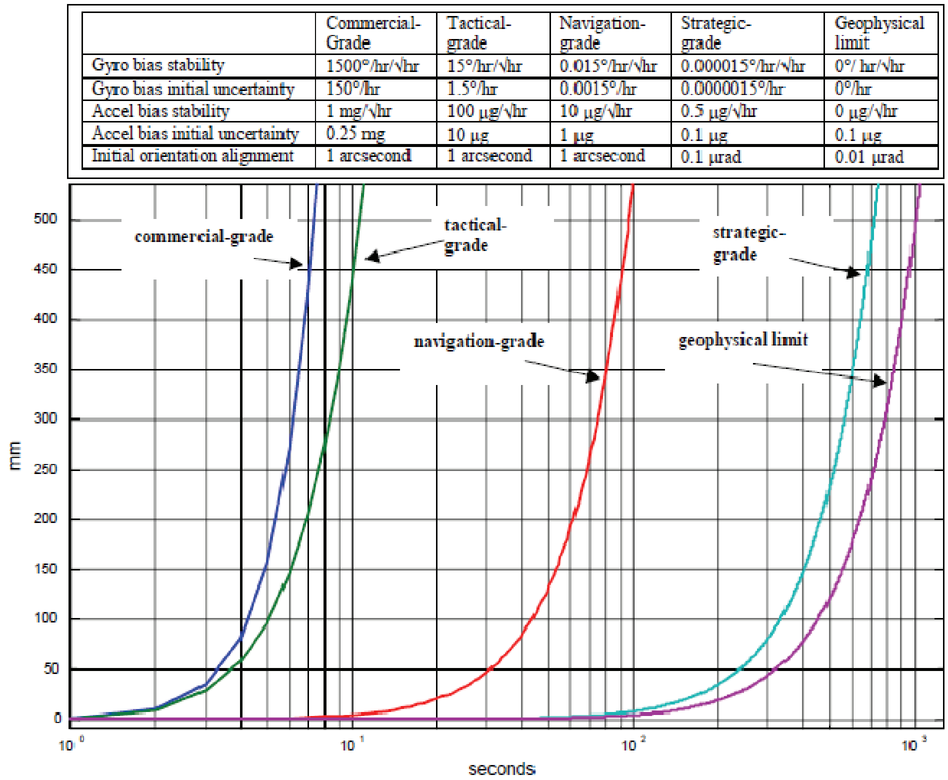

| | Commercial-Grade | Tactical-grade | Navigation-grade | Strategic-grade | Geophysical limit |
|---|---|---|---|---|---|
| Gyro bias stability | 1500°/hr/√hr | 15°/hr/√hr | 0.015°/hr/√hr | 0.000015°/hr/√hr | 0°/ hr/√hr |
| Gyro bias initial uncertainty | 150°/hr | 1.5°/hr | 0.0015°/hr | 0.0000015°/hr | 0°/hr |
| Accel bias stability | 1 mg/√hr | 100 μg/√hr | 10 μg/√hr | 0.5 μg/√hr | 0 μg/√hr |
| Accel bias initial uncertainty | 0.25 mg | 10 μg | 1 μg | 0.1 μg | 0.1 μg |
| Initial orientation alignment | 1 arcsecond | 1 arcsecond | 1 arcsecond | 0.1 μrad | 0.01 μrad |

Figure 2.1: Drift error comparsion for different INS grades

In the following section, the basic structure for inertial measurement units and the included sensors will be discussed.

## 2.1 Inertial Measurement Units

Early inertial measurement units were composed of purely mechanical sensors for military applications. Previously, an aircraft's attitude indicator (ADI) or artificial horizon was built using only a gyroscope to determine the three Euler angles, Roll, Pitch and Yaw. The pilot or the navigation system to determine the heading and tilt angles uses the gyro-stabilized platform controlling the artificial horizon. Also of interest is the fact that attitude indicators are now being substituted by today's attitude and heading reference systems that this research uses for joint angle determination.

The semiconductor revolution in the 1950s led to rapid developments in Micro-Electro Mechanical Systems. This advancement in turn revolutionized the invention of miniature gyroscopes, accelerometers and magnetometers. This new technology allowed manufacturers to enable the mass production of low-cost low-power miniature attitude and heading reference system units, such as the unit used for this project. A basic structure of an AHRS system is shown in Figure 2.2, where tri-axes accelerometers, gyroscopes and magnetometers are integrated for attitude angle calculation.

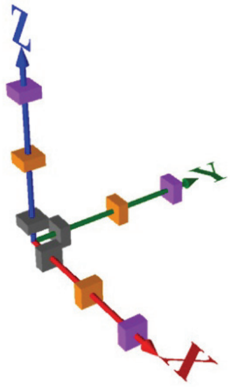

Figure 2.2: AHRS using inertial sensor triads

The theory of operation and the governing equations of MEMS vibrating gyroscopes, capacitive accelerometers and magneto inductive magnetometers are presented in the following paragraphs.

### 2.1.1 MEMS Gyroscopes

Early in the eighteenth century, mechanical gyroscopes started to be produced for measuring orientation; gyroscopes measure the rate of change in angular orientation, that is, angular velocity. After the MEMS revolution, micro-machined gyroscopes were developed based on a variety of physical phenomena.

The two types of MEMS gyroscope of interest are fibre optic gyroscope and the vibrating element gyroscope.

#### 2.1.1.1 Fibre-Optic Gyroscope

As the name implies, the fibre optic type uses the high sensitivity of fibre optic cables to change orientation and stress according to the Sagnac effect, discovered in 1913. The sensor is composed of a laser source that splits a beam and sends it in opposite directions in a fibre optic ring. The two laser beams recombine, supposing they would be in perfect phase. The phase difference between beams changes with angular velocity. Thus, by measuring the phase difference due to interference, a relation can be established to calculate angular velocity.

The governing equation for FOG gyroscope is written as:

$$\Delta S = \frac{8\pi n A\omega}{c\lambda} \tag{2.1}$$

where $\Delta S$ is the Sagnac phase shift, n is the number of turns of the fibre optic coil around the ring, $A$ is the cross-sectional area of the fibre, $\omega$ is the angular velocity of the body, $c$ is the speed of light, and $\lambda$ is the wave length of the laser beam emitted inside the fibre optic coil [21].

#### 2.1.1.2 Vibrating Element Gyroscope

The vibrating element gyroscope operation depends on measuring the Coriolis acceleration that is directly proportional to the angular velocity.

Coriolis Effect occurs for an object moving with linear velocity from a rotating frame of reference. As an example, assume the rigid body as shown in Figure 2.3 is moving along the y-axis with linear velocity v along the y-axis. When a rotation exists around the positive z-axis (considering Faraday's right hand rule), a resultant Coriolis acceleration $a_c$ (x-axis direction in this example) will occur perpendicular to both the rotation axis (z-axis direction) and the linear velocity (y-axis direction). The resultant Coriolis acceleration is calculated by equation (2.2)

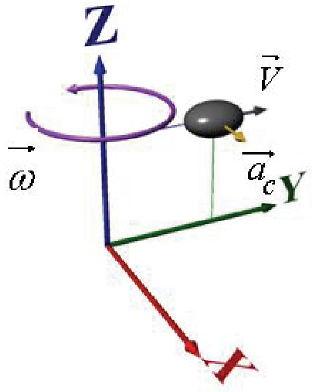

Figure 2.3: Coriolis acceleration vector illustration

$$a_c = 2v \times \omega \tag{2.2}$$

This can be written alternatively, by

$$a_c = -2\omega \times v \tag{2.3}$$

Thus, applying Newton's second Law:

$$F = m\,a \tag{2.4}$$

$$F_c = 2mv \times \omega \tag{2.5}$$

such that $F_c$ is the Coriolis force resulting from the angular rotation.

This yields:

$$a_c = 2.v.\omega \tag{2.6}$$

This phenomenon was applied before MEMS technology was developed, by applying lateral excitation on a tuning fork as shown in Figure 2.4.

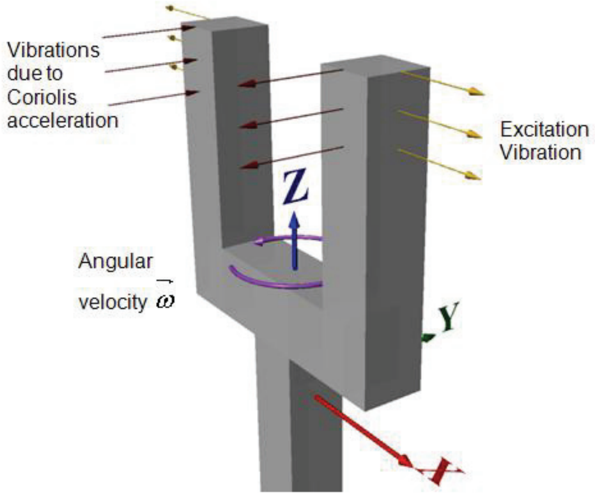
Vibrations due to Coriolis acceleration
Excitation Vibration
Z
Angular velocity $\vec{\omega}$
Y
X

Figure 2.4: Tuning fork analogy to measure angular rate using Coriolis force

If the tuning fork resonates at its first vibration-mode, the fork-tines (i.e. prongs) move in the same plane but in opposite directions. Coriolis forces will result perpendicular to the excitation forces because of the rotation around the main axis of the fork. Thus, by calculating the resultant Coriolis forces or acceleration, the angular velocity can be calculated.

Scientists and researchers who developed the miniature tuning fork gyroscopes using the MEMS technology used the same theory of operation as that in the earlier mechanical one. However, several key parameters had to be taken into consideration due to the extremely small size and strength of the MEMS structure.

This type of gyroscope uses two vibration mechanisms to measure acceleration. The first mechanism is excited by the system in order to generate Coriolis forces accompanying rotation. The second mechanism is a capacitive-based MEMS comb drive to transform the Coriolis vibrations from the physical mechanical quantity into its electrical form as a voltage or duty cycle sensor signal. After that, the sensor readings are filtered and amplified according to the sensor specifications, using traditional electronic circuits that are also embedded on the same semiconductor die. Geen and Krakauer from Analog Devices showed that their iMEMS™ gyroscopes are built upon the concept of measuring the Coriolis acceleration, as shown in Figure 2.5 [22].

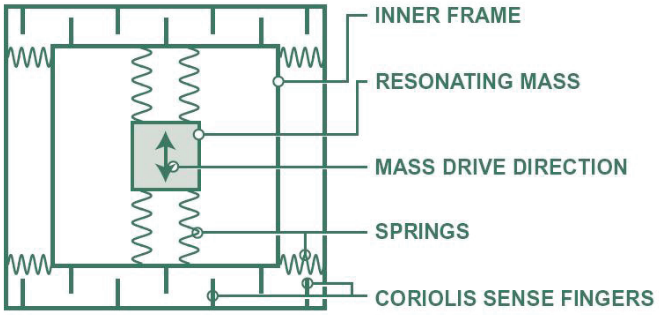

Figure 2.5: iMEMS gyroscope from Analog Devices™

The Analog Device's inertial measurement sensor ADIS 16355 was chosen for use in this research because of its relatively low cost and medium accuracy. This MEMS sensor includes tri-axial gyroscopes, accelerometers and temperature sensors. Moreover, it is factory-calibrated over its operating temperature range, making the calibration process more facile [23].

In the instrumentation industry, the specifications of transducers and sensors have to be strictly adhered to in order to minimize measurement errors. The most significant specifications for MEMS angular rate gyroscopes were studied, with emphasis on the Analog Devices ADIS16355 (See Appendix A):

The time domain signals for the three axial gyroscope angular rates and their discrete trapezoidal integration (i.e. angles) are shown in Figure 2.6 through Figure 2.8.

The sensors were held at stationary position (i.e. zero angular rates) that was acquired using the experimental set-up discussed in Chapter 5.

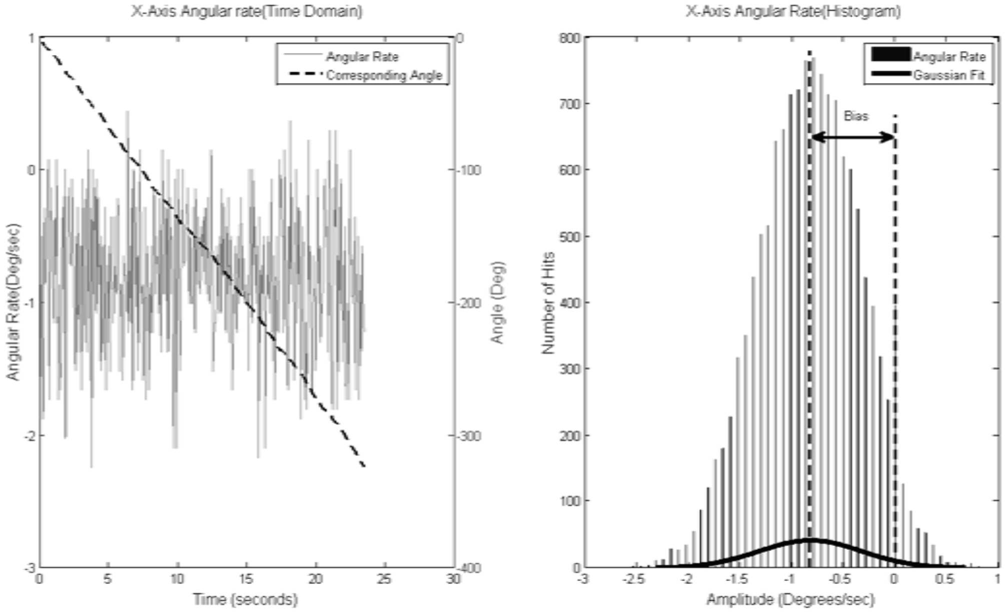

Figure 2.6: Raw angular rate vs. angular orientation data about x-axis

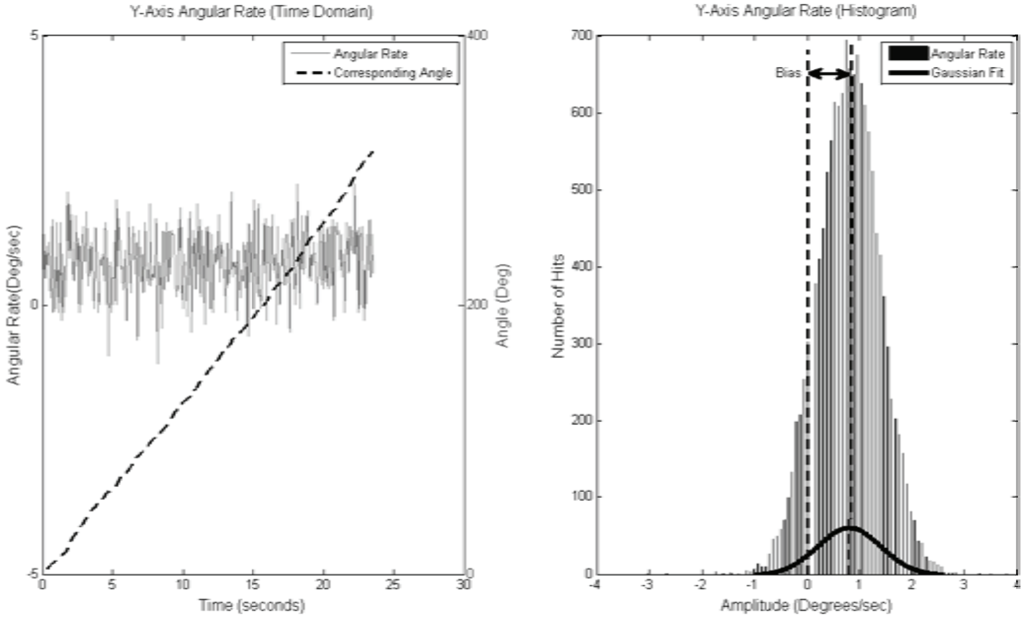

Figure 2.7: Raw angular rate vs. angular orientation data about y-axis

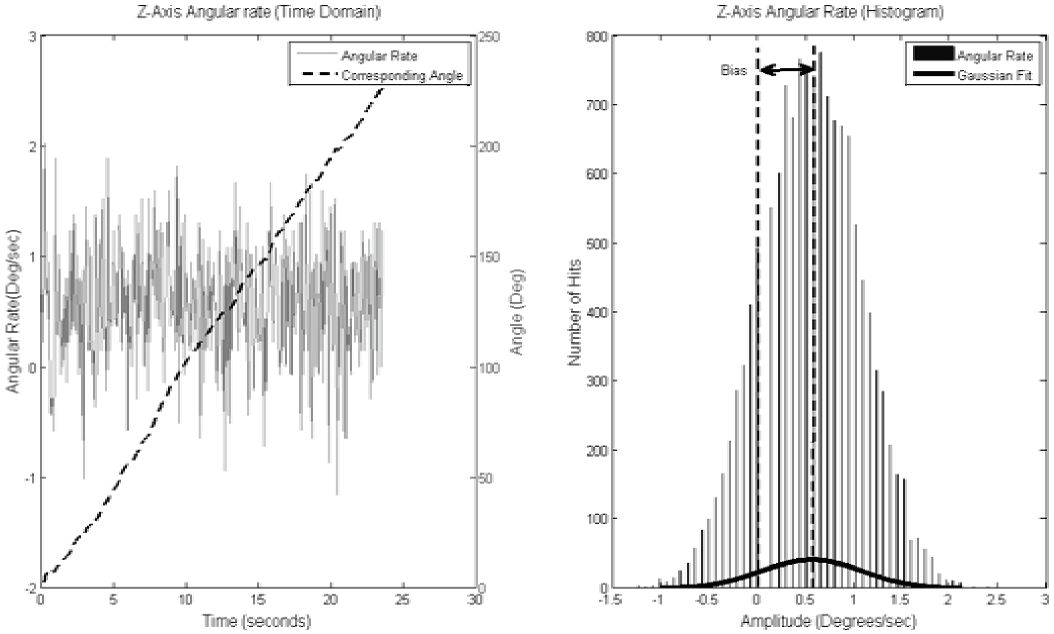

Figure 2.8: Raw angular rate vs. angular orientation data about z-axis

The statistics for the previous plots are shown in Table 2.1

Table 2.1: Angular rate data-statistics summary

| **Angular rate Axis** | **Mean** | **Standard Deviation** | **Variance** |
|---|---|---|---|
| | **(deg/s)** | | |
| $G_x$ | -0.8229 | 0.4960 | 0.2460 |
| $G_y$ | 0.7879 | 0.6001 | 0.3601 |
| $G_z$ | 0.5597 | 0.5181 | 0.2684 |

The discrete integration process results in Euler's orientations angles by the following equations:

$$Roll = \sum_{k=1}^{\infty} \omega_x \, T_s \tag{2.7}$$

$$Pitch = \sum_{k=1}^{\infty} \omega_y \, T_s \tag{2.8}$$

$$Yaw = \sum_{k=1}^{\infty} \omega_z \, T_s \tag{2.9}$$

Such that $T_s$ is the sampling time, $\left(\frac{1}{17}\right)$ sec for this research. Although the sensor is at equilibrium, the angle measurements' histograms show a Gaussian distribution around a non-zero mean, Table 2.1, showing the static bias (offset) of the gyroscope in the x, y, and z directions. Thus, the static bias must be calculated before we begin any data acquisition process.

The gyro static bias calibration was also taken into consideration during the practical implementation. In order to cancel out these biases, the embedded software averages the first few samples (100 to 150) at equilibrium, and the output average is considered the static bias. Next, theses calculated static biases are subtracted from the forthcoming sensor values. Furthermore, the dynamic biases of the gyroscopes are estimated using an Extended Kalman Filter to overcome the sudden unnecessary oscillations [24]. The output of the unbiased angular rates as well as the resulting angles showed relatively better results than raw data calculations, Figure 2.9.

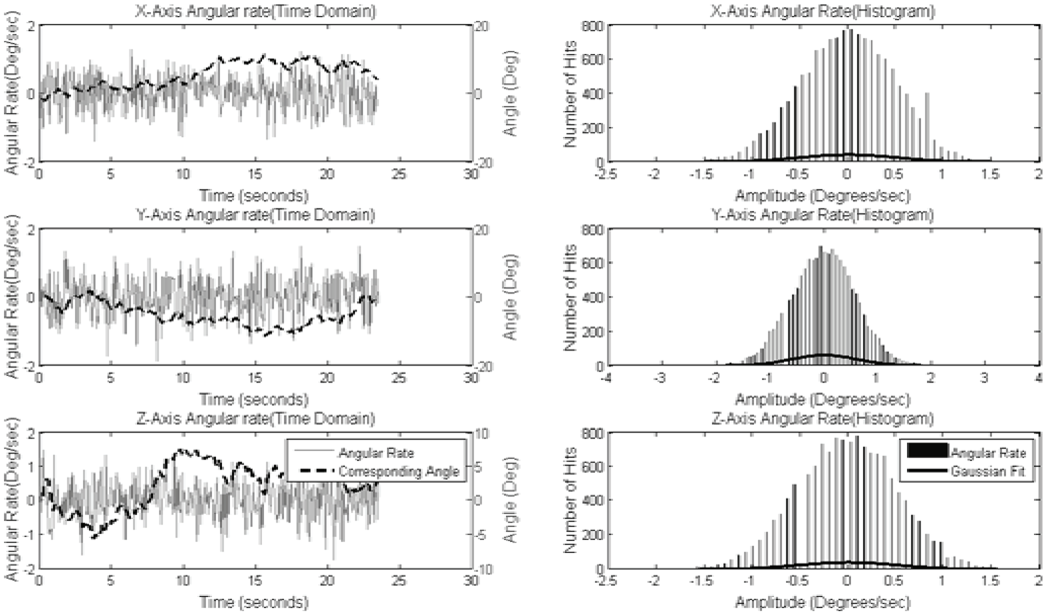

Figure 2.9: Angular rate data after static bias compensation

However, since dynamic drift, noise due to linear accelerations, manufacturing misalignment, and sensor-temperature response inject randomness in the system, sensor fusion between multiple inertial sensors – that is, Gyroscopes, accelerometers and magnetometers – had to be considered.

### 2.1.2 MEMS Capacitive Accelerometers

Mechanical accelerometers are used in many applications. Their mechanical structure has a proof mass with an attached needle and a spring, analogous to weighing instruments of the past. The mechanical model of an accelerometer, with its approximate mass spring and damper equivalent, is shown in Figure 2.10. The differences between forces acting on the mass are proportional to the linear acceleration.

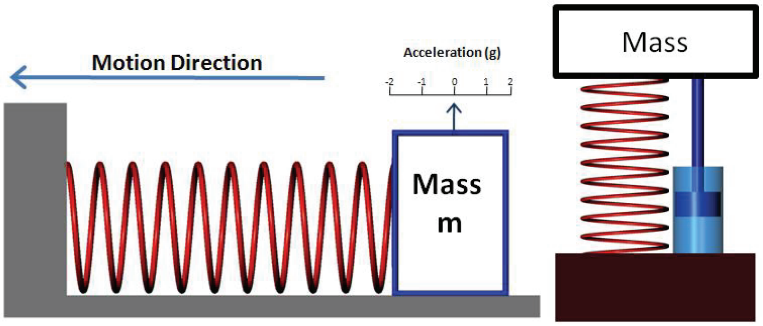

Figure 2.10: Accelerometer approximated mass-spring model

The spring exerts a force of

$$F_{spring} = -Kx \tag{2.10}$$

Where K is the spring constant, x is the travelled distance, and F is the spring reaction force. The damping force is

$$F_{spring} = -cv = -c\dot{x} \tag{2.11}$$

This equation obeys Newton's second Law :

$$\sum F = ma = m\frac{d^2x}{dt^2} \tag{2.12}$$

The above equations are combined to form the second-order differential equation for displacement x as:

$$m\ddot{x} + c\dot{x} + kx = 0 \tag{2.13}$$

This yields:

$$\ddot{x} + 2\xi\omega_0\dot{x} + \omega_0^2 x = 0 \tag{2.14}$$

Where the undammed natural frequency is

$$\omega_0 = \sqrt{\frac{k}{m}}(rad/sec) \tag{2.15}$$

and the damping ratio is:

$$\xi = \frac{c}{2\sqrt{km}} \tag{2.16}$$

MEMS accelerometer designs more or less follow this same design concept. A proof mass is suspended over a small gap on the end a cantilever or hanging from a membrane flexible structure. Figure 2.11 shows the difference in the MEMS structure between a Piezo-resistive accelerometer and a capacitive accelerometer.

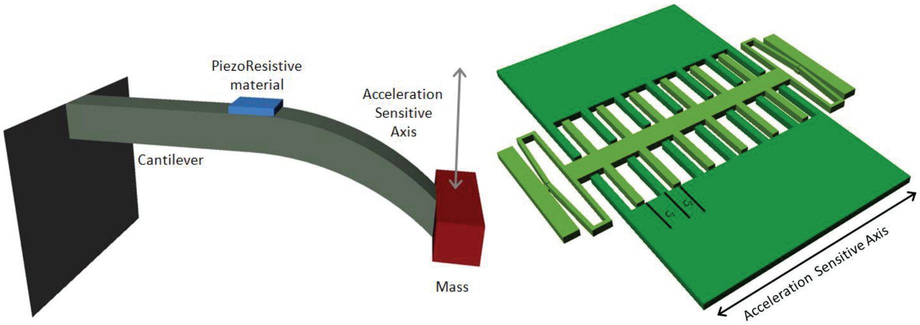

Figure 2.11: Piezo-resistive vs. capacitive accelerometers structure

In the Piezo-based system, the deflection is less than the capacitive, which provides more sensitivity – up to $1\ \mu g$, where $g$ is the gravitational acceleration. However, this reduces the overall measurement dynamic range of the sensor and obliges the designer to consider a relatively large proof mass. Furthermore, capacitive accelerometers are less vulnerable to temperature changes than the Piezo-resistive systems.

In addition, the electronic circuitry needed to convert mechanical acceleration to an electrical signal is simple in Piezo-resistive accelerometers, because Piezo electric materials generate voltages proportional to the applied stress. On the other hand, capacitive MEMS accelerometers need a more complex circuitry involving alternating voltages and modulation/demodulation electronics, as shown in Figure 2.12 [25].

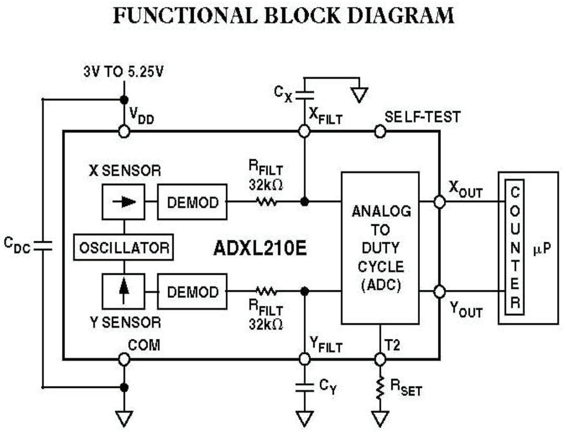

Figure 2.12: MEMS accelerometer internal circuit (Analog Devices™)

Tilt angle measurement using accelerometer values depends entirely on the gravitational acceleration. However, this is not the case for dynamic bodies or systems, where linear accelerations are added to the measured data.

The inertial frame for the body segment or the sensor is given with respect to Earth's-Centered-Earth-Fixed (ECEF) frame, as shown in Figure 2.13. The frame assignment used in this research follows the conventional one used in aviation [26]. Assuming that the arm is held horzointal to earth, the positive x-axis points towards the elbow of the human arm from the shoulder's joint prespective, the positive z-axis points downwards towards earth, and the positive y-axis is to the right of the right arm, also known as Local Tangent Plane (LTP).

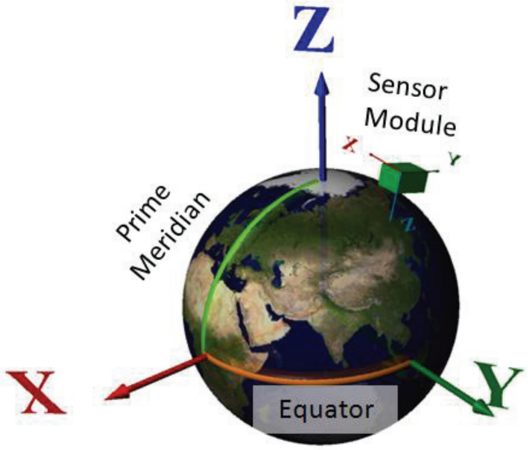

Figure 2.13: ECEF Vs sensor coordinate frame

The time domain three-axes accelerations and their corresponding static biases acquired by the analog devices ADIS16355 [23] are shown in Figure 2.14 through Figure 2.16. These experimental results were also taken at the equilbirum state of the sensor held horizontally, measuring normalized accelerations due to gravity; that is, $a_x=a_y=0$, and $a_z=1$ using the developed sensor module discussed in Chapter 5.

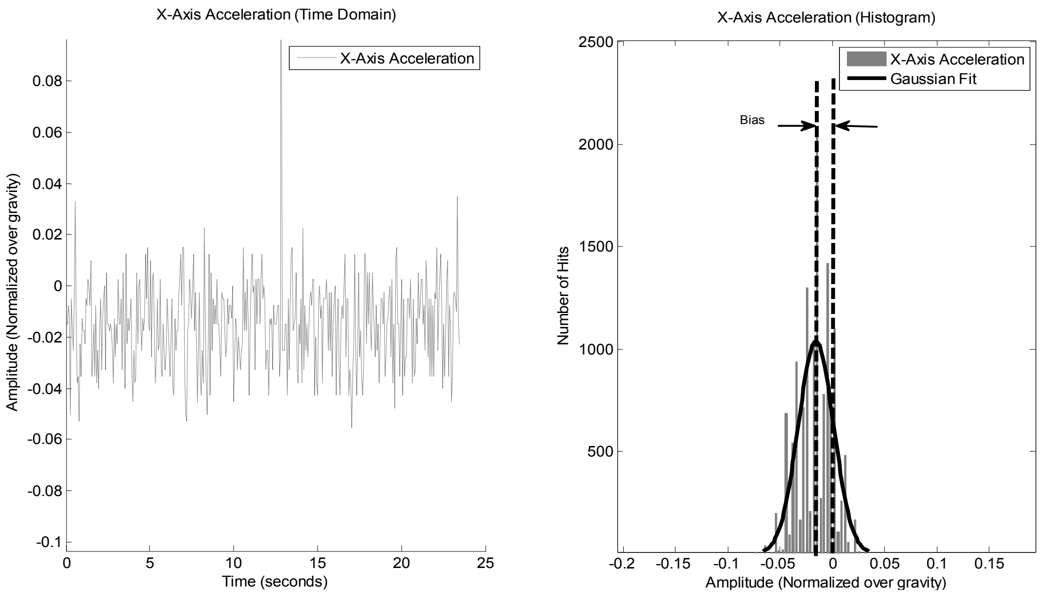

Figure 2.14: Raw linear acceleration along x-axis with sensor module fixed

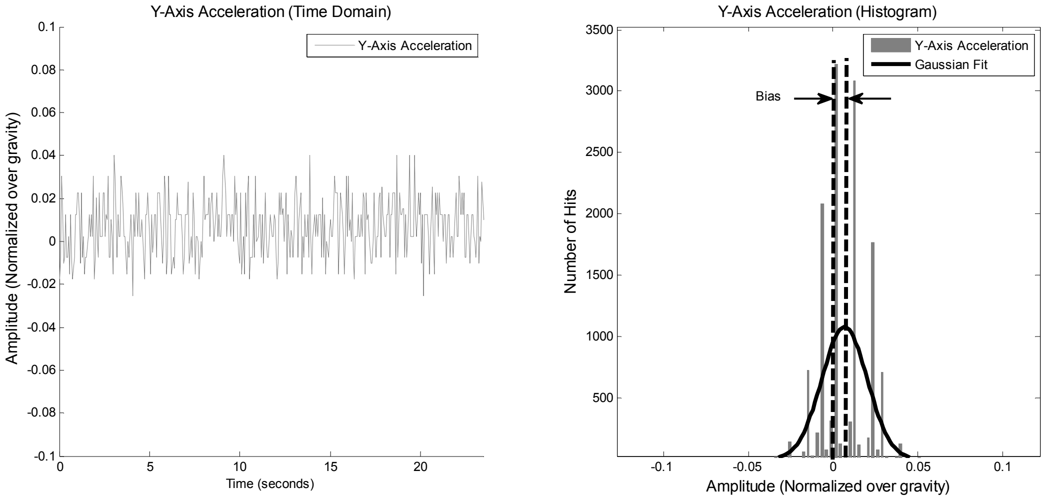

Figure 2.15: Raw linear acceleration along y-axis with sensor module fixed

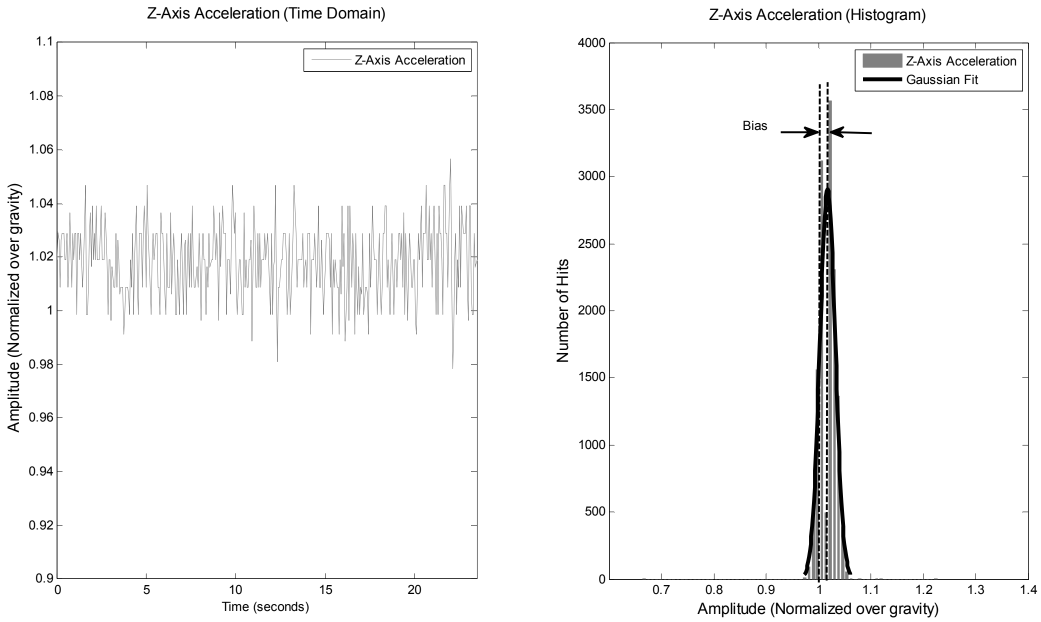

Figure 2.16: Raw linear acceleration along z-axis with sensor module fixed

Table 2.2: Acceleration data statistics summary

| **Accelerometer axis** | **Mean** | **Standard Deviation** | **Variance** |
|---|---|---|---|
| | **(Normalized/g)** | | |
| Ax | -0.0158 | 0.0169 | 2.8661e-004 |
| Ay | 0.0068 | 0.0134 | 1.8078e-004 |
| Az | 1.0176 | 1.0176 | 2.1574e-004 |

The correspnding statistics for the data acquired in Figure 2.14 through Figure 2.16 are shown in Table 2.2. The Pitch (θ) tilt angle of a rigid body using a single axis accelerometer can be calculated as shown in Figure 2.17.

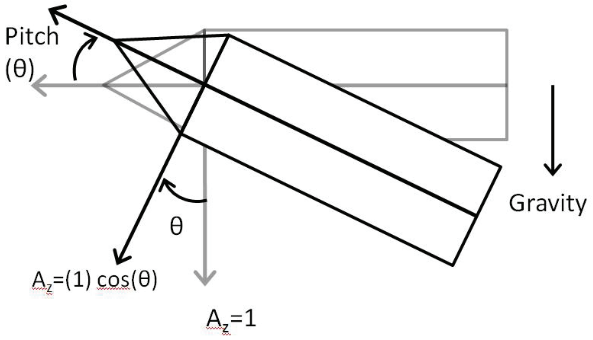

Figure 2.17: Pitch angle measurement theory using single axis accelerometer

The following simple vector relation can be used to obtain the the pitch angle as:

$$\theta = cos^{-1}\left(\frac{Accelerometer_{value}}{Acceleration_{gravity}}\right) \tag{2.17}$$

The same method can be used to calculate Roll angle (φ) by using a second orhtognally mounted accelerometer. However, a combination of all three accelerometers can be used to pinoint accurately the three Euler angles of the sensor's coordinate frame. These required angles are obtained by applying the following relations [27]:

For the Roll angle:

$$\begin{bmatrix} sin(\phi) \\ cos(\phi) \end{bmatrix} = \begin{bmatrix} -\overline{a_y} \\ -\overline{a_z} \end{bmatrix} \tag{2.18}$$

such that the normalized vector $\overline{a_y} = \frac{a_y}{\sqrt{a_y^2+a_z^2}}$ is the normalized y-axis accelerometer data over earth's gravity (i.e. 9.8 m/sec$^2$).

Also

$$\overline{a_z} = \frac{a_z}{\sqrt{a_y^2 + a_z^2}}$$

Dividing both equations in the L.H.S. vector in equation (2.18) yields

$$tan(\phi) = \left(\frac{\overline{a_y}}{\overline{a_z}}\right) \tag{2.19}$$

and therefore

$$\phi = tan^{-1}\left(\frac{\overline{a_y}}{\overline{a_z}}\right) \tag{2.20}$$

Nevertheless, a problem is introduced by using the atan function: The quadrant determination of the angle cannot be determined accurately unless the corresponding two-argument arc tan one (i.e. atan2 ) is used. This method limits the angle range between +180 and -180 degrees. Knowing that the two-argument arc tan function can be defined using:

For y≠0

$$atan2(y,x) = \begin{cases} \rho \cdot sgn(y)\,; & x > 0 \\ \frac{\pi}{2} \cdot sgn(y); & x = 0 \\ (\pi - \rho) \cdot sgn(y)\,; & x < 0 \end{cases}$$

And For y=0

$$atan2(y,x) = \begin{cases} 0\,; & x > 0 \\ undefined; & x = 0 \\ \pi\,; & x < 0 \end{cases}$$

Such that $\rho$ is the angle and $\tan(\rho) = \left|\frac{y}{x}\right|$. Also sgn is the mathematical sign function.

Also the atan2 function can be expressed interms of arc tan half angle function as:

$$atan2(y,x) = 2\,tan^{-1}\left(\frac{y}{\sqrt{x^2 + y^2} + x}\right)$$

$$\phi = atan2\left(\frac{\overline{a_y}}{\overline{a_z}}\right) \tag{2.21}$$

Similarily The pitch angle can be obtained using the two equations:

$$\begin{bmatrix} sin(\theta) \\ cos(\theta) \end{bmatrix} = \begin{bmatrix} \overline{a_x} \\ -\overline{a_y}\ sin(\phi) + \overline{a_z} cos\ (\phi) \end{bmatrix} \tag{2.22}$$

Following the same methodology to obtain equation (2.21), the pitch angle is obtained by:

$$\theta = atan2\left(\overline{a_x}\ , -\overline{a_y}\ sin(\phi) + \overline{a_z}\ cos(\phi)\ \right) \tag{2.23}$$

However, obtaining roll and pitch angles from accelerometers has to be done after static bias correction and low pass filtering those sensor values. The pitch and roll angles obtained from the unbiased acceleromter data in the equilbrium state (i.e. ideally ax=0, ay=0, az=1) are shown as follows in Figure 2.18 and Figure 2.19 noting that about 1 degree error was expected due to human placement errors :

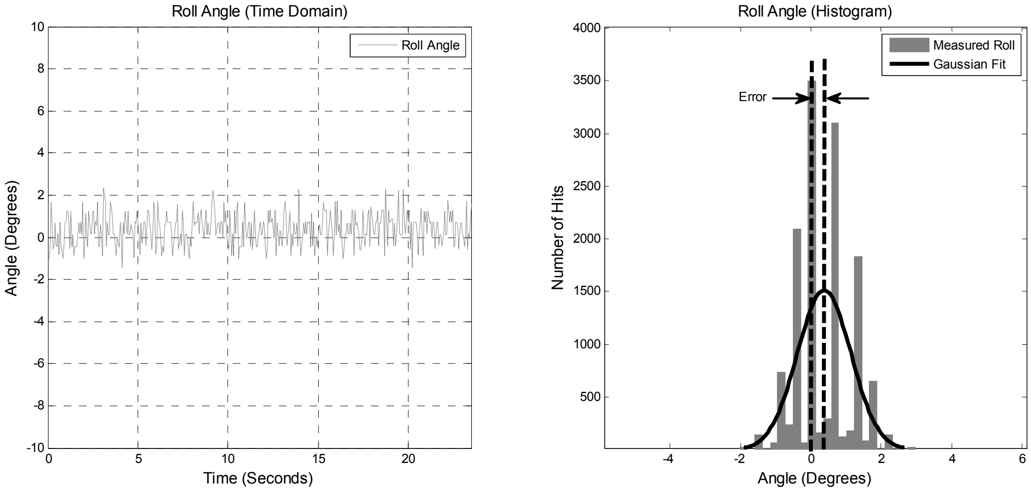

Figure 2.18: Roll angle using unbiased accelerometer values

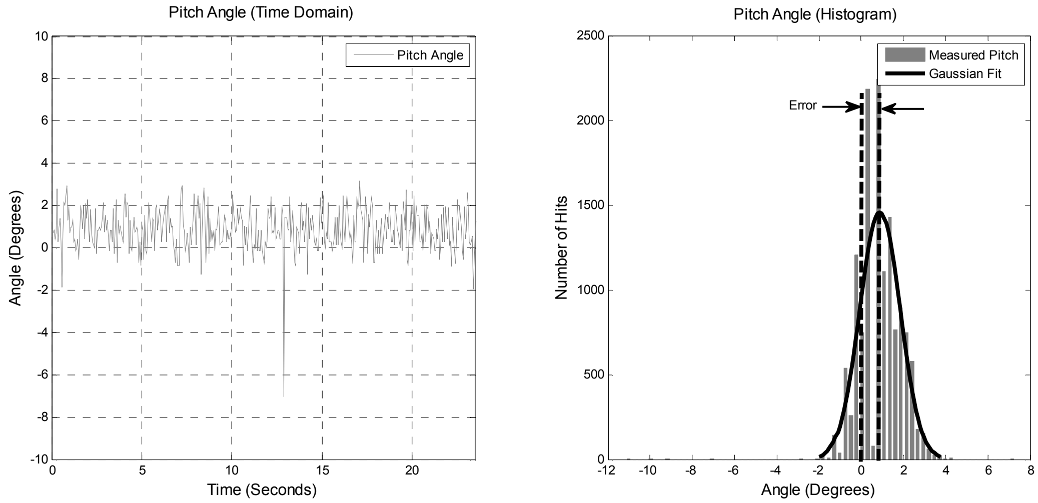

Figure 2.19: Pitch angle using unbiased accelerometer values

The statistical analysis summary for Figure 2.18 and Figure 2.19 is shown in Table 2.3.

Table 2.3: Roll and pitch angles' statistics calculated using accelerometers

| **Angle** | **Mean (deg)** | **Standard Deviation** | **Variance** |
|---|---|---|---|
| Roll (Φ) | 0.3814 | 0.7575 | 0.5737 |
| Pitch (θ) | 0.8923 | 0.9537 | 0.9096 |

The large variance value for the pitch angle is due to the external vibrational noises in the laboratory during the experiment.

Nevertheless, the Yaw angle – heading angle around the z-axis – cannot be calculated using accelerometers, because of the semmetry of eath’s magnetic field while rotating around that axis. This fact introduces the use of magnetometers as a heading measuring sensors to calculate the yaw angle with respect to earth's magnetic north.

### 2.1.3 MEMS Magnetometers

Earth's magnetic field is considered relatively small, ~0.5 to 0.6 Gauss. Chinese historical literature shows that the magnetic compass was used for navigation as early as the fourth century BC. Later, the principles upon which a magnetometer depends were classified into either mechanical, magneto-resistive, Hall Effect, and magneto-inductive. The magneto-inductive magnetometer type was chosen for use in this project because of its low cost and small size. The general theory of operation to measure magnetic field using inductance dates to 1831, when British scientist Michael Faraday discovered electromagnetic induction.

Faraday developed his law through observing a voltage change in a coil wrapped around a soft-iron core loop when voltage was applied to another nearby coil. Later, these proofs of concept led to the invention of the transformer. Magneto-inductive sensors can be simplified based on Faraday's experiment. However, several noise sources can dramatically affect a magnetometer reading; these include temperature change, and surrounding electromagnetic interference due to sources or iron cores. The PNI-11096 (Appendix B) magneto-inductive sensor driver ASIC chip applies an oscillator o/p into an end of a coil parallel to the magnetic sensitive axis while grounding the other end of the coil. Furthermore, a counter counts the time taken for a predetermined oscillations number. Next, the same measurement is done after switching the coil terminals, as shown in Figure 2.20 [28].

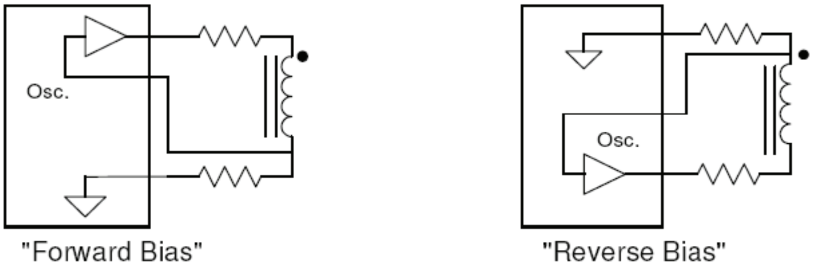

Figure 2.20: Forward /Reverse bias (courtesy of PNI™ Corp.)

This differential method of calculation reduces vulnerability to temperature change.

The following trigonometric relation can be used to calculate yaw angle $\psi$ (Heading) using a minimum dual-axis magnetometer held parallel to earth's horizon:

$$tan(\psi) = \left(\frac{B_y}{B_x}\right) \tag{2.24}$$

$$\therefore \psi = atan\left(\frac{B_y}{B_x}\right) \tag{2.25}$$

One way for the processor to keep track of the angle is to apply the following constraints:

| | |
|---|---|
| Heading angle $\psi$= 90-[arc tan(x/y)*180/$\pi$] | $B_y>0$ |
| Heading angle $\psi$= 270-[arc tan(x/y)*180/$\pi$] | $B_y<0$ |
| Heading angle $\psi$= 180 | $B_y=0$ & $B_x<0$ |
| Heading angle $\psi$= 0 | $B_y=0$ & $B_x>0$ |

These relationships are applied due to the fact the vector field strengths surrounding earth are almost planar near the equator, but as they approach the poles the z-component appears. It should be known that earth's geographic north is not the same as its magnetic north. Furthermore, compass readings point towards the magnetic north. The angular offsets between compass north, magnetic north and geographic north are shown in Figure 2.21 [27].

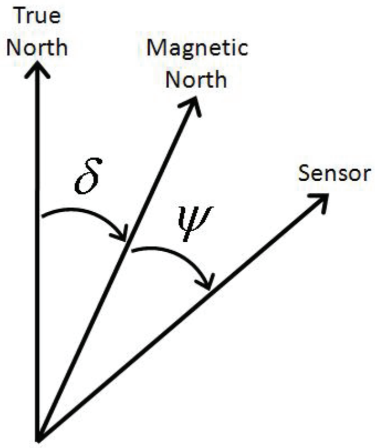

Figure 2.21: Geographic, Magnetic north versus sensor heading angle

Where declination angle is denoted by δ and the heading angle by ψ.

It is also worth noting that the magnetic declination angle δ changes with both the position on earth's surface (longitude and latitude) and time. For simplicity in this research, magnetic north is considered the reference to the yaw angle. To refer to true north, one can use the World Magnetic Model (WMM) whenever the sensory system is moved to a new location to find the declination angle.

Figure 2.22 through Figure 2.24 show the normalized magnetic field flux density readings for the x-, y- and z-axis, and their histograms sampled using the PNI-MicroMag3 tri-axes magnetometer at stationary position pointing towards about 95 degrees from Magnetic North (± 1-degree error due to human placement and axes misalignments).

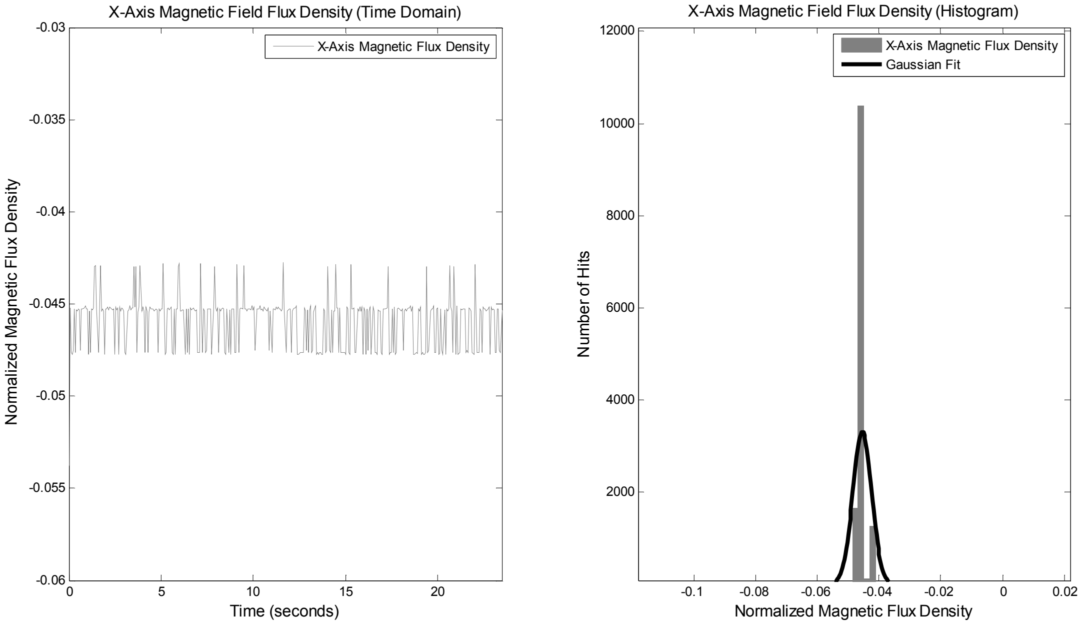

Figure 2.22: Normalized magnetic flux density in the x-axis

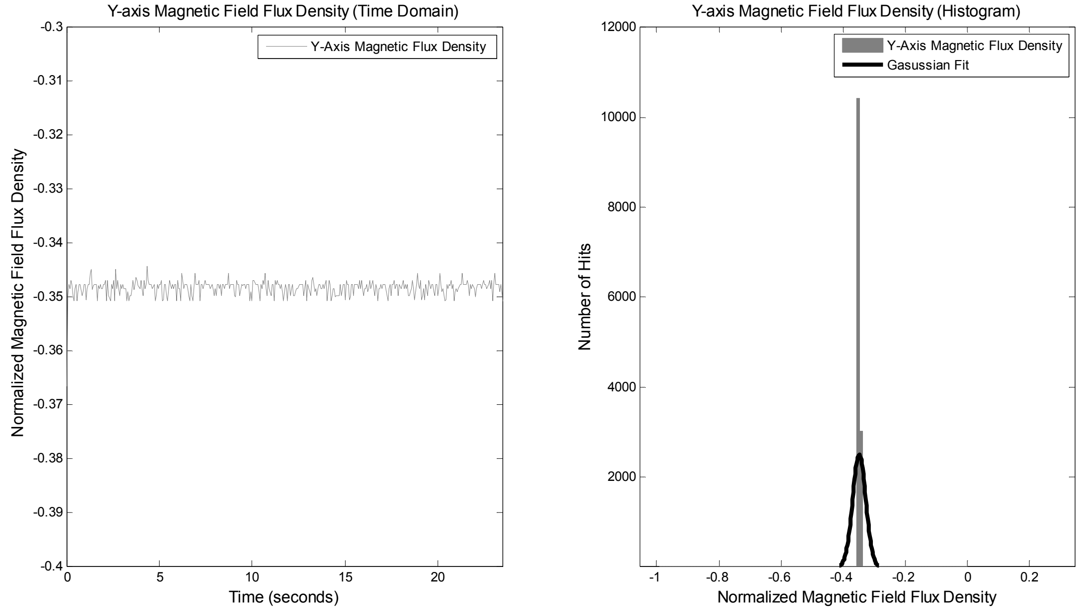

Figure 2.23: Normalized magnetic flux density in the y-axis

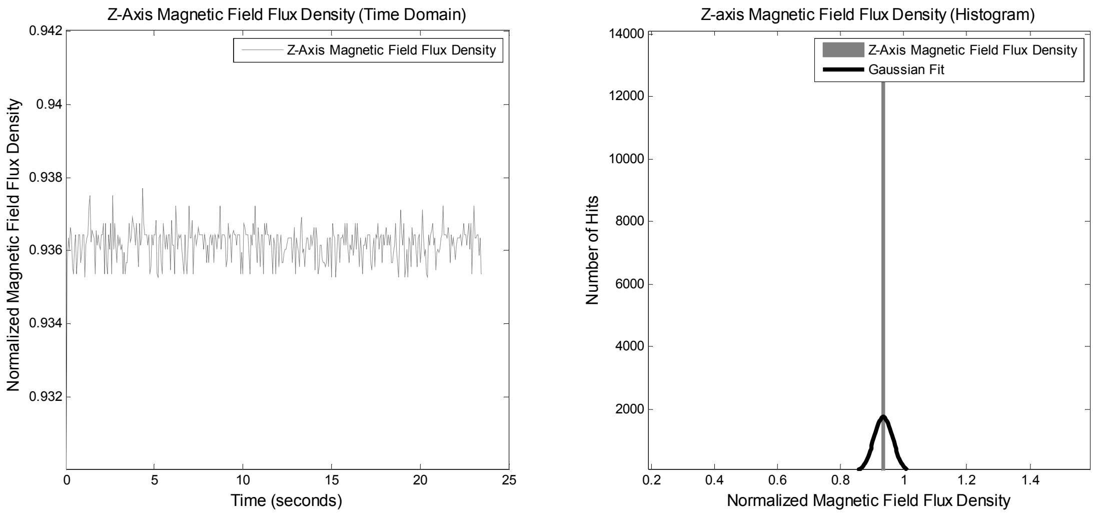

Figure 2.24: Normalized magnetic flux density in the z-axis

The corresponding statistical parameters are stated in Table 2.4.

Table 2.4: Magnetometer data statistics summary

| **Magnetometer axis** | **Mean (Normalized/Magnitude)** | **Standard Deviation** | **Variance** |
|---|---|---|---|
| $M_x$ | -0.0454 | 0.0031 | 9.3357e-006 |
| $M_y$ | -0.3485 | 0.0212 | 1.7240e-004 |
| $M_z$ | 0.9355 | 0.0302 | 9.1179e-004 |

In order to perform a magnetometer calibration against surrounding magnetic disturbances, usually the sensor is rotated two complete turns around its vertical axis**.** Figure 2.25 shows the corresponding oscillation counts resembling the magnetic field flux density given by the magnetometers by performing multiple 360-degree turns. It shows the effect of soft iron and hard iron magnetic disturbances surrounding the sensor, generating inconsistencies.

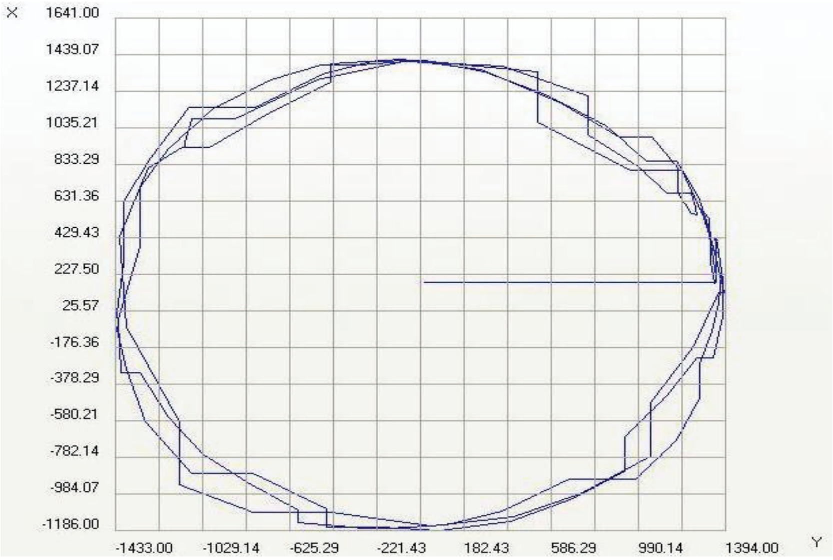

Figure 2.25: Magnetic flux density frequency counts performing 360 loops

Since the previous results assume a perfect horizontal orientation of the magnetometer, heading errors are induced. Gebre Eghziabher [29] showed a method to combine accelerometers and magnetometers integrated with baseline attitude and GPS to calculate orientation parameters without the use of gyroscopes. Furthermore, the method introduced by Bekir [27] was used to obtain the magnetic heading angle (yaw) by combining magnetometers and accelerometer sensors. The algorithm to obtain the yaw angle depends on obtaining the angle towards magnetic north after compensating the tilt effects on the magnetometers. The following equations can solve the tilt compensation problem of the magnetometer readings using the accompanying accelerometers:

Assuming the vector P is the output vector from the cross product between the acceleration vector and the magnetic field vector,

$$\begin{bmatrix} P_x \\ P_y \\ P_z \end{bmatrix} = \begin{bmatrix} m_x \\ m_y \\ m_z \end{bmatrix} \times \begin{bmatrix} \overline{a_x} \\ \overline{a_y} \\ \overline{a_z} \end{bmatrix} = \begin{bmatrix} \overline{a_z} m_y - \overline{a_y} m_z \\ \overline{a_x} m_z - \overline{a_z} m_x \\ \overline{a_y} m_x - \overline{a_x} m_y \end{bmatrix} \tag{2.26}$$

and yields

$$tan(\psi) = \left( \frac{P_x}{\overline{a_y} P_z - \overline{a_z} P_y} \right) \tag{2.27}$$

Following the same concept as the Pitch and Roll angles to convert the tan function to specify quadrants, the Yaw and angle are given by:

$$\psi = atan2(P_x \, , \overline{a_y} P_z - \overline{a_z} P_y) \tag{2.28}$$

The output of equation (2.28) using the sampled data with the sensor almost pointing towards 95 degrees from magnetic north is shown in Figure 2.26 (the design of the sensor can be seen in Chapter 5).

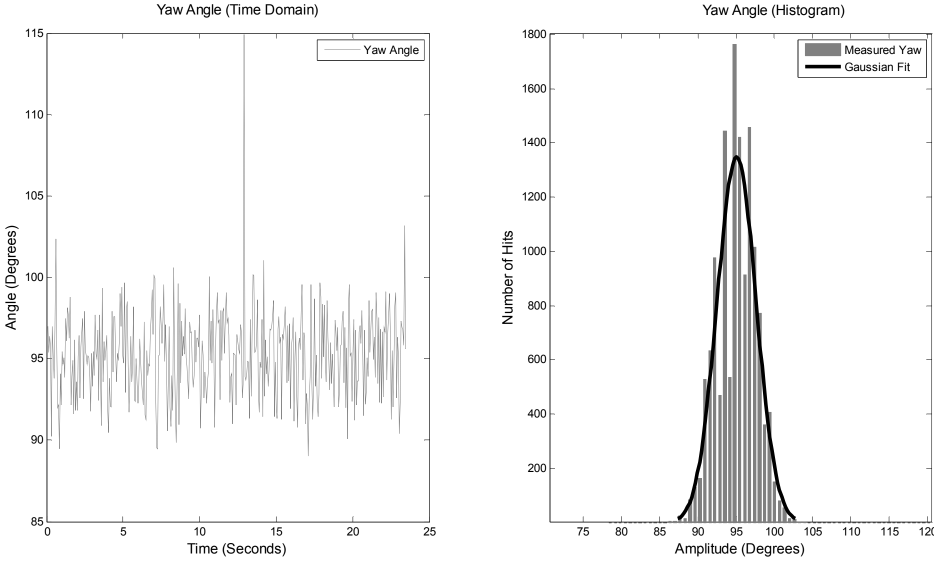

Figure 2.26: Heading angle output using tilt compensated magnetometers

The statistics for Figure 2.26 are stated in Table 2.5:

Table 2.5: Yaw angle statistics summary

| **Orientation angle** | **Mean** | **Standard deviation** | **Variance** |
|---|---|---|---|
| Ψ | 95.0572 | 2.5607 | 6.5572 |

As a result, from data in this Chapter, all three-orientation angles could be obtained using at least two of the inertial sensors as shown in Table 2.6.

Table 2.6: Sensor methods for obtaining Euler angles

| **Angle** | **Source I** | **Source II** |
|---|---|---|
| Roll (θ) | Discrete integration of the gyroscope angular velocity about x-axis (Gx). | Calculating tilt using accelerometers. |
| Pitch (φ) | Discrete integration of the gyroscope angular velocity about the y-axis (Gy). | Calculating tilt using accelerometers. |
| Yaw (ψ) | Discrete integration of the gyroscope angular velocity about the z-axis (Gz) **.** | Using tilt-compensated magnetometers. |

## 2.2 Orientation Determination

The Euler angles (θ, φ and ψ) are sufficient to express orientation and rotation in three-dimensional space using several representation methods – Directional Cosine Matrix, Euler's axis-angle, Euler rotations and Quaternions.

The most common methods, directional cosine matrix and quaternion, were studied as follows.

### 2.2.1 Orientation Determination using Directional Cosine Matrix

As the name implies, each element of the directional cosine matrix is the cosine of the angle between an axis of the three axes of the body's frame at a given point in time and the reference unit axis. The coordinate frame used here is a local frame with respect to the sensor body. The x, y and z unit vectors point towards front, right and down of each sensor (Local NED frame).

The two-dimensional clockwise rotation of the sensor in space around its z-axis with an angle ψ (heading angle) the rotation matrix is given by:

$$R(\psi) = \begin{bmatrix} cos(\psi) & sin(\psi) \\ -sin(\psi) & cos(\psi) \end{bmatrix} \tag{2.29}$$

Matrix R has the properties: $R.R^T = I \quad and \quad det(R) = 1$

Extending the rotation to a three-dimensional spatial one, the rotation matrices about each of the three basis axes are shown next.

The pure rotation around x-axis (Roll) is given by:

$$R_x(\phi) = \begin{bmatrix} 1 & 0 & 0 \\ 0 & cos(\phi) & sin(\phi) \\ 0 & -sin(\phi) & cos(\phi) \end{bmatrix} \tag{2.30}$$

and the rotation around the y-axis (Pitch) is given by:

$$R_y(\theta) = \begin{bmatrix} cos(\theta) & 0 & -sin(\theta) \\ 0 & 1 & 0 \\ sin(\theta) & 0 & cos(\theta) \end{bmatrix} \tag{2.31}$$

Finally, the rotation around the z-axis (Yaw or change in heading angle) is given by:

$$R_z(\psi) = \begin{bmatrix} cos(\psi) & sin(\psi) & 0 \\ -sin(\psi) & cos(\psi) & 0 \\ 0 & 0 & 1 \end{bmatrix} \tag{2.32}$$

Representation of rotation in three-dimensional Euclidean space can be obtained using multiplication of the matrices shown in equations (2.30) thorough (2.32). For instance, the rotation of the inertial sensor around the z-, y- and x-axis can be calculated as:

$$\begin{aligned} R_{zyx}(\psi, \theta, \varphi) &= R_z(\psi). R_y(\theta). R_x(\phi) \\ &= \begin{bmatrix} c\psi s\theta & s\psi c\theta & s\theta \\ c\psi s\theta s\phi - s\psi c\phi & s\psi s\theta s\phi + c\psi c\phi & c\theta s\phi \\ c\psi s\theta c\phi + s\psi s\phi & s\psi s\theta c\phi - c\psi s\phi & c\theta c\phi \end{bmatrix} \end{aligned} \tag{2.33}$$

such that the abbreviations $c\psi = cos\ (\psi)$, $s\psi = sin(\psi)$, and so on for the remaining angles.

But to obtain Euler angles from the Directional Cosine Matrix (DCM), we have:

$$\begin{bmatrix} \phi \\ \theta \\ \psi \end{bmatrix} = \begin{bmatrix} atan2(R_{23}, R_{33}) \\ -sin^{-1}(R_{13}) \\ atan2(R_{12}, R_{11}) \end{bmatrix} \tag{2.34}$$

This means that by using the three Euler angles φ, θ and ψ, different combinations of matrix multiplications other than the previous equation can be used to express rotation. Different rotation sequences can be (x, y, z), (x, z, y), (y, x, z), (y, z, x), (z, x, y) and (z, y, x), which make about six combinations; the angles are dependent, which means that any two 90-degrees rotation about two axes can be expressed as one 90-degree rotation around the third axis. Furthermore, one can express three-dimensional rotations by using only two of three rotation matrices by rotating the body about the first axis, then the second, then the first again, as in (z, x, z), (z, y, z), (y, x, y), (y, z, y), (x, y, x) and (x, z, x).

This exercise raises the number of combinations to 12. Moreover, one can choose between the reference frame to be either the previous local coordinate frame (relative coordinates) or earth's fixed frame (absolute coordinates), increasing the possible combinations to 24.

Several drawbacks appear when representing orientation using directional cosine matrices (Rotation Matrix), such as computation complexity and Gimbal-lock [30]. A well-known solution to these problems is to use quaternions.

### 2.2.2 Orientation Determination using Quaternions

Quaternions were invented by Sir. William Rowan Hamilton in 1843 as an attempt to generalize complex numbers to include three-dimensional space. A quaternion is represented as one scalar and three vector parts [30]:

$$Q = q_0 + q_1\hat{\imath} + q_2\hat{\jmath} + q_3\hat{k} \tag{2.35}$$

where $q_0$ is the scalar part and $q_1$, $q_2$ and $q_3$ are the three elements of the vector part. The vector part of the quaternion obeys the rule:

$$i^2 = j^2 = k^2 = ijk = -1 \tag{2.36}$$

The same quaternion can also be presented as:

$$Q = (q_s\,, \overrightarrow{q_v}\,) \text{ or } Q = (\theta, \hat{n})$$

such that $q_s$ is the scalar component, and $\overrightarrow{q_v}$ is the three-dimensional vector component.

Also, θ is the angle and n is the unit vector pointing along the direction of the rotation axis following the angle-axis Euler convention.

Quaternions can be represented in their matrix form [30] as:

$$Q = \begin{bmatrix} q_4 & -q_1 & -q_2 & -q_3 \\ q_1 & q_4 & -q_3 & q_2 \\ q_2 & q_3 & q_4 & -q_1 \\ q_3 & -q_2 & q_1 & q_4 \end{bmatrix} \tag{2.37}$$

To express a pure rotational transformation between two coordinate frames using quaternions, a quaternion multiplication takes place as:

$$PQ = (p_1\,, p_2, p_3\,, p_4\,) * (q_1\,, q_2, q_3\,, q_4\,)$$
$$= \begin{bmatrix} p_4q_4 - p_1q_1 - \ p_2q_2 - p_3q_3 \\ p_1q_4 + p_4q_1 + p_2q_3 - p_3q_1 \\ p_2q_4 + p_4q_1 + p_2q_3 - p_3q_2 \\ p_3q_4 + p_4q_3 + p_1q_2 - p_2q_1 \end{bmatrix} \quad (2.38)$$

Quaternion algebra is similar to vector algebra except for multiplication. The transformation between the Directional Cosines Matrix, Euler's axis-angle and quaternion form can be done quite easily. In order to calculate quaternion orientation using Euler angles, the following equation is used:

$$\begin{bmatrix} q_0 \\ q_1 \\ q_2 \\ q_3 \end{bmatrix} = \begin{bmatrix} c(\frac{\phi}{2})c(\frac{\theta}{2})c(\frac{\psi}{2}) + s\left(\frac{\phi}{2}\right)s\left(\frac{\theta}{2}\right)s(\frac{\psi}{2}) \\ s\left(\frac{\phi}{2}\right)c\left(\frac{\theta}{2}\right)c(\frac{\psi}{2}) - c(\frac{\phi}{2})s(\frac{\theta}{2})s(\frac{\psi}{2}) \\ c(\frac{\phi}{2})s(\frac{\theta}{2})c(\frac{\psi}{2}) + s(\frac{\phi}{2})c(\frac{\theta}{2})s(\frac{\psi}{2}) \\ c(\frac{\phi}{2})c(\frac{\theta}{2})s(\frac{\psi}{2}) - s(\frac{\phi}{2})s(\frac{\theta}{2})c(\frac{\psi}{2}) \end{bmatrix} \quad (2.39)$$

Given that $q_1$, $q_2$, and $q_3$ are the vector components that the coordinate frame rotated about. Also, $q_0$ is the scalar part of the quaternion expressing the angle that body rotated about. The quaternion to DCM rotation matrix is transformed using:

$$R = \begin{bmatrix} q_0^2 + \ q_1^2 - q_2^2 - q_3^2 & 2(q_1q_2 + q_3q_0) & 2(q_1q_3 + q_2q_0) \\ 2(q_1q_2 - q_3q_0) & q_0^2 + \ q_1^2 - q_2^2 - q_3^2 & 2(q_2q_3 + q_1q_0) \\ 2(q_1q_3 + q_2q_0) & 2(q_2q_3 + q_1q_0) & q_0^2 - \ q_1^2 - q_2^2 + q_3^2 \end{bmatrix} \quad (2.40)$$

knowing that the quaternion used in the transformation is a normalized quaternion by:

$$\begin{bmatrix} \bar{q}_0 \\ \bar{q}_1 \\ q_2 \\ q_3 \end{bmatrix} = \begin{bmatrix} \left(\frac{q_0}{m}\right) \\ \left(\frac{q_1}{m}\right) \\ \left(\frac{q_2}{m}\right) \\ \left(\frac{q_3}{m}\right) \end{bmatrix} \qquad (2.41)$$

such than: $m = \sqrt{q_0^2 + q_1^2 + q_2^2 + q_3^2}$

By analogy to equation (2.34), the transformation of quaternion notation back to Euler angles, the equation used is:

$$\begin{bmatrix} \phi \\ \theta \\ \psi \end{bmatrix} = \begin{bmatrix} atan2(2(q_2q_3 + q_0q_1), q_0^2 - q_1^2 - q_2^2 + q_3^2) \\ sin^{-1}(-2(q_1q_3 - q_2q_0)) \\ atan2(2(q_1q_2 + q_0q_3), q_0^2 + q_1^2 - q_2^2 + q_3^2) \end{bmatrix} \qquad (2.42)$$

These relations result in angle values in units of radians.

An estimation algorithm was considered in the research because of the bias, drift errors, and random noise effects noticed on the orientation angles acquired earlier in this chapter. A literature review showed that the conventional estimator used in aerospace and computer graphics to estimate the quaternion (Orientation) state of a coordinate frame is the Extended Kalman Filter.

# Chapter 3: ATTITUDE ESTIMATION USING EXTENDED KALMAN FILTER

In this research, attitude estimation using the extended Kalman Filter (EKF) is used for sensor fusion between the inertial sensors because the previous results from the equilibrium state experiment shown in Chapter 2 clarify the effect of gyroscope drift problems due to integration of noise. Other systems' noise-related factors are temperature variation, misalignment errors, and miscalculated biases. Furthermore, since angular velocities obtained from gyroscopes are integrated to produce angles to express orientation, the initial conditions have to be known. A solution to that problem is to use the angles obtained from accelerometers and magnetometers as the initial conditions.

Based on optimal estimation theory, the Extended Kalman Filter is a recursive optimal estimator that can be used for non-linear system state estimation [26]. Two Extended Kalman Filter designs were studied and implemented to estimate the orientation of each sensor module.

## 3.1 Sensor Measurement Models

The measurement modeling phase is a critical step in order for the Kalman Filter/estimator to operate accurately. The sensors' measurement models are discussed for each sensor as follows:

#### 3.1.1.1 Gyroscope Measurement Model

The angular velocity model of the gyroscope can be expressed by equation(3.1),

$$\omega_{measured} = \omega_{true} + b_s + b_d + v_g \tag{3.1}$$

such that:

$$\omega_{measured} = \begin{bmatrix} g_x \\ g_y \\ g_z \end{bmatrix} = \begin{bmatrix} p \\ q \\ r \end{bmatrix} \tag{3.2}$$

$b_s$ is static gyroscope biases (offset)

which expresses the measured angular velocities vector using the gyroscope triplet group.

Also

$$b_d = \begin{bmatrix} b_p \\ b_q \\ b_r \end{bmatrix} \tag{3.3}$$

Vector $b_d$ is the dynamic bias vector for each of the three axes' measured angular rates. In addition, $v_g$ is the noise vector.

On the other hand, a set of sensor data is averaged by the software algorithm at the beginning of each data acquisition session to compute static biases, as stated in Chapter 2. Then, each sensor measurement is subtracted from the calculated static bias (offset) using:

$$\omega_{compensated} = \omega_{measured} - b_{static} \tag{3.4}$$

The noise statistical parameters for the gyroscope measurements were calculated experimentally using reference data due to equilibrium. Noise is modeled as the zero-mean uncorrelated white Gaussian noise$v_g$, and variances are used for initializing the covariance matrices in the EKF algorithm.

The measurement model expressed by equation (3.1) does not take sensor misalignments, temperature compensation and cross-axis dependencies into consideration. This assumption was used because of the nature of the MEMS gyroscopes embedded in the analog device’s inertial measurement unit (ADIS16355) being used, which has minimal misalignment errors as well as temperature compensation throughout its temperature range (Appendix A).

### 3.1.1.2 Accelerometer Measurement Model

The measurement modeling equation for the accelerometer reading is:

$$a_{measured} = a_{true} - b_a + v_a \tag{3.5}$$

$$a_{measured} = \begin{bmatrix} a_x \\ a_y \\ a_z \end{bmatrix} \tag{3.6}$$

The vector $a_{measured}$ is the accelerometer's measured values vector. Also the vector $b_a$ is the bias vector, and $v_a$ is the noise vector by analogy to the gyroscope's measurement model.

The static bias vector $b_a$ affects tilt measurement for the magnetometer compensation as well as measures both the Roll angle and the Pitch angle in the EKF. This static bias is also computed by averaging the first set of data measurements before any acquisition session, by analogy to the gyroscope static biases.

Furthermore, other models include the compensation due to earth's centripetal acceleration with the accelerometer and gyroscope models. However, since this acceleration is so small that low-cost sensors cannot sense it, it was not considered during the modeling.

Accelerometer measurement noise was analyzed in order to use the variance in the EKF measurement covariance matrices initialization.

#### 3.1.1.3 Magnetometer Measurement Model

The equation governing each of the three magnetometers can be expressed by:

$$m_{measured} = m_{true} + d_m + v_m \tag{3.7}$$

such that:

$$m_{measured} = \begin{bmatrix} m_x \\ m_y \\ m_z \end{bmatrix} \tag{3.8}$$

The vector $m_{measured}$ is the actual sensor values streaming from the magnetometer triad. Furthermore, vector $d_m$ includes the magnetic disturbances that affect measuring true magnetic field of earth. Magnetic noise can be classified into the so-called soft iron and hard iron interferences [31]. The soft iron disturbances are induced through the reflection of magnetic and electromagnetic field applications. The hard iron disturbances are external magnetic fields generated by the surrounding sources such as transformers, lighting systems, cellular phones and iron core materials. Accelerometer tilt measurements are used to compensate for the magnetic dip-angle effect on the magnetometers, as described in previous chapters. In addition, other noise sources are modeled as $v_m$ , zero-mean uncorrelated white Gaussian noise.

## 3.2 Euler-based Orientation Estimation Algorithm

This algorithm uses the measured Euler angles given by accelerometers and magnetometers to compensate for the gyroscope's dynamic drift. Experiments also showed that it is advantageous to add more dependency on the gyro-based orientation angles in dynamic states. On the other hand, Euler angles should be calculated using accelerometers and magnetometers in static and slowly moving states.

### 3.2.1 Euler Angles Estimator Design

A rotational transformation between two successive frames in time can be expressed by the differential equation. The measured angular velocities p, q and r relate to the angular velocities in terms of Euler angles [26] by:

$$\begin{bmatrix}\dot{\phi}\\ \dot{\theta}\\ \dot{\psi}\end{bmatrix}=\begin{bmatrix}1 & s\phi t\theta & c\phi t\theta\\ 0 & c\phi & -s\phi\\ 0 & \left(\frac{s\phi}{c\theta}\right) & \left(\frac{c\phi}{c\theta}\right)\end{bmatrix}\begin{bmatrix}p\\ q\\ r\end{bmatrix} \tag{3.9}$$

such that s, c, and t are abbreviations for the sine, cosine, and tan functions respectively.

#### 3.2.1.1 System State Model

The system state vector to be estimated is composed of the six elements: the three Euler angles and three dynamic biases of the gyroscope, as shown in:

$$X_{k+1} = \begin{bmatrix} \phi \\ \theta \\ \psi \\ b_p \\ b_q \\ b_r \end{bmatrix} = F_k . x_k + \omega_k \tag{3.10}$$

To determine the state transition matrix F, the Jacobian of equation (3.9) is derived as:

$$F_k = J \begin{bmatrix} p + q(s\phi t\theta) + r(c\phi t\theta) \\ q(c\phi) - r(s\phi) \\ q\left(\frac{s\phi}{c\theta}\right) + r\left(\frac{c\phi}{c\theta}\right) \end{bmatrix}_{[\phi,\theta,\psi,b_p,b_q,b_r]} \tag{3.11}$$

The system state noise $\omega_k$ is modelled as the Gaussian noise with zero mean and variance Q ($\omega_k \approx N(0, Q)$). The covariance matrix Q holds the variances of the state vector elements in the three frame axes, assuming decoupled effects as follows:

$$Q_{6\times6} = \begin{bmatrix} \Sigma_E & 0_3 \\ 0_3 & \Sigma_b \end{bmatrix} \tag{3.12}$$

such that :
$$\Sigma_E = \begin{bmatrix} \sigma_\phi^2 & 0 & 0 \\ 0 & \sigma_\theta^2 & 0 \\ 0 & 0 & \sigma_\psi^2 \end{bmatrix}$$

and
$$\Sigma_E = \begin{bmatrix} \sigma_{b_p}^2 & 0 & 0 \\ 0 & \sigma_{b_q}^2 & 0 \\ 0 & 0 & \sigma_{b_r}^2 \end{bmatrix}$$

The values of these variances were calculated experimentally by keeping the sensor in equilibrium for a sufficient time and studying its statistical characteristics.

#### 3.2.1.2 System Measurement Model

The measurement model is composed of the Euler angle measurements corrupted with the noise vector $v_k$ shown as:

$$Z_{k+1} = \begin{bmatrix} \phi \\ \theta \\ \psi \\ 0 \\ 0 \\ 0 \end{bmatrix} = H_{k+1} + v_{k+1} \tag{3.13}$$

The Euler angles acquired here are roll (φ) and pitch (θ) from accelerometers, and Yaw (ψ) from the tilt compensated magnetometers. Also, $v_k$ is the measurement noise modeled as Gaussian noise with zero mean and variance R (i.e. $v_{k+1} \approx N(0, R)$). The measurement covariance matrix R is given in (3.13):

$$R = \begin{bmatrix} \Sigma_E & 0_{3\times3} \\ 0_{3\times3} & 0_{3\times3} \end{bmatrix} \tag{3.14}$$

### 3.2.1.3 Prediction and Update

Prediction starts by estimating the system state using:

$$X_{k+1}^{-} = F_k \cdot X_k \tag{3.15}$$

The system state error covariance estimate (Continuous time update) is:

$$P_{k+1}^{-}{}' = F_k \cdot P_k + P_k \cdot F_k^T + Q \tag{3.16}$$

The error covariance is then updated by:

$$P_{k+1}^{-} = P_{k+1}^{-}{}' + P_{k+1}^{-}{}' \cdot T_s \tag{3.17}$$

such that $T_s$ is the sampling time.

Furthermore, the Kalman Gain is determined through the following relation:

$$K_{k+1} = P_{k+1}^{-} \cdot H_{k+1}^{T}(H_{k+1} \cdot P_{k+1}^{-} \cdot H_{k+1}^{T} + R_{k+1})^{-1} \tag{3.18}$$

The update phase of the Kalman Filter algorithm is made by using the following two equations:

$$\hat{X}_{k+1} = X_{k+1}^{-} + K_{k+1} \cdot (error) \tag{3.19}$$

such that the "$error$" term is calculated as the difference between the measured Euler angle and its estimated value given from the previous state.

$$\hat{P}_{k+1} = P_{k+1}^{-} - K_{k+1} \cdot H_{k+1} \cdot P_{k+1}^{-} \tag{3.20}$$

### 3.2.2 Estimator Experimental Results

Practical results showed that the estimated roll and pitch angles converge efficiently to the reference ones. However, the yaw angle showed instabilities because the lab environment has affected the modeling statistics of the magnetometers by hard and soft iron disturbances. The experimental results are shown in Figure 3.1 through Figure 3.6, comparing the performance of the developed sensor with the performance of an industrial-grade AHRS (Microstrain GX2). The developed inertial sensor module was fixed onto the reference AHRS as shown in Chapter 5 section 3.

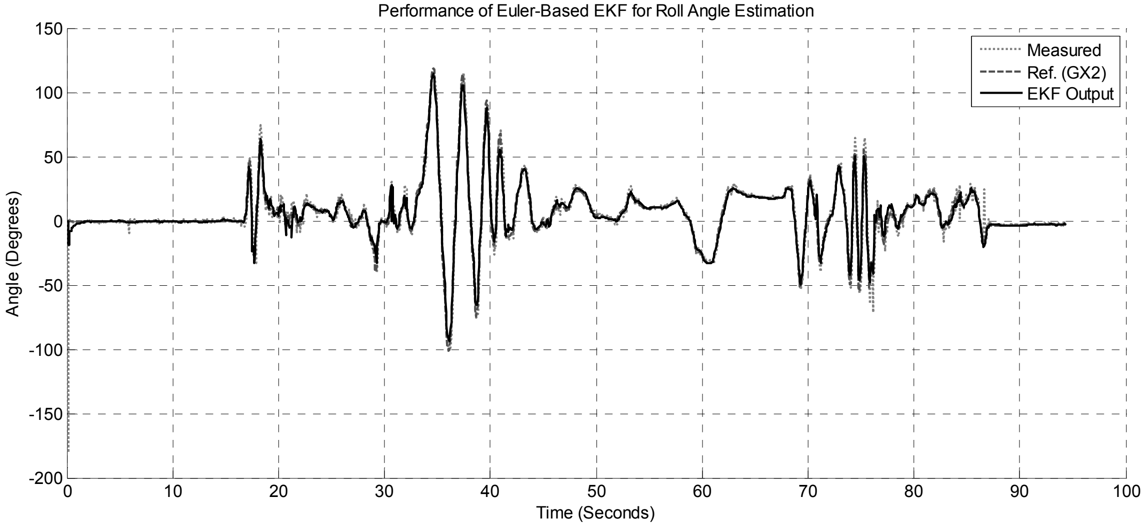

Figure 3.1: Estimated-roll using Euler-based EKF

In order to show the Euler-based EKF performance more efficiently, a zoomed-in version on the time interval between the 50th and the 60th seconds is shown in Figure 3.2.

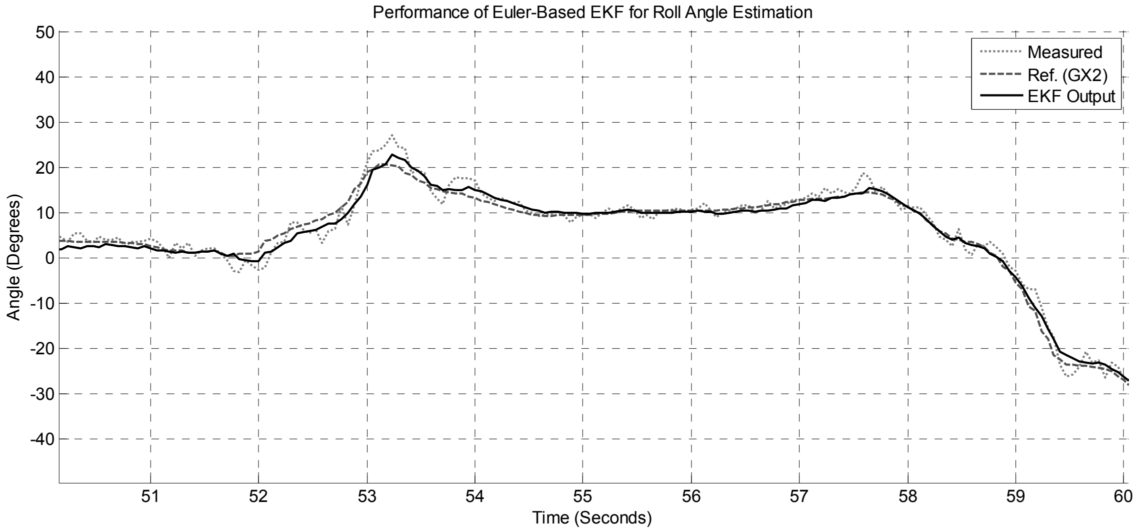

Figure 3.2: Zoomed estimated-roll angle using Euler-based EKF

Continuing using the same scheme of figures, the Pitch angle EKF performance is shown in Figure 3.3 and the selected time-interval zoom-in is shown in Figure 3.4.

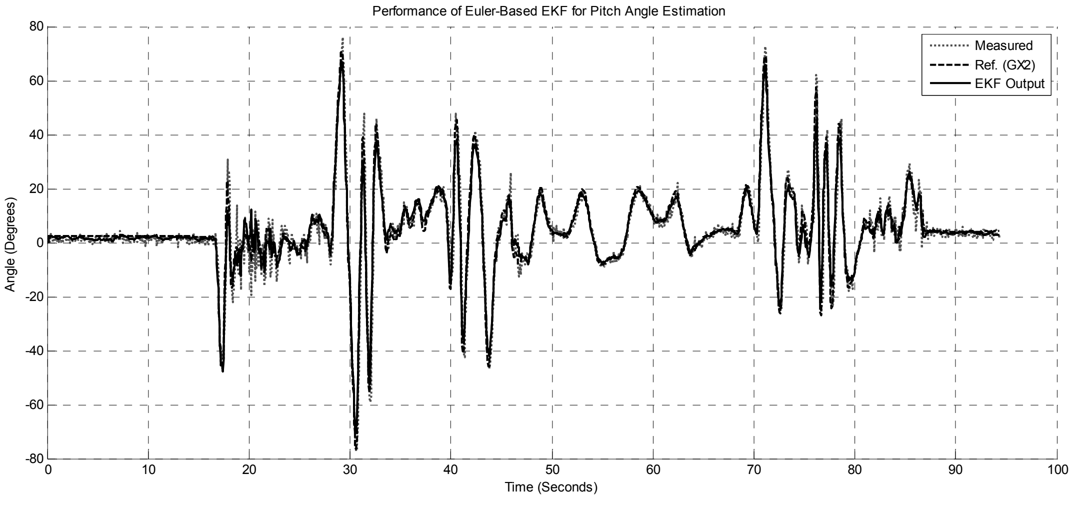

Figure 3.3: Estimated-pitch using Euler-based EKF

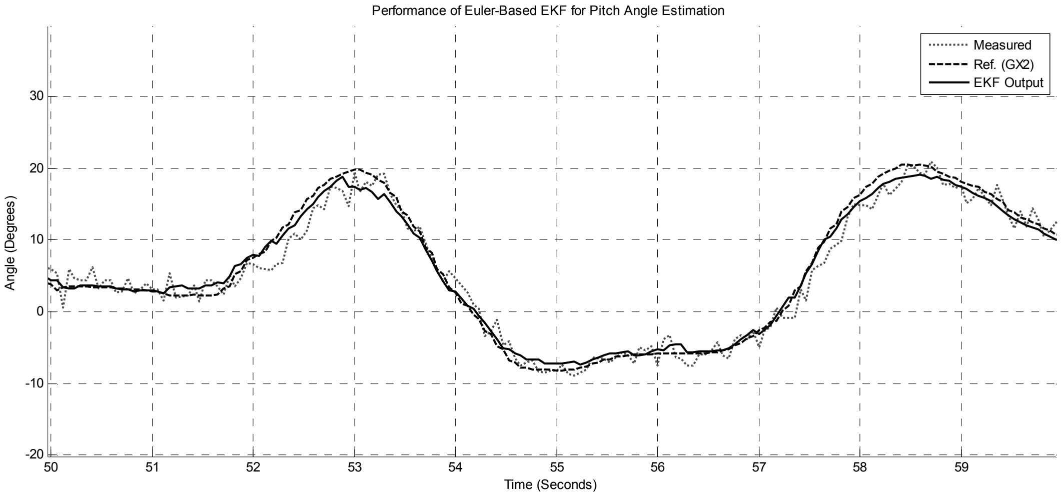

Figure 3.4: Zoomed estimated-pitch angle using Euler-based EKF

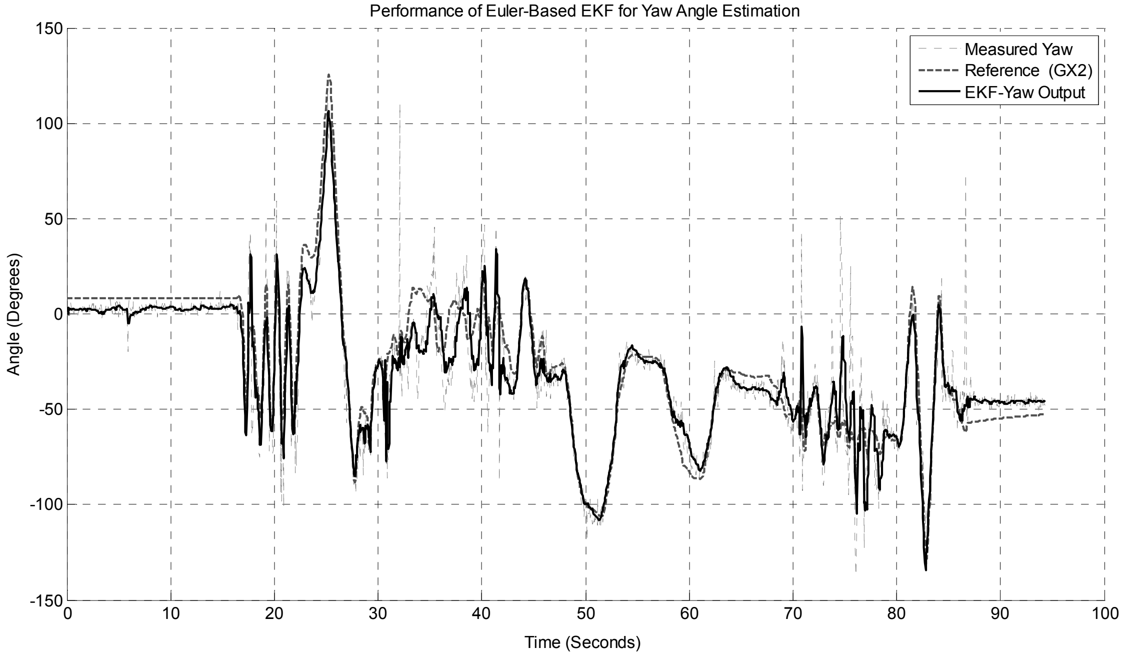

Figure 3.5: Estimated-yaw angle using Euler-based EKF

Lastly, the zoomed time-interval-section from Figure 3.5 is shown in Figure 3.6.

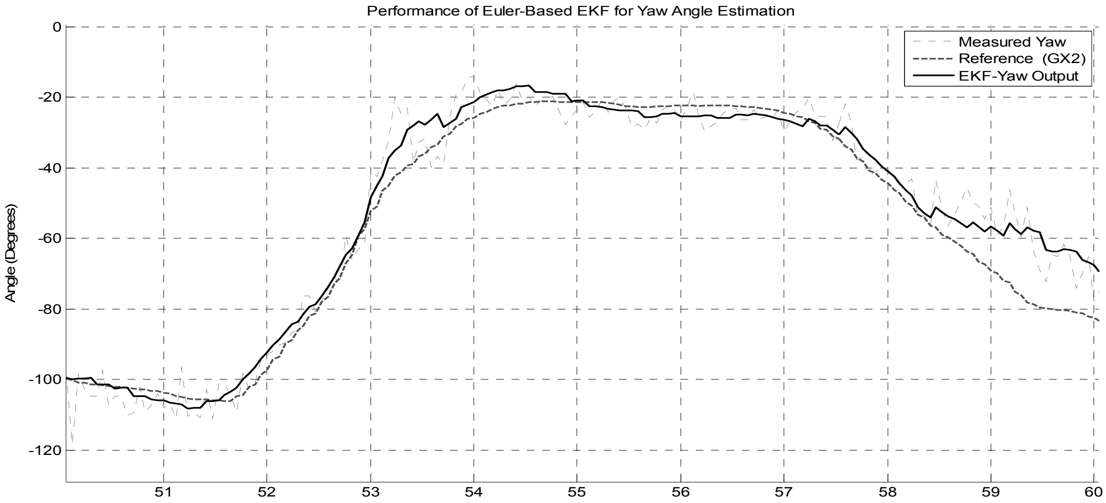

Figure 3.6: Zoomed estimated-yaw angle using Euler-based EKF

The error analysis studies for the previous results are summarized in Table 3.1:

Table 3.1: Error analysis for the Euler-based EKF estimator results

| **Orientation Angle Error** | **Mean Error (deg)** |
|---|---|
| φ | 3.2287 |
| θ | 2.9146 |
| Ψ | 10.8224 |

Singularities form a major problem that appears when using Euler angles. The system singularities are at a pitch angle of ±90 degrees because the roll angle will be in phase with the yaw axis. Another reason is that at these pitch angles, accelerometer axes z and y will be perpendicular to earth's gravity vector, causing the trigonometric functions to divide by zero, resulting in singularities. A common solution for this problem is to use quaternions.

## 3.3 Quaternion-based Orientation Estimation Algorithm

The EKF used here acts as a complementary/indirect filter to the general kinematics calculation algorithm because it focuses on error analysis as well as the state estimation. The estimator structure, system state space model and results are shown in the sequence presented throughout this chapter.

The extended EKF was applied to combine the three-dimensional accelerometers, magnetometer and gyroscopes sensor data.

The accelerometer measurements and magnetometer measurements are combined to cancel out the tilt affecting magnetometer readings using the acceleration due to earth's gravity. Furthermore, data of all the nine sensors are sent simultaneously to the extended Kalman Filter estimator. Then the estimator relies on the statistics calculated prior to the experiment during the calibration phase to adjust the gains weighing the system dependence on sensor values for each orientation angle based on the nature of the motion with respect to the error analysis.

### 3.3.1 Quaternion Estimator Design

The equation relating the derivatives of the quaternion to the angular velocities [26] is given by:

$$\begin{bmatrix} \dot{q}_0 \\ \dot{q}_1 \\ \dot{q}_2 \\ \dot{q}_3 \end{bmatrix} = \begin{bmatrix} 0 & -p & -q & -r \\ p & 0 & r & -q \\ q & -r & 0 & p \\ r & q & -p & 0 \end{bmatrix} \begin{bmatrix} q_0 \\ q_1 \\ q_2 \\ q_3 \end{bmatrix} \tag{3.21}$$

This data can also be written as:

$$\dot{q} = \left(\frac{1}{2}\right) \cdot \Omega(p, q, r) \cdot q \tag{3.22}$$

such that the angular velocity matrix $\Omega(p, q, r)$ can be driven in terms of the gyroscopes measurements as:

$$\Omega(p, q, r) = \begin{bmatrix} 0 & -p & -q & -r \\ p & 0 & r & -q \\ q & -r & 0 & p \\ r & q & -p & 0 \end{bmatrix} \tag{3.23}$$

This relation is used in the software algorithm to update the orientation state vector in the discrete form using:

$$q_{k+1} = q_k + \dot{q}_k \, T_s \tag{3.24}$$

Where $q_{k+1}$ is the updated quaternion state at time step k+1, and $T_s$ is the sampling time.

#### 3.3.1.1 System State Model

The state vector used in this research is composed of a quaternion along with the dynamic gyroscope biases, as expressed by (3.25) and (3.26).

$$X_{k+1} = F_k \cdot X_k + \omega_k \tag{3.25}$$

such that the state vector is

$$X_k = \begin{bmatrix} q_{0_k} \\ q_{1_k} \\ q_{2_k} \\ q_{3_k} \\ b_{p_k} \\ b_{q_k} \\ b_{r_k} \end{bmatrix} \tag{3.26}$$

The vector $X_{k+1}$ corresponds to the derivative of the state vector, given that the gyro-dynamic biases $b_p$, $b_q$ and $b_r$ are constants, leading their derivatives to be zeros as shown in(3.27).

$$X_{k+1} = \begin{bmatrix} q_{0_{k+1}} \\ q_{1_{k+1}} \\ q_{2_{k+1}} \\ q_{3_{k+1}} \\ 0 \\ 0 \\ 0 \end{bmatrix} \tag{3.27}$$

Also, F is the system state transition matrix of the quaternion calculated as:

$$F_k = J(X_{k+1})_{X_k} \tag{3.28}$$

The function $J(X_{k+1})_{X_k}$ is defined as the Jacobian of the state vector at time step k+1 with respect to the state vector at time step k.

This leads the state transition function *F* to be as shown in (3.29).

$$F_k = \left(\frac{1}{2}\right)\begin{bmatrix} 0 & -p & -q & -r & q_1 & q_2 & q_3 \\ p & 0 & r & -q & -q_0 & q_3 & -q_2 \\ q & -r & 0 & p & -q_3 & -q_0 & q_1 \\ r & q & -p & 0 & q_2 & -q_1 & -q_0 \\ 0 & 0 & 0 & 0 & 0 & 0 & 0 \\ 0 & 0 & 0 & 0 & 0 & 0 & 0 \\ 0 & 0 & 0 & 0 & 0 & 0 & 0 \end{bmatrix} \tag{3.29}$$

The vector $\omega_k$ in the state model resembles the error vector. It is also characterized by the system states error covariance matrix *Q* as:

$$Q = \begin{bmatrix} 0_{4\times4} & 0_{3\times3} \\ 0_{4\times4} & \sigma_g^2 \cdot I_{3\times3} \end{bmatrix} \tag{3.30}$$

The scalar value $\sigma_g^2$ denotes the variances of the gyroscopes calculated by obtaining the angular rate data in static conditions. In this case, it is assumed to be the variance of the dynamic gyro-biases, too.

#### 3.3.1.2 System Measurement Model

Following the same procedure taken in designing the system state model, the measurement model is:

$$Z_{k+1} = H_k + v_{k+1} \tag{3.31}$$

Vector $H$ denotes the error measurements, and it is updated with every iteration to correct the state vector given the measured quaternion and Euler angles. The sequence of this updating procedure is discussed in the next section.

The noise $v_{k+1}$ is modeled as white Gaussian noise with zero mean and variance R (i.e.$v_{k+1} \approx N(0, R)$). The measurement covariance matrix R is composed of the variances of the measurements, that is, variances of the Euler angles. For practical experiments, these variances are assumed to be 1 because of external magnetic interferences affecting the calculation of variances, specifically the yaw angle.

These preliminary results show that the orientation angles are better obtained using magnetometers and accelerometers in steady state. Nevertheless, the gyroscope results showed more efficiency in the dynamic states because of the addition of linear acceleration to the accelerometers.

#### 3.3.1.3 Prediction and Update

The prediction and update steps are made using the following set of equations [31]:

Prediction starts by estimating the system state using:

$$X_{k+1} = F_k \cdot X_k \tag{3.32}$$

The system state error covariance estimate is:

$$\hat{P}_{k+1}^{-}{}' = F_k \cdot P_k + P_k \cdot {F_k}^T + Q \tag{3.33}$$

The update phase of the estimator uses a sequence of the Euler angles measurements. The error measurements are updated as:

Roll error update:

$$H_{\varphi_{k+1}} = \begin{bmatrix} {q_1}_{k+1}\, {DCM_{33}}_{k+1}\, {\varphi_{error}}_{k+1} \\ ({q_0}_{k+1}\, {DCM_{33}}_{k+1} \ + 2\, {q_1}_{k+1}\, {DCM_{23}}_{k+1}){\varphi_{error}}_{k+1} \\ ({q_3}_{k+1}\, {DCM_{33}}_{\ k+1} + 2\, {q_2}_{\ k+1} {DCM_{23}}_{k+1}){\varphi_{error}}_{k+1} \\ {q_2}_{k+1}\, {DCM_{33}}_{k+1}\, {\varphi_{error}}_{k+1} \end{bmatrix} \tag{3.34}$$

Pitch error update:

$$H_{\theta_{k+1}} = \begin{bmatrix} {q_2}_{k+1}\, {\theta_{error}}_{k+1} \\ -{q_3}_{k+1}\, {\theta_{error}}_{k+1} \\ {q_0}_{k+1}\, {\theta_{error}}_{k+1} \\ -{q_1}_{k+1}\, {\theta_{error}}_{k+1} \end{bmatrix} \tag{3.35}$$

Yaw error update:

$$H_{\psi_{k+1}} = \begin{bmatrix} {q_3}_{k+1}\, {DCM_{11}}_{k+1}\, {\psi_{error}}_{k+1} \\ {q_2}_{k+1} {DCM_{11}}_{k+1}\, {\psi_{error}}_{k+1} \\ ({q_2}_{k+1}\, {DCM_{11}}_{k+1} \ + 2\, {q_2}_{k+1}\, {DCM_{12}}_{k+1}){\psi_{error}}_{k+1} \\ ({q_1}_{k+1}\, {DCM_{11}}_{\ k+1} + 2\, {q_2}_{\ k+1} {DCM_{12}}_{k+1}){\psi_{error}}_{k+1} \end{bmatrix} \tag{3.36}$$

The terms $\varphi_{error}$, $\theta_{error}$ and $\psi_{error}$ are calculated from the estimated quaternion via the directional cosine matrix (DCM). Equations (3.37) through (3.39) show the procedure of calculating those angle errors.

$$\varphi_{error} = \left(\frac{2}{DCM_{33}^2 + DCM_{23}^2}\right) \tag{3.37}$$

$$\theta_{error} = \left(\frac{2}{\sqrt{1-DCM_{13}^2}}\right) \tag{3.38}$$

$$\psi_{error} = \left(\frac{2}{DCM_{11}^2 + DCM_{12}^2}\right) \tag{3.39}$$

Continuing the update phase, the error covariance is then updated by:

$$\hat{P}_{k+1}^{-} = \hat{P}_{k+1}^{-\,\prime} + \hat{P}_{k+1}^{-\,\prime} \cdot T_s \tag{3.40}$$

We see that the Kalman Gain is determined through:

$$K_{k+1} = \hat{P}_{k+1}^{-} \cdot H_{k+1}^{T}(H_{k+1} \cdot \hat{P}_{k+1}^{-} \cdot H_{k+1}^{T} + R_{k+1})^{-1} \tag{3.41}$$

Next, the state vector update is given by:

$$X_{k+1} = X_{k+1} + K_{k+1}[Angle_{Measured} - Angle_{Estimated}] \tag{3.42}$$

It is worth noting that the quaternion part of the state vector has to be normalized past this point.

$$P_{k+1} = \hat{P}_{k+1}^{-} - K_{k+1} \cdot H_{k+1} \cdot \hat{P}_{k+1}^{-} \tag{3.43}$$

### 3.3.2 Estimator Experimental Results

The experimental results shown next were sampled from the implemented sensor module compared to a factory calibrated AHRS(GX2) manufactured by Microstrain, both sensors are shown in Chapter 5. Each angle is shown over the measurement time succeeded by a zoomed-in version for the time interval between the 50th and 60th seconds for clarity.

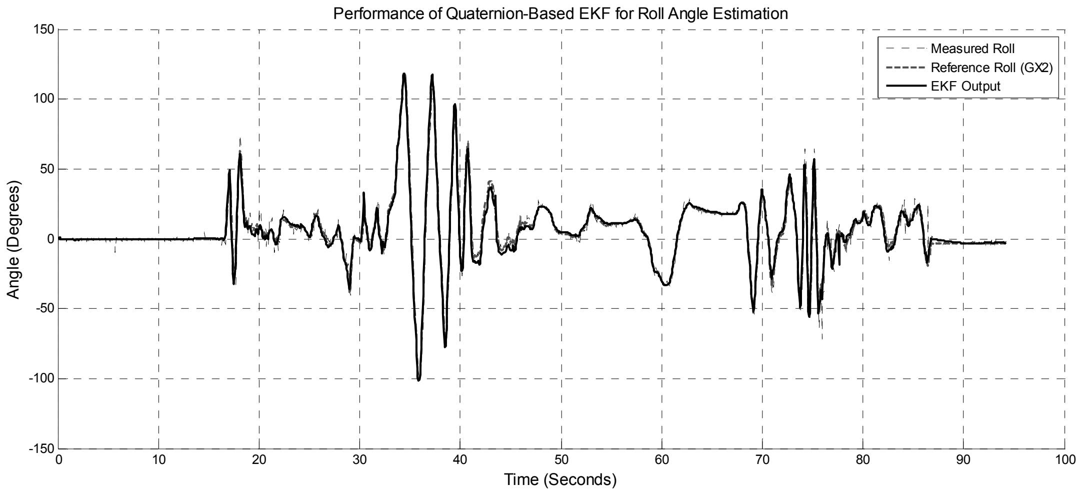

Figure 3.7: Estimated-roll using quaternion-based EKF

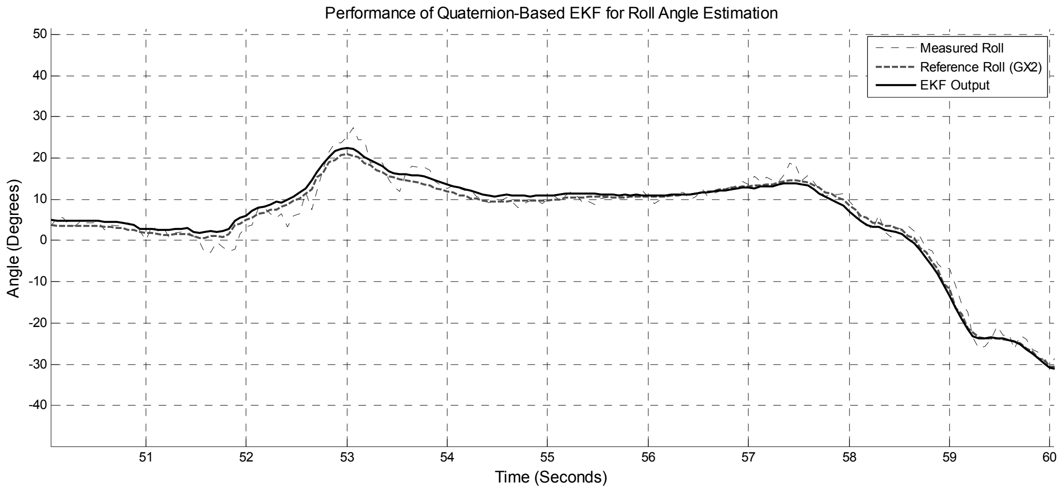

Figure 3.8: Zoomed estimated-roll angle using quaternion-based EKF

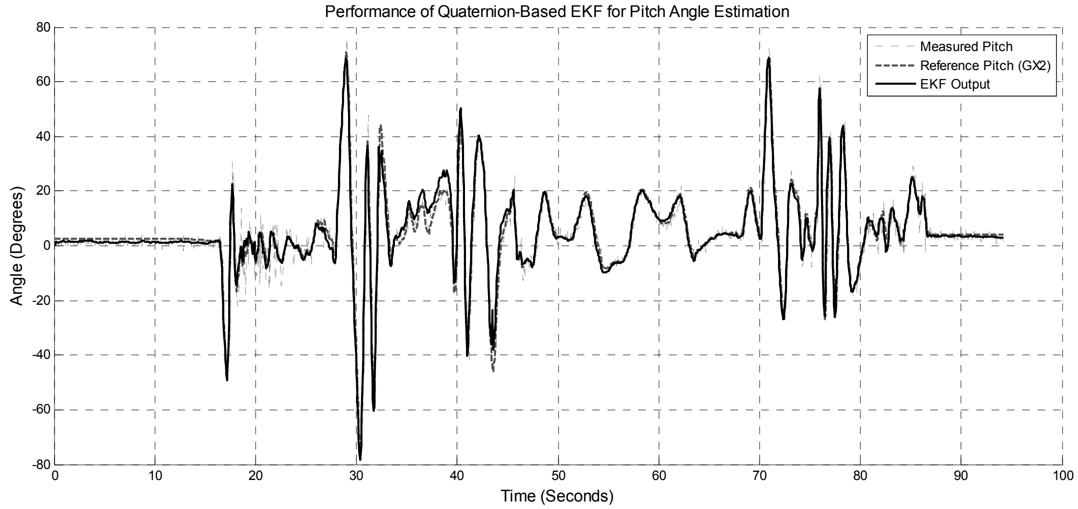

Figure 3.9: Estimated-pitch using quaternion-based EKF

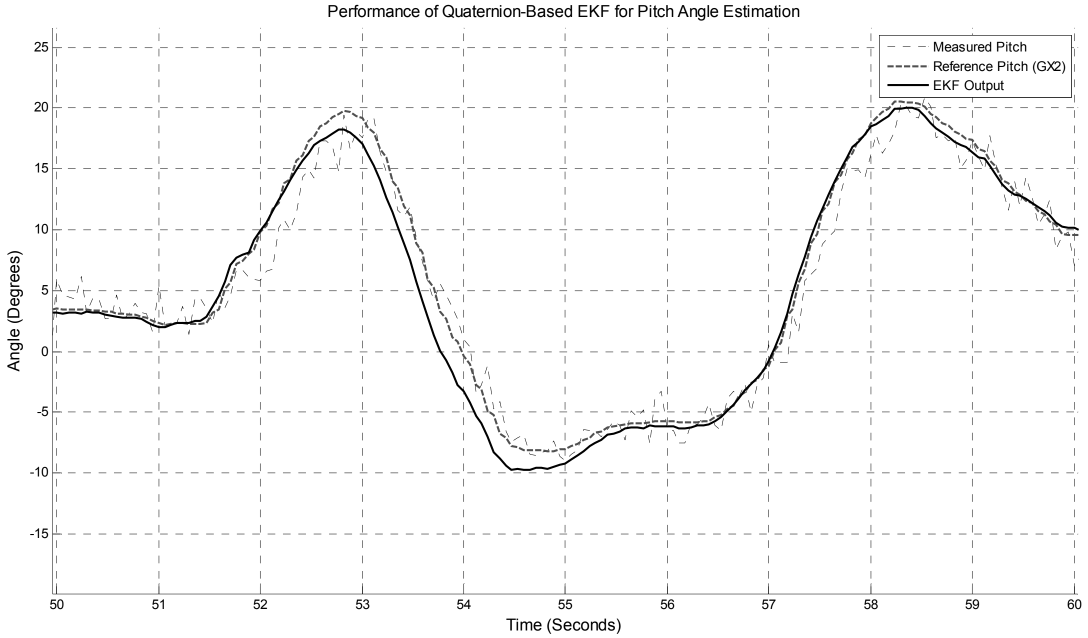

Figure 3.10: Zoomed estimated-pitch angle using quaternion-based EKF

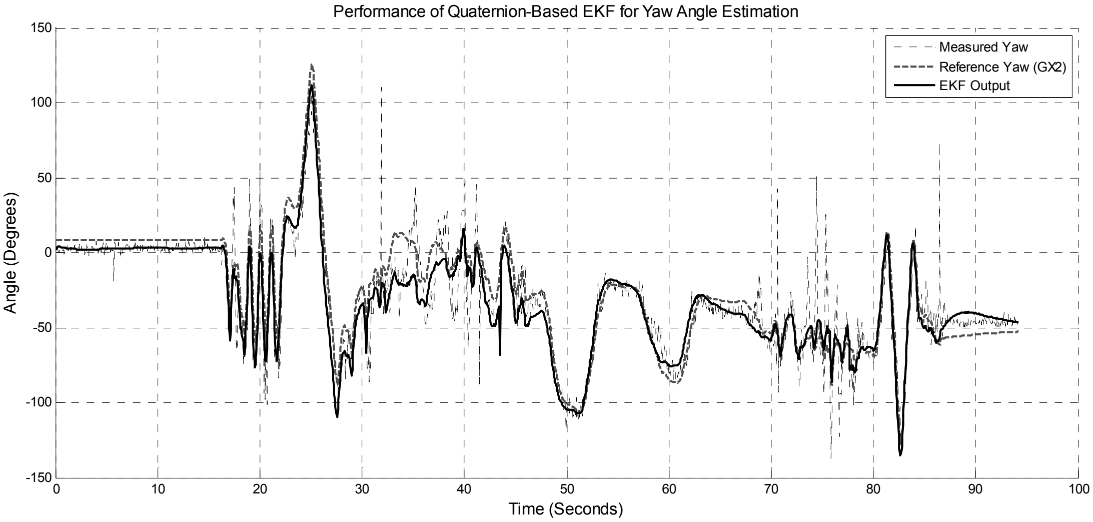

Figure 3.11: Estimated-yaw using quaternion based EKF

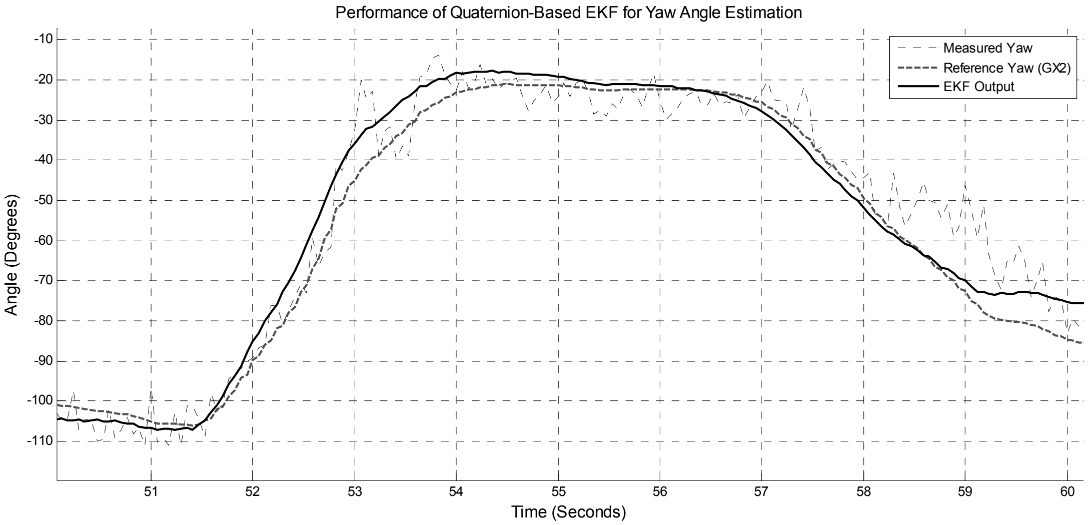

Figure 3.12: Zoomed estimated-yaw angle using quaternion-based EKF

Error analysis results are summarized in Table 3.2.

Table 3.2: Error analysis for the quaternion EKF estimator results

| Orientation Angle Error | Mean Error (deg) |
|---|---|
| φ | 1.7051 |
| θ | 1.8102 |
| Ψ | 8.9811 |

It is clear that the yaw angle estimation suffered relatively large angle deviations because of the magnetic sensor interferences. To overcome these noises, typical calibration algorithms have been developed, as in [32]. These algorithms have not been explored in this research; they are considered in future work and recommendations.

# Chapter 4: HUMAN ARM BIOMECHANICAL MODEL

Human upper extremities are elements of a highly complicated mechanical structure. The human body bone mechanism contains about 126 degrees of freedom, as noted by Arisawa and Sato [33]. Since more than two actuators (muscles) actuate each degree of freedom of the human body, the exact modelling of the arm has not been easily achieved. Using an approximate biomechanical model of the bone-structure of the arm, one can obtain further knowledge of the system parameters such as position, orientation and relative velocities. The priority of the mathematical model is to emulate the real-arm structure with minimum errors to demonstrate the most important features. Early models of the human arm simplify the human arm motion as two-dimensional. The arm model has usually been modelled as two rigid bodies linked together with two joints without considering friction.

Since the human arm model can be approximated as a serial-linked robot, several approaches were made to use a network of inertial and pressure sensors to model the human skeleton, as described in [34]. Kurata et. al. [35] used only a set of accelerometers mounted on the arm to model joint angles. In addition, most of the research groups used the Extended Kalman Filter as a complementary error estimator instead of estimating the states themselves [18].

In this Chapter, the human arm kinematics is described thoroughly for each degree of freedom. The forward kinematics is done using the Homogenous Transformation, Denavit Hartenberg's convention and Dual Quaternion methods. In practice, these methods describe three-dimensional transformations using the joint angles acquired by the inertial measurement units and estimated by the EKF mentioned in Chapter 3.

## 4.1 Model Structure and Description

The human arm can be modeled as a three-links, nine Degrees of freedom (DOFs) serial robot manipulator [36]. The arm model used in this research was also used by Mark Treiber [37] following the work done by Lenarcic and A Umek [38], as shown in Figure 4.1.

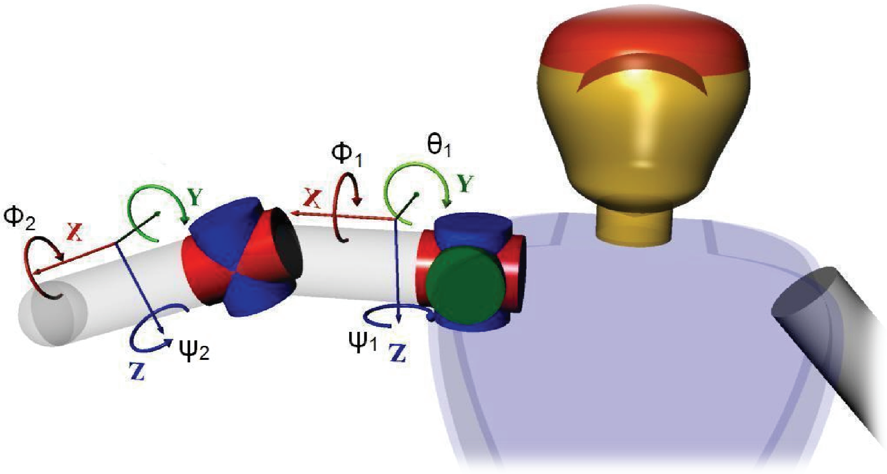

Figure 4.1: Human arm biomechanical model

The human arm model used in this research considers five DOFs, because the inertial sensors will not be to be able to accurately measure prismatic joints attached between the shoulder and the torso. Prismatic joints position can be determined by using double integration of acceleration, which will cause a rapid growing error with time. Since both prismatic joints have a relatively small effect on the total work space, they were ignored in the model. To minimize the number of sensors and, consequently, reduce the cost of the system, the wrist joint has also been ignored. Another reason for ignoring it is that its limited working space with respect to the whole human arm means that position can be estimated with less expensive sensors such as flex sensors [14].

Each joint of the human arm model is described as shown in Table 4.1. In the homogeneous transformation method rotation matrices are used directly to calculate forward kinematics. However, since each sensor measures orientation globally with respect to Earth's NED frame, the obtained rotation matrices had to be transformed to the local coordinate frame of the arm when using the DH or the DQ conventions. This is because the DH table considers that each joint angle of the arm is relative to the previous link (i.e. local coordinate frames). The joint angle calculations are described relatively in their corresponding sections.

Table 4.1: Joint angles description for the human arm model

| Joint | Resemblance | Joint Type | Corresponding Joint Angles | |
|---|---|---|---|---|
| 1. | Shoulder | 1-Spherical joint (Ball joint) | 3 | $\Theta_1$ |
| | | | | $\Theta_2$ |
| | | | | $\Theta_3$ |
| 2. | Elbow | 2- Perpendicular Revolute joints (Pin Joints) | 2 | $\Theta_4$ |
| | | | | $\Theta_5$ |

The following sections show the used methods for local positioning and orientation tracking of the arm.

## 4.2 Homogenous Transformation Method

This method follows relations initially derived for implementing forward kinematics in the robotics field. However, some adaptations had to be made to incorporate inertial sensor data into the model. This section is divided into two subsections: the model and methodology to derive the orientation and position of each arm link, and experimental results.

Consider the model shown in Figure 4.2; both frames {S$_1$} and {S$_2$} are attached to the inertial sensor modules mounted on the arm. In practice, both frames are measured with respect to the global frame {U}, which is fixed on the shoulder.

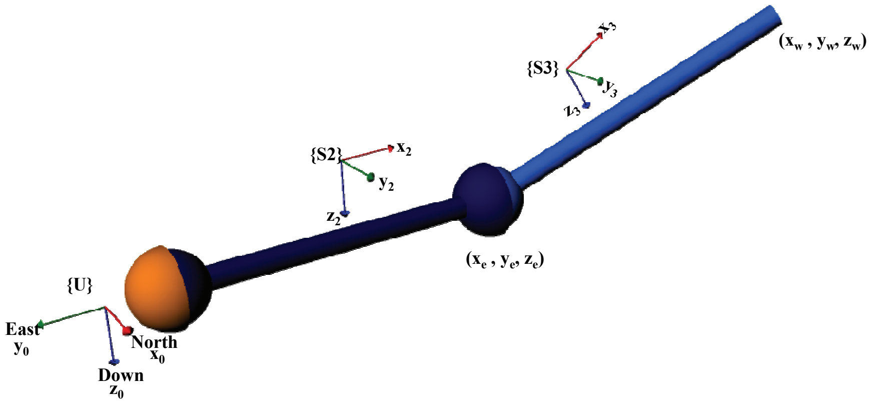

Figure 4.2: Forward kinematics using Homogenous Transformation

The initial condition of the arm is assumed aligned with universal frame {U} as shown in Figure 4.3. Given that the upper arm link length is the distance $L_u$, the position vector pointing from the shoulder center point to the elbow also has magnitude $L_u$. The forearm length is given by $L_F$.

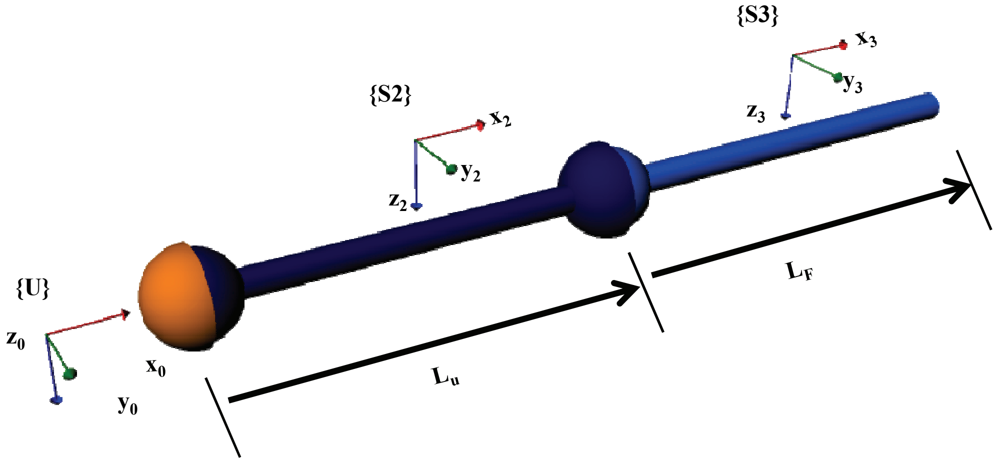

Figure 4.3: Arm model initial condition

In the initial condition of the position vector is given by:

$$P_e = \begin{bmatrix} L_u \\ 0 \\ 0 \end{bmatrix} \tag{4.1}$$

As the upper arm starts to rotate about the center of the shoulder spherical joint, the new orientation of position vector $P_e'$ is given by:

$$P_e' = R_2^U \cdot P_e \tag{4.2}$$

such that the rotation matrix $R_2^U$ is the matrix relating the orientation of the frame attached to upper arm (i.e. sensor module 1 rotation matrix) with the global frame {U}. This rotation matrix is with respect to the XYZ fixed frame, and is written as:

$$ {}_{2}^{U}R_{XYZ}(\varphi,\theta,\psi) = \begin{bmatrix} c\psi c\theta & c\psi s\theta s\varphi - s\psi c\varphi & c\psi s\theta c\varphi + s\psi s\varphi \\ s\psi c\theta & s\psi s\theta s\varphi + c\psi c\varphi & s\psi s\theta c\varphi - c\psi s\varphi \\ -s\theta & c\theta s\varphi & c\theta c\varphi \end{bmatrix} \tag{4.3} $$

such that the angles $\varphi, \theta, and\ \psi$ are roll, pitch and yaw measured by sensor module 1, respectively. It is also worth noting that the same rotation matrix denotes the orientation of the position vector $P_e'$. The combined rotation and translation for that position vector can be denoted by the transformation matrix $T_e$ written as:

$$ T_2^U = \begin{bmatrix} {}_{2}^{U}R_{XYZ} & P_e' \\ 0_{1x3} & 1 \end{bmatrix} \tag{4.4} $$

In addition, to calculate the position vector of the wrist (i.e. end of the forearm), a slightly different approach has to be considered, given that sensor module 2 measures absolute roll, pitch and yaw angles relative to the world frame {U}) not relative ones to frame {S2}. To calculate the position vector $P_w$, we consider its relation to frame {S2} as:

$$ {}'P_w^2 = R_3^2 \cdot P_w^2 \tag{4.5} $$

Knowing that, the rotation matrix $R_3^2$ can be calculated using

such that: $$ R_3^2 = R_2^{u^{-1}} \cdot R_3^u \tag{4.6} $$

And the vector $P_w^2$ is: $$ P_w^2 = \begin{bmatrix} L_F \\ 0 \\ 0 \end{bmatrix} \tag{4.7} $$

such that the parameter $L_F$ is the forearm length measured from the elbow to the wrist. Furthermore, combining equations (4.6) and (4.7) forms the transformation matrix $T_w^2$ as:

$$T_w^2 = \begin{bmatrix} R_3^2 & P_w^2 \\ 0_{1x3} & 1 \end{bmatrix} \tag{4.8}$$

Transforming back to frame {U} can then be done by multiplying the transformation matrices given in equation(4.4) and equation(4.8). The resulting transformation matrix describes the orientation and position of the wrist point with respect to the shoulder, written as:

$$T_w^U = T_2^U \, T_w^2 \tag{4.9}$$

such that $T_w^U$ is composed of the rotation matrix relating the position vector $P_w^U$ to the global frame {U} and undergoing translation of $P_w^U$ , which can be summarized as:

$$T_w^U = \begin{bmatrix} R_w^U & P_w^U \\ 0_{1x3} & 1 \end{bmatrix} \tag{4.10}$$

Experimental results for this algorithm are discussed in section 5 of this Chapter.

## 4.3 Forward Kinematics using Denavit-Hartenberg's Convention

The Denavit-Hartenberg's parameters have been commonly used in robotics for many years. The DH parameters describe each link of a mechanism with respect to the next [39]. In order to derive the transformation matrices based on the DH parameters, the DH algorithm has been applied on the human arm model separately from the sensor coordinate frames. Then, the relation between the assigned coordinate frames and the sensor modules coordinate frames is easily determined. As shown in Figure 4.4, the local coordinate frames are reassigned following the DH convention, noting that angle names relate to the Euler angles as stated previously inTable 4.1.

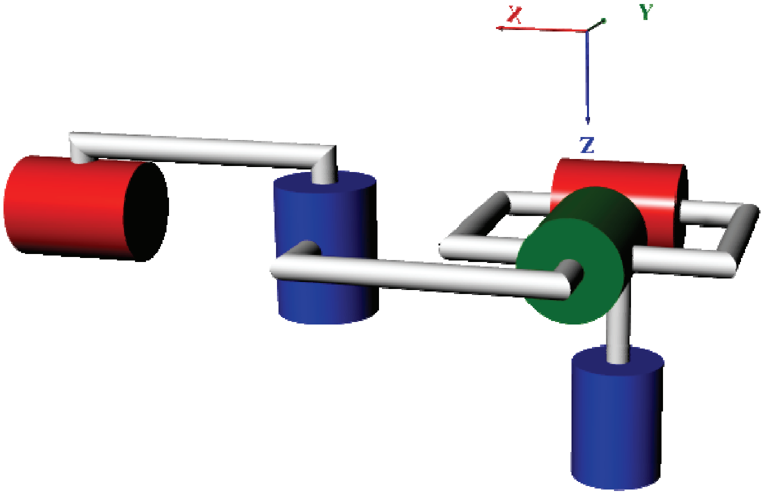

Figure 4.4: Arm model decoupled joints with assigned DH frames

Coordinate frame {0} is the base frame anchored at the shoulder (assuming patient's body is motionless). Frames {1}, {2} and {3} are the equivalent perpendicular joints to simulate a spherical joint (Ball). Furthermore, the elbow joints are expressed by frames {4} and {5} for its two degrees of freedom. Frame {n} is attached to the wrist joint center. To analyze shoulder joint angles, links of zero-lengths are assigned to each since their rotation axes intersect at a common point, which also coincides with their origin points. Moreover, the coordinate frame {1} coincides with the base coordinate frame {0} if the angle $\theta_1$ is zero. The frame assignment procedure used to obtain the DH parameters follows the standard DH convention [39].

After applying the previous algorithm steps on the arm model, link parameters are summarized in Table 4.2, noting that $\alpha_i$ is the twist, $a_i$ is the link length, $d_i$ is the joint offset, and $\theta_i$ is the joint angle in radians [39].

Table 4.2: Human arm model DH link description table

| **Link$_i$** | **$\theta_i$** | **$a_i$** | **$\alpha_i$** | **$d_i$** |
|---|---|---|---|---|
| 1 | $\Theta_1$ | 0 | $-\left(\frac{\pi}{2}\right)$ | 0 |
| 2 | $\Theta_2$ | 0 | $\left(\frac{\pi}{2}\right)$ | 0 |
| 3 | $\Theta_3$ | $L_u$ | $-\left(\frac{\pi}{2}\right)$ | 0 |
| 4 | $\Theta_4$ | 0 | $\left(\frac{\pi}{2}\right)$ | 0 |
| 5 | $\Theta_5$ | 0 | $-\left(\frac{\pi}{2}\right)$ | 0 |
| 6 | $-\left(\frac{\pi}{2}\right)$ | $L_F$ | $\left(\frac{\pi}{2}\right)$ | 0 |

Since the roll, pitch and yaw angles - given by each inertial sensor module - are measured about the fixed NED frame, they had to be mapped to relative joint angles. This is due to the nature of the DH algorithm that uses relative angles between each joint and the previous.

Given that the shoulder remains fixed with the base fixed to the NED frame, mapping of the first three DOF can be done directly as:

$$\Theta_1 = yaw_{s2} - \frac{\pi}{2} \tag{4.11}$$

$$\Theta_2 = -roll_{s2} + \frac{\pi}{2} \tag{4.12}$$

$$\Theta_3 = -pitch_{s2} + \frac{\pi}{2} \tag{4.13}$$

Such that $yaw_{s2}$ , $roll_{s2}$ $and$ $-pitch_{s2}$ stand for the fixed XYZ frame Euler angles obtained sensor module 2 (fixed between the shoulder and the elbow).

On the other hand, to obtain the relation between the Euler angles from module 3 (fixed between the elbow and the wrist), a slightly different approach had to be considered. Given the relation between the two rotation matrices from frames {2} and {3} in equation (4.6), the relative Euler angles can be obtained [39] as:

$$\theta_3^2 = atan2\ (-r_{31}, \sqrt{r_{11}^2 + r_{21}^2}) \tag{4.14}$$

$$\psi_3^2 = atan2\ (\frac{r_{21}}{c\theta_3^2}, \frac{r_{11}}{c\theta_3^2}) \tag{4.15}$$

$$\emptyset_3^2 = atan2\ (\frac{r_{32}}{c\theta_3^2}, \frac{r_{33}}{c\theta_3^2}) \tag{4.16}$$

Such that $\emptyset_3^2$ stands for the roll angle between frames {3} relative to {2}, and so on for the rest of angles.

This can define the joint angles $\Theta_4\ and\ \Theta_5$ by using

$$\Theta_4 = \ \psi_3^2 + \frac{\pi}{2} \tag{4.17}$$

$$\Theta_5 = \ \emptyset_3^2 + \frac{\pi}{2} \tag{4.18}$$

The forward kinematics used to find the three positions of the elbow joint as well as the wrist joint (the far end of the forearm) can be obtained using the corresponding DH homogenous transformation matrices method. Since each degree of freedom is modeled as a link of the model, the transformation matrix for each link has the following form [40]:

$$T_n^{n-1} = Rot_{z_{n-1}}(\theta_n) \cdot Trans_{z_{n-1}}(d_n) \cdot Trans_{x_n}(a_n) \cdot Rot_{x_n}(\alpha_n) \tag{4.19}$$

$$T_n^{n-1} = \begin{bmatrix} c\theta_n & -s\theta_n\, c\alpha_n & s\theta_n\, s\alpha_n & a_n\, c\theta_n \\ s\theta_n & c\theta_n\, c\alpha_n & -c\theta_n\, s\alpha_n & a_n\, s\theta_n \\ 0 & s\alpha_n & c\alpha_n & d_n \\ 0 & 0 & 0 & 1 \end{bmatrix} \tag{4.20}$$

The final orientation and position of the wrist are given by the multiplication of the transformation matrices for each link. This is determined by using:

$$T_0^n = \prod_0^n T_{n-1}^n \tag{4.21}$$

Such that the 4x4 matrix ${}_0^nT$ is the final resulting transformation matrix for the wrist's three-dimensional position.

The general notation of the transformation matrix is given by the position vector d and the 3x3 orientation matrix R as:

$$T_0^n = \begin{bmatrix} R_{11} & R_{12} & R_{13} & d_x \\ R_{21} & R_{22} & R_{23} & d_y \\ R_{31} & R_{32} & R_{33} & d_z \\ 0 & 0 & 0 & 1 \end{bmatrix} \tag{4.22}$$

The DH model for the human arm was implemented using MATLAB's robotics toolbox software, Figure 4.5, as well as CH (C-Interpreter) programming language for testing and validation.

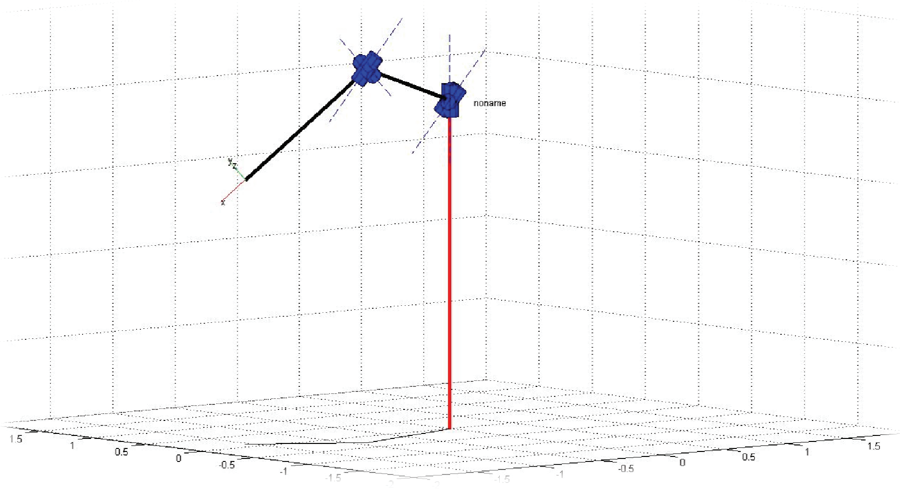

Figure 4.5: Matlab robotics toolbox model

The model's constant input parameters ($\alpha_n$, $a_n$ and $d_n$) were streamed to the algorithm according to the DH parameters in Table 4.2.

## 4.4 Forward Kinematics using Dual Quaternions

As discussed already, quaternions are quadruples of numbers that can be used to express rotation but not translational motion. Eduard Study and William Clifford expanded quaternions to include translational motion by adding a second dual parameter to each element of the quaternion [41], shown as:

$$\hat{q} = (q_0 + q_{00}\varepsilon) + (q_1 + q_{01}\varepsilon)\hat{\imath} + (q_2 + q_{02}\varepsilon)\hat{\jmath} + (q_3 + q_{03}\varepsilon)\hat{k} \tag{4.23}$$

such that the parameter $\boldsymbol{\varepsilon}$ is the dual operator, with $\varepsilon^2 = 0$. Also, the elements $q_{00,}$ $q_{01}$, $q_{02}$ and $q_{03}$ are the dual elements of the quaternion.

A dual quaternion can also be written as a summation of a normal quaternion and a dual one.

$$\hat{q} = q + q_0\varepsilon \tag{4.24}$$

In this section, the dual quaternion notation used is shown as:

$$\hat{q} = (\hat{q}_s, \hat{q}_v) \tag{4.25}$$

such that $\hat{q}_s$ and $\hat{q}_v$ are the scalar and vector components of the dual quaternion having real and dual parts themselves.

Dual numbers can also be used to represent angles between lines in three-dimensional Euclidean space, such that:

$$\hat{\theta} = \theta + a\,\varepsilon \tag{4.26}$$

where $\hat{\theta}$ is the dual angle, $and\ \theta$ is the angle between the orthogonally projected vector $V_1$ and vector $V_{2.}$ Also, the distance L is the common perpendicular distance between the line vectors, as shown in Figure 4.6.

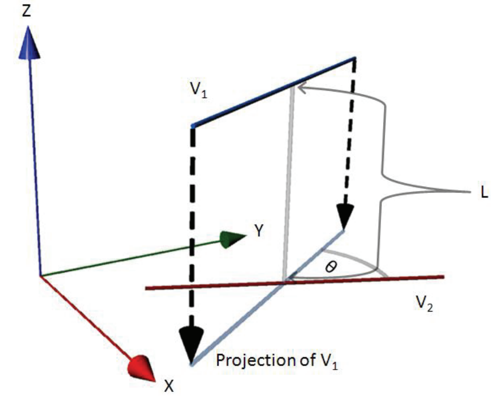

Figure 4.6: Illustration of the dual angle between two vectors

Aspragathos and Dimitros [40] compared homogenous transformations with dual quaternions for robot kinematics. The dual quaternion method makes use of screw theory to describe three-dimensional motion. Screw theory states that any motion trajectory can be simplified by describing it as a rotation on the edge of a screw with a given pitch and angle of rotation and a vector expressing the axis of rotation that the body rotates about [42]. The Plucker coordinates can also express this process.

The application of screw theory through using dual quaternions [43] had been adapted to fit the needs of the human arm model. The dual quaternion algorithm depends on the generated DH table, like its DH method counterpart. However, the dual quaternion has faster calculation speed as well as the immunity to singularities. The modified algorithm procedure is outlined in the following steps [40]:

1. Assignment of the coordinate frames to the upper and forearm links (considering the mounted inertial sensor modules axes) following the Denavit-Hartenberg's notation.

2. Construction of the DH table as stated previously in this Chapter.

3. Assignment of the unit vector $\hat{s}_{i,i+1}$ along the $\hat{Z}_i$ axis assigned using the previous step (i.e. the joints' axes of rotation). The initial condition of $\hat{s}_i$ is at the base frame, where i=0, resulting in:

$$\hat{s}_1 = \hat{k}$$

4. Assignment of the unit vector $\hat{a}_{i,i+1}$ along the $\hat{X}_i$ axis by the previous step – that is along the common perpendicular between joints' axes if they are parallel or perpendicular to the plane they make if they intersect. The initial condition of $\hat{s}_i$ is at the base frame where i=0, resulting in:

$$\hat{a}_{0,1} = \hat{\imath}$$

Modifying the DH table to include the dual angles $\hat{\theta}$ and $\hat{\alpha}$ yields:

$$\hat{\theta} = \theta + a\,\varepsilon$$

$$\hat{\alpha} = \alpha + d\,\varepsilon$$

This results in adding two columns to the DH table as shown in Table 4.3. $L_u$ and $L_F$ are the lengths of the upper and forearm, respectively.

Table 4.3: Dual angles extracted from DH table

| **Link$_i$** | **$\theta_i$** | **$a_i$** | **$\alpha_i$** | **$d_i$** | $\hat{\theta}$ | $\hat{\alpha}$ |
|---|---|---|---|---|---|---|
| 1 | $\Theta_1$ | 0 | $-\left(\frac{\pi}{2}\right)$ | 0 | $\Theta_1$ | $-\left(\frac{\pi}{2}\right)$ |
| 2 | $\Theta_2$ | 0 | $\left(\frac{\pi}{2}\right)$ | 0 | $\Theta_2$ | $\left(\frac{\pi}{2}\right)$ |
| 3 | $\Theta_3$ | $L_u$ | $-\left(\frac{\pi}{2}\right)$ | 0 | $\Theta_3+\epsilon\, L_u$ | $-\left(\frac{\pi}{2}\right)$ |
| 4 | $\Theta_4$ | 0 | $\left(\frac{\pi}{2}\right)$ | 0 | $\Theta_4$ | $\left(\frac{\pi}{2}\right)$ |
| 5 | $\Theta_5$ | 0 | $-\left(\frac{\pi}{2}\right)$ | 0 | $\Theta_5$ | $-\left(\frac{\pi}{2}\right)$ |
| 6 | $-\left(\frac{\pi}{2}\right)$ | $L_F$ | $\left(\frac{\pi}{2}\right)$ | 0 | $-\left(\frac{\pi}{2}\right)+\epsilon\, L_F$ | $\left(\frac{\pi}{2}\right)$ |

5. The relation between the vectors $\hat{a}_{i,\ i+1}$ and $\hat{a}_{i-1,\ i}$ is defined by the dual quaternion transformation operator Q, where:

$$\hat{a}_{i,\ i+1} = \hat{Q}_i\, \hat{a}_{i-1,i} \tag{4.27}$$

such than: $$\hat{Q}_i = cos\left(\hat{\theta}_i\right) + \hat{s}_i\, sin\,(\hat{\theta}_i) \tag{4.28}$$

Knowing that the cosine and sine functions for a dual angle obey the following rules:

$$cos(\hat{\theta}_i) = cos(\theta_i + \varepsilon a_i) = cos(\theta_i) - \varepsilon \; a_i \; sin(\theta_i) \qquad (4.29)$$

$$sin(\hat{\theta}_i) = sin(\theta_i + \varepsilon a_i) = sin(\theta_i) - \varepsilon \; a_i \; cos(\theta_i) \qquad (4.30)$$

6. The relation between the vectors $\hat{s}_{i+1}$ and $\hat{s}_i$ is also defined by the Dual quaternion transformation operator Q, where:

$$\hat{s}_{\,i+1} = \hat{Q}_{i\,,i+1}\, \hat{s}_{\,i} \qquad (4.31)$$

such that $\hat{Q}_{i\,,i+1} = cos(\hat{\alpha}_{i.i+1}) + \; \hat{a}_{i\,,i+1}\, sin\; (\hat{\alpha}_{i.i+1})$

and such that $\hat{\alpha}_{i.i+1}$ is the twist angle between the i$^{th}$ and the i+1 joint rotation axis.
By analogy to equations (4.29) and (4.30), the sine and cosine functions for the dual angle $\hat{\alpha}_{i\,,i+1}$ are:

$$cos(\hat{\alpha}_{i\,,i+1}) = cos(\hat{\alpha}_{i\,,i+1} + \varepsilon d) = cos(\alpha) - \varepsilon \; d \; sin(\alpha) \qquad (4.32)$$

$$sin(\hat{\alpha}_{i,i+1}) = sin(\alpha_{i,i+1} + \varepsilon d) = sin(\alpha) - \varepsilon \; d \; cos(\alpha) \qquad (4.33)$$

7. Calculation of the position vector for forearm’s tip coordinate frame origin (also called end- effector in robotics) is done by:

$$P_n = \sum_{i=1}^{n} (d_i \; s_i + L_i \; a_{i,i+1}) \qquad (4.34)$$

8. Finally, the orientation of the same coordinate frame is calculated by:

$$n_n = a_{n,n+1} \tag{4.35}$$

$$a = s_{n+1} \tag{4.36}$$

$$o = s_{n+1} \times a_{n,n+1} \tag{4.37}$$

Simulation results for this algorithm were produced using the CH language [44] because of its support of the dual numbers data type and its algebra. A 5-DOF model was designed as stated in Table 4.3, and to compare results, joint angles used were the same as the ones used for the DH forward kinematics. Results showed that the DQ algorithm gives an output identical to that of the DH method, with the advantage of smaller processing times for higher degrees of freedoms as stated in [40]. The comparison between the dual quaternion method and the DH method is summarized in Table 4.4.

Table 4.4: Comparison between Dual Quaternion and DH algorithms

| **Points of Comparison** | **Homogenous Transformation** | **Dual Quaternions** |
|---|---|---|
| • **Visualization of theory of operation** | Easy to visualize | Difficult to visualize |
| • **Quantity of Calculation** | More | Less |
| • **Single Rotation operation** | Complex | Simple |
| • **Single Translation** | Simple | Complex |
| • **Combined rotation and translation.** | Complex | Simple |
| • **Gimbal Lock Problem** | Might exist and cause singularities | Doesn't Exist |

A 3D position-based comparative study was made of the performances of the DH algorithm and the Dual Quaternions one by simulating their input angles as shown in Figure 4.7. The output 3D trajectories from both algorithms were the same, as shown in Figure 4.8.

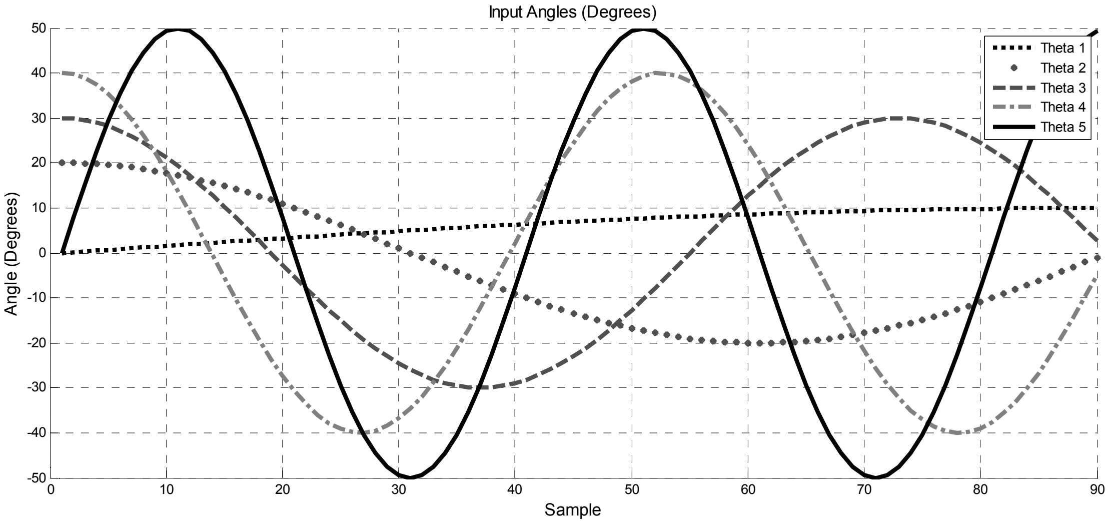

Figure 4.7: Input angles for comparing DH and DQ algorithms' performance

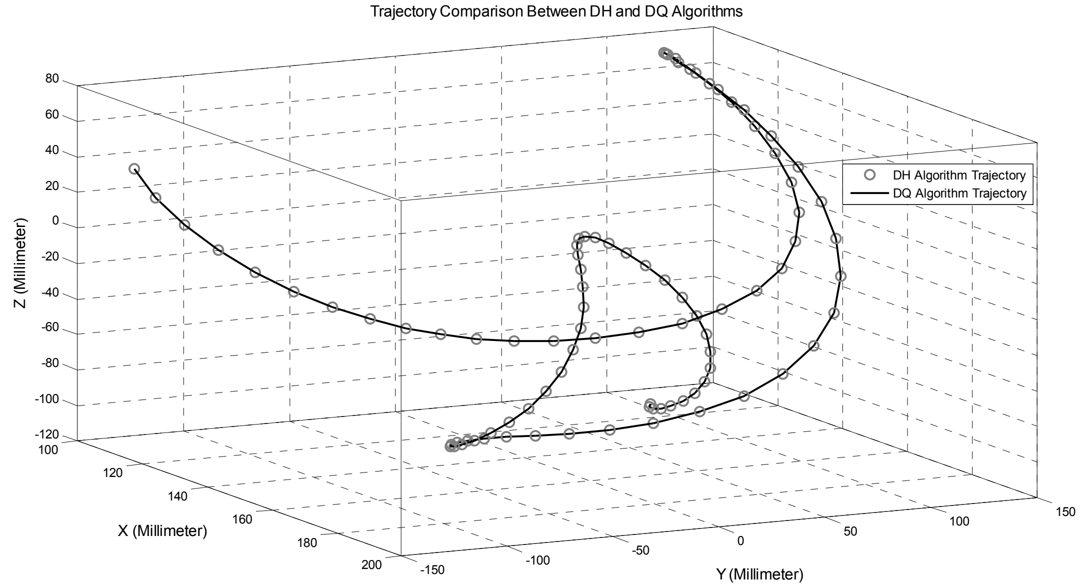

Figure 4.8: Simulation 3D position trajectory

Furthermore, the computing speed of the dual quaternion method showed faster results than the DH algorithm for higher degrees of freedom systems, as shown in Figure 4.9 and Figure 4.10.

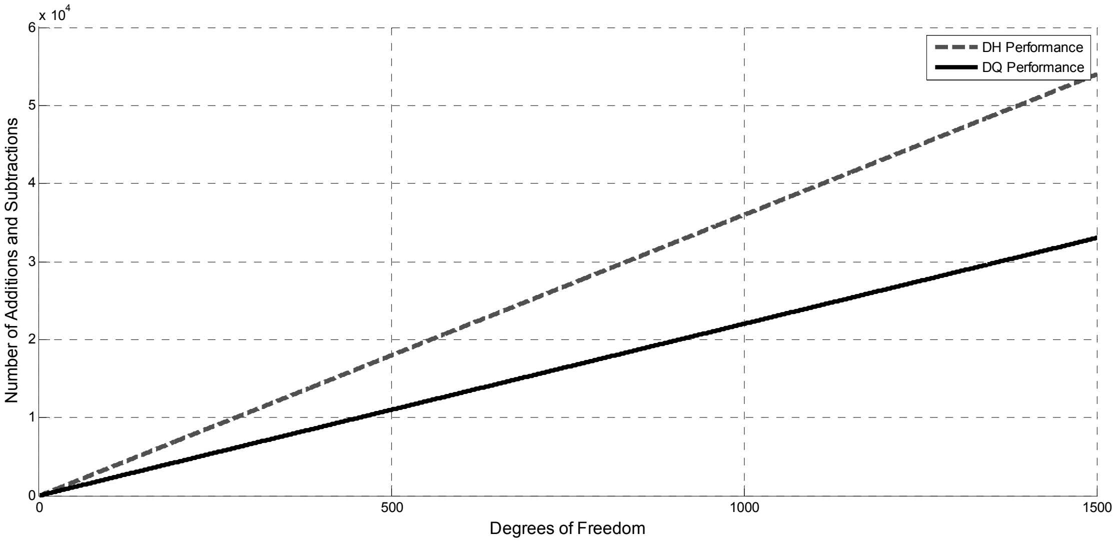

Figure 4.9: Add/Subtract computational cost for DH vs. DQ algorithms

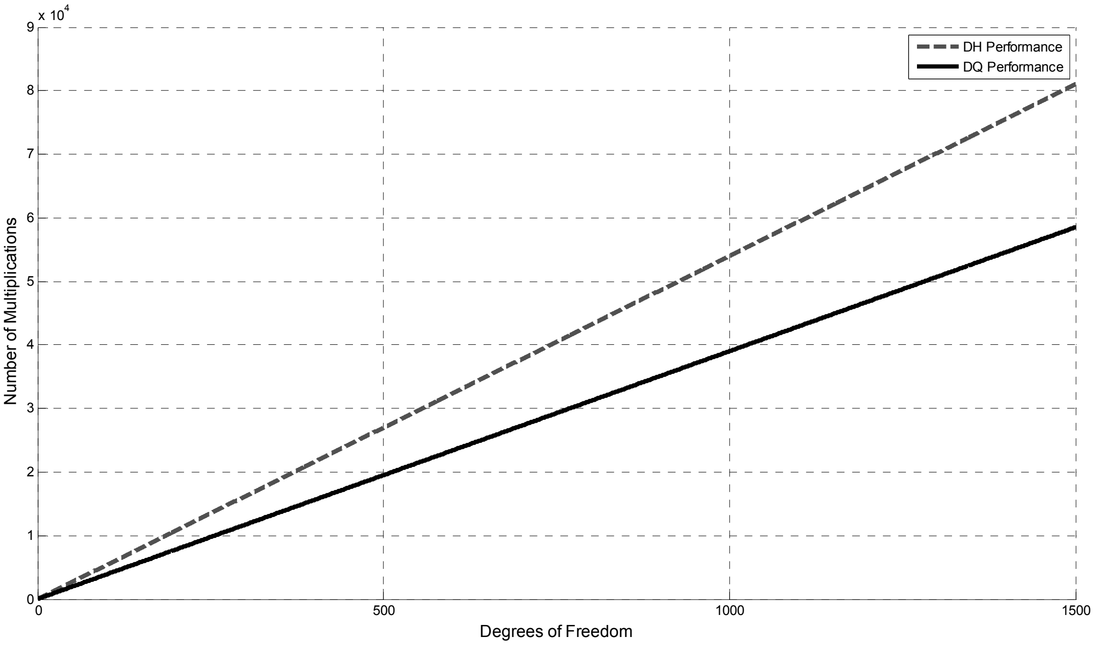

Figure 4.10: Multiplication computational cost for DH vs. DQ algorithms

In practice, the angles were fed to the model using the estimated values acquired from the Extended Kalman Filter after being measured using the inertial measurement units mounted on the arm.

## 4.5 Experimental Results

Proof of concept experiments have been designed for validating the local positioning algorithms discussed in this Chapter. The experimental setup was done using the artificial arm model and the motion tracking system mentioned in Chapter 5 section 4.

At first, a 3D motion trajectory was calculated using raw orientation angles data from the sensors by applying directly the forward kinematics techniques. This raw position data were considered as the measurements. After that, the angles were fed to the EKF algorithms mentioned in Chapter 3 to obtain better position estimates after applying forward kinematics. Local positioning results for a pitch motion trajectory are shown for each axis separately in Figure 4.11through Figure 4.13.

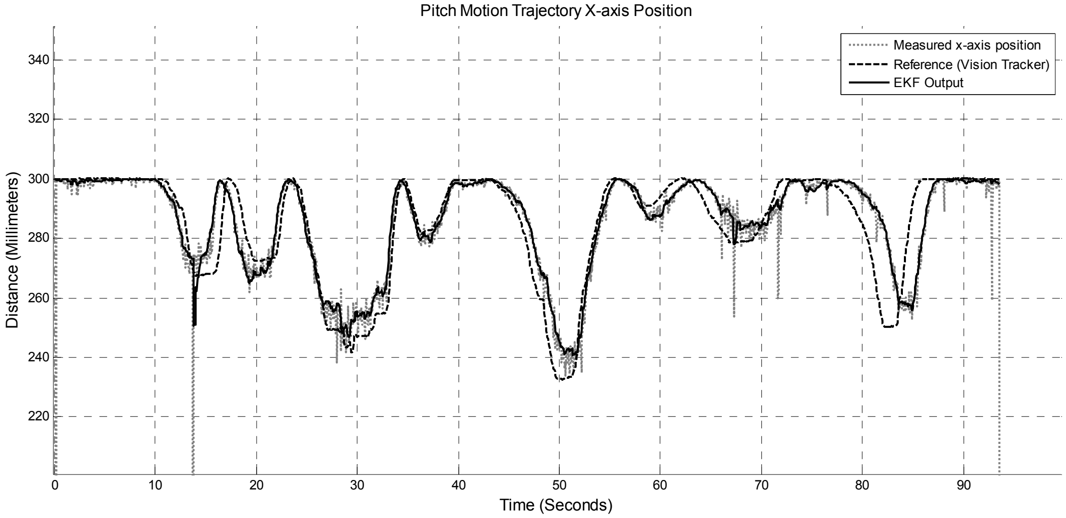

Figure 4.11: EKF performance on elbow-joint positioning (x-axis)

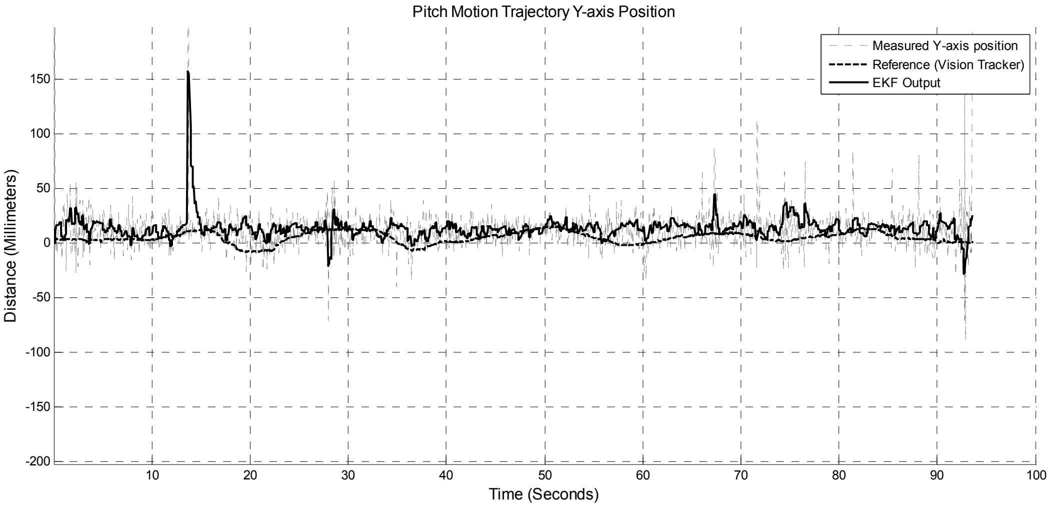

Figure 4.12: EKF performance on elbow-joint positioning (y-axis)

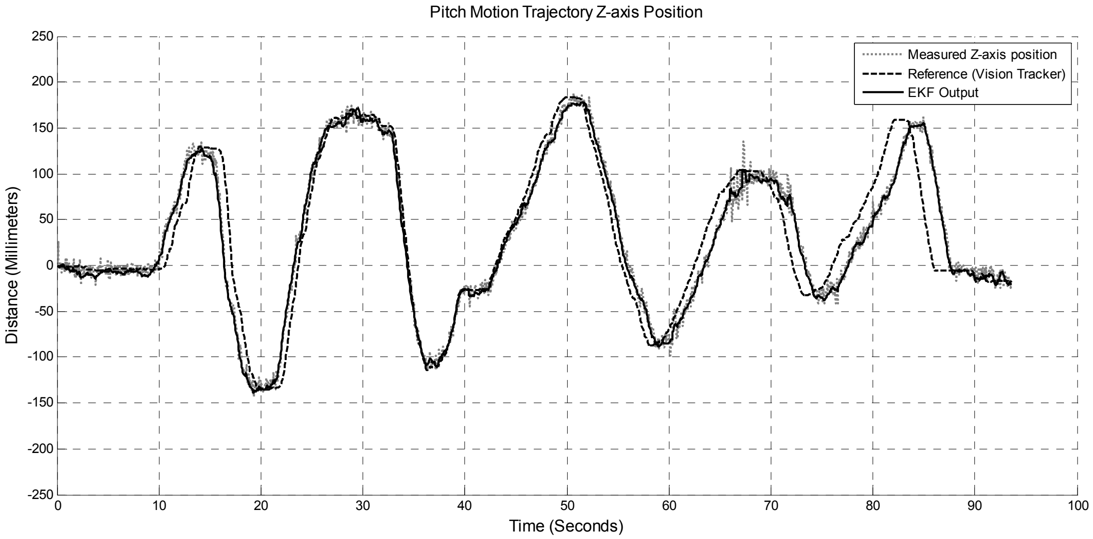

Figure 4.13: EKF performance on elbow-joint positioning (z-axis)

Combining position data from the previous figures shows the 3D motion trajectory shown in Figure 4.14.

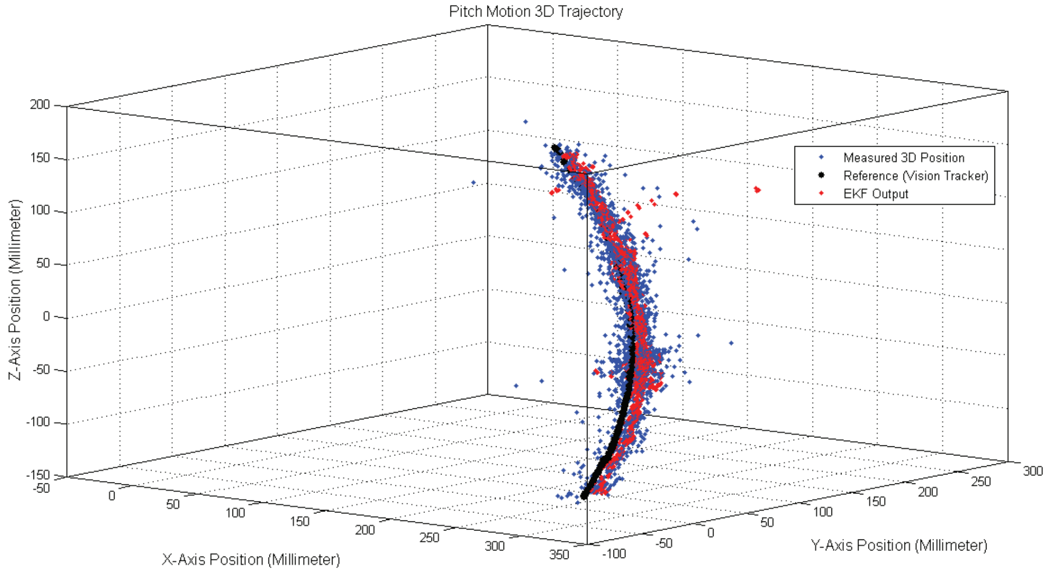

Figure 4.14: EKF performance on a 3D pitch motion trajectory

Moreover, another proof of concept yaw motion trajectory was also captured and processed like the pitch motion one mentioned earlier. The output 3D motion trajectory proved successful comparing the reference trajectory to the estimated one as shown in Figure 4.15.

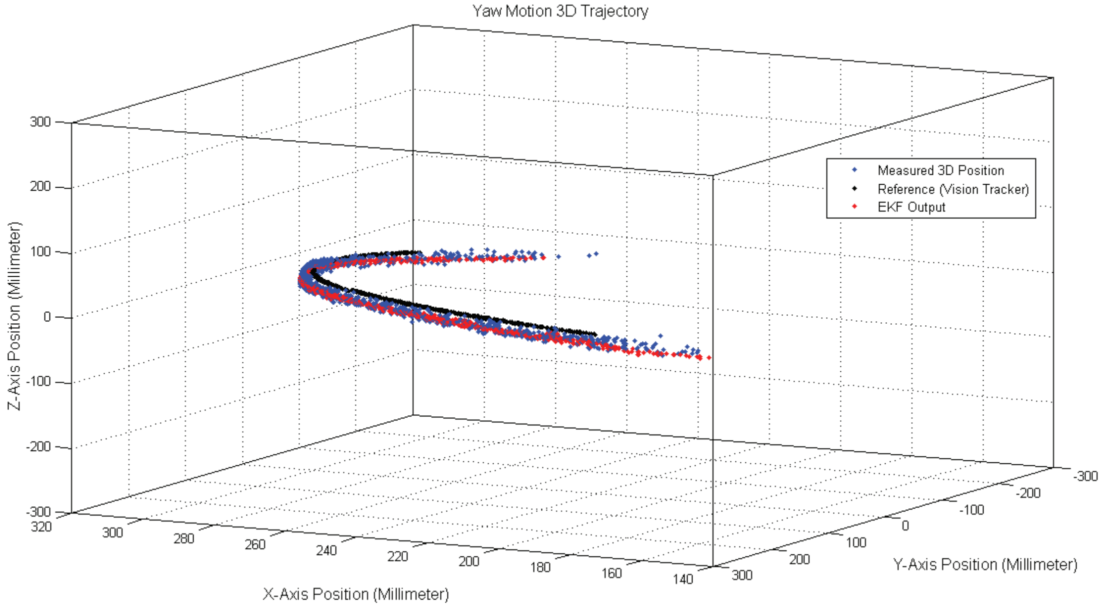

Figure 4.15: EKF performance on a 3D yaw motion trajectory

Results show the performance improvement before and after applying the EKF estimator. The position error was minimized in almost all three axes to about 5cm in each one. Nevertheless, these error data are preliminary due to the fact that the sensors were not perfectly synchronized, which led to time shifting and therefore maximized subtraction errors. However, these promising results showed stability over the complete experiment time. The preliminary error charts for all three axes are shown in Error! Reference source not found.Figure 4.16 through Figure 4.18**.**

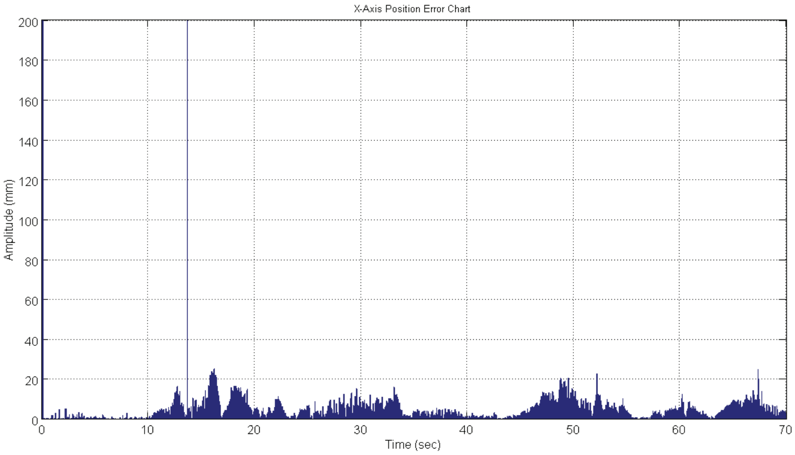

Figure 4.16: Error chart for local positioning (x-axis)

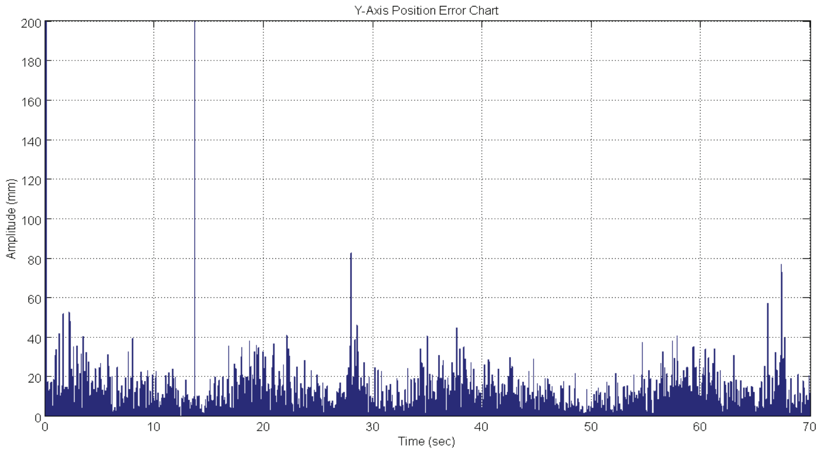

Figure 4.17: Error chart for local positioning (y-axis)

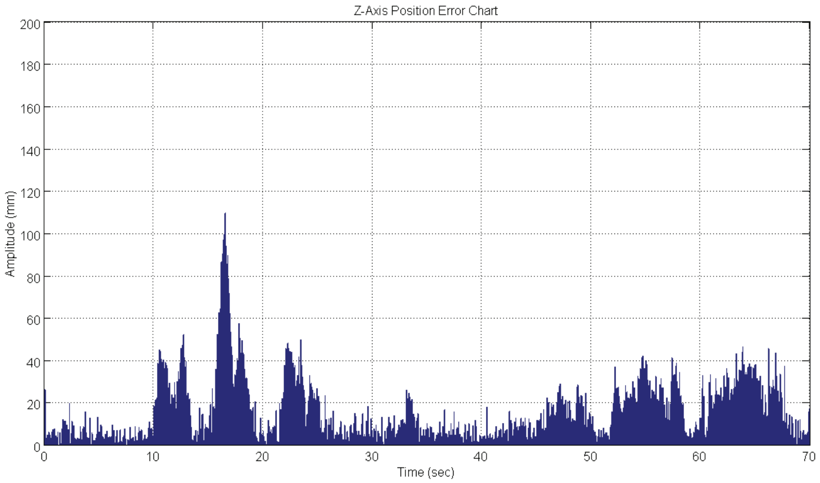

Figure 4.18: Error chart for local positioning (z-axis)

# Chapter 5: EXPERIMENTAL STUDIES

The experimental design plays a significant role in the application of the proposed monitoring system. In this Chapter, the system level designs as well as the implementation and manufacturing phases are discussed. In general, the system is expected to provide proof of concept as to measure and estimate human arm joint angles and send the data wirelessly to a host PC. The host PC is responsible for performing the more complicated mathematics on the sensor's data being fed from the wireless sensor modules. Finally, the testing and validation of the integrated system was done using Matlab, CH IDE and LabVIEW programming languages.

## 5.1 System Design Criteria

The primary system design goal for this research is to integrate the two groups of sensors (also called module-I and module-II) with an embedded microcontroller and a wireless communication transceiver. To do so, some restrictions had to be specified to outline the design methodology. The defined system criteria were defined as:

- Defining the best fit from cost benefit analysis of the system components.
- Low power consumption due to the need for portability.
- Sufficient sampling time and processing speed for later system optimization for real time application.
- Wireless connectivity that has networking capabilities for system expansion to model the whole human body in future research stages.

- Small set up time of the system on the human arm to allow friendly use by multiple patients.

The general system design is composed of two main components: the simple body area network (BAN) containing the sensors and the host personal computer (Host PC), as shown in Figure 5.1.

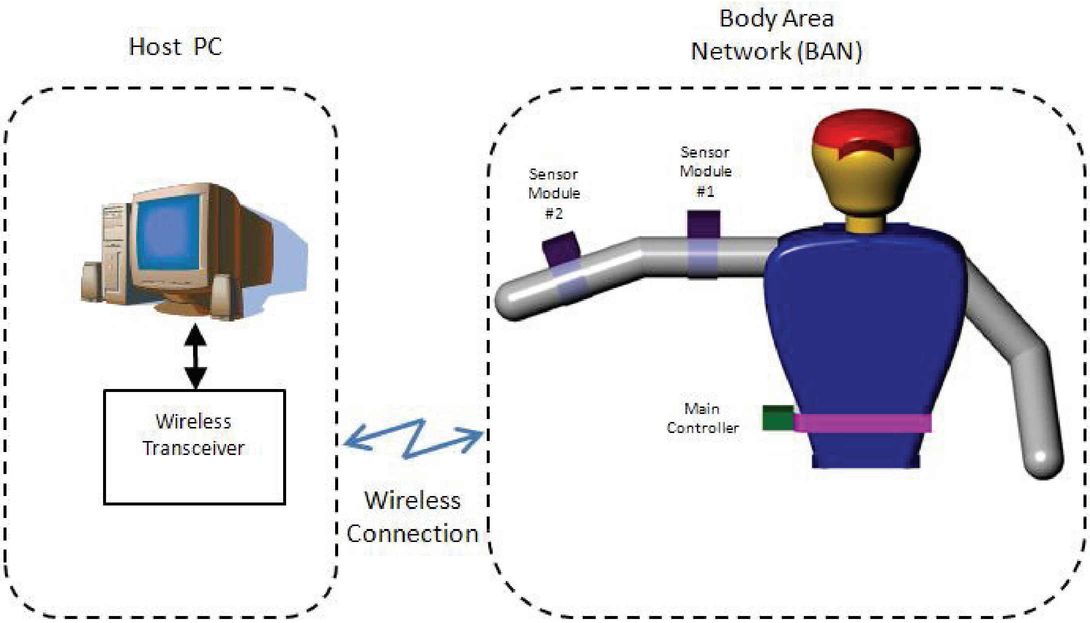

Figure 5.1: Total hardware system structural design

### 5.1.1 Body Area Network (BAN)

The body area network is a simple network between multiple sensors following the star networking topology. The main processor (i.e. microcontroller) acts as a master to all slave sensors. The master controller initializes the sensor modules according to the sampling, timing and power consumption needs at power-up. Moreover, the master is also responsible for sending the acquired sensor data to the host PC via a wireless communication transceiver (Zigbee). The network hierarchy in Figure 5.2 shows the star topological nature of the designed BAN between the master controller and the sensor modules.

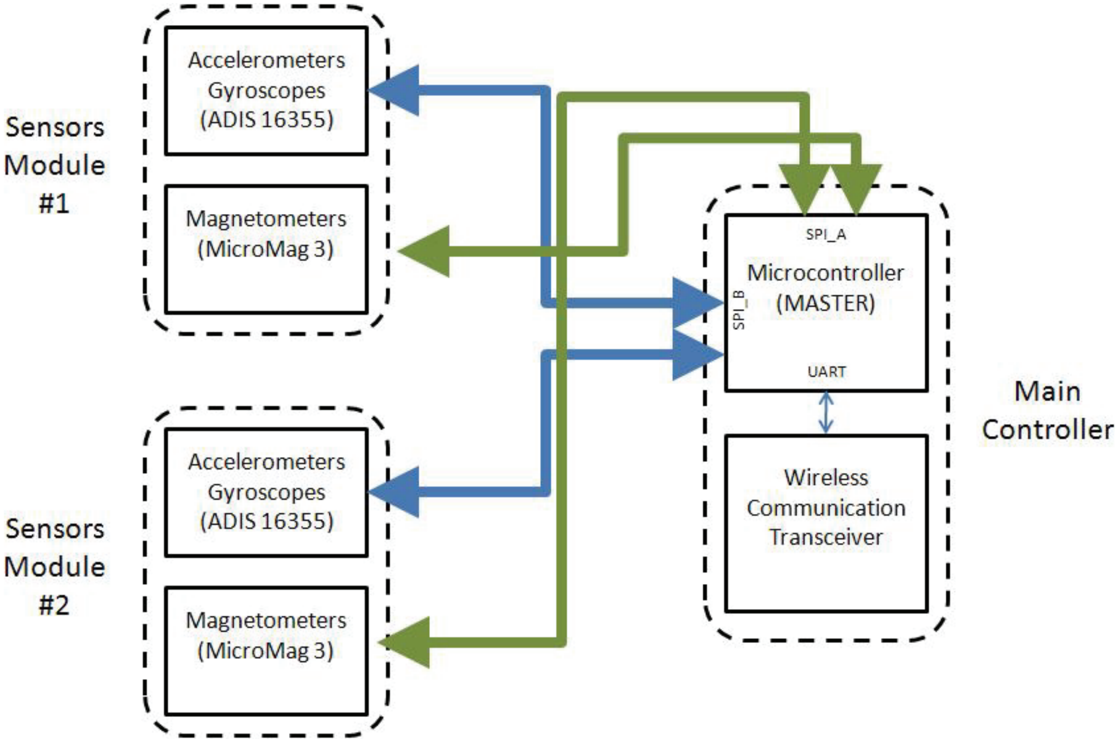
Sensors Module #1
Accelerometers Gyroscopes (ADIS 16355)
Magnetometers (MicroMag 3)
Sensors Module #2
Accelerometers Gyroscopes (ADIS 16355)
Magnetometers (MicroMag 3)
SPI_A
SPI_B
Microcontroller (MASTER)
UART
Wireless Communication Transceiver
Main Controller

Figure 5.2: Sensor communication network following the Star topology

#### 5.1.1.1 Hardware Designs

The hardware design procedure has undergone several development phases to fulfill the needs of the project. As shown previously in Figure 5.2, the main microcontroller communicates directly (wired) to the sensor modules. A market study of the available inertial sensors technologies showed that digitally interfaced sensors are best for this application, because these types of sensor include the entire necessary signal conditioning circuitry built on-chip, dramatically reducing overall circuitry physical size. On the other hand, the Texas Instruments MSP430F5438 microcontroller has been chosen for its low power consumption (≈9 μ. Watts in Low-Power-Mode); furthermore, it gives some flexibility in the hardware configuration, as will be discussed in section 5.2.2.

#### 5.1.1.2 Sensor Module Design

Each of the two sensor modules mounted on the arm contains a complete set of triplets of angular rate gyroscopes, accelerometers and magnetometers. The evaluation of each of the Analog Devices ADIS16355 (Gyros and Accelerometers) as well as the PNI MicroMag3 (Magnetometers) was done through their evaluation boards. Later, the sensor embedded interfacing was held separately for each sensor for efficient software and hardware debugging purposes. The ADIS16355 connection diagram for embedded interfacing depends on the use of its many features. However, this sensor has been tested using the Atmel AVR 8-bit MCU as well as the Texas Instruments MSP430 16-bit MCU following the Serial Peripheral Interface (SPI) communication protocol. The ADIS16355 sensor communicates with the microcontroller through its on-chip SPI module. Similarly, the Magnetometer (PNI Micromag3) uses the same protocol to interface with the embedded controller noting the different protocol settings, as will be discussed in the embedded software section.

However, the communication with the AVR microcontroller through the SPI protocol was easier than with the msp430 because the ADIS16355 communication voltage levels were the same (5V) as those of the AVR .  On the other hand, the msp430 uses lower voltage levels for minimizing the power consumption (3.3V), a fact that introduced the problem of the voltage level translation for the SPI connections. To convert the voltage levels from one level to another, a fast switching circuit has to be used because of the fast switching speeds on the SPI Bus – up to 2 MHz on the SPI clock. The high-level translation was accomplished using the Maxim MAX3390, as shown in the block diagram in Figure 5.3. The sensor connection diagram in Figure 5.3 shows the connection dataflow used for interfacing both sensor groups to form one complete module.

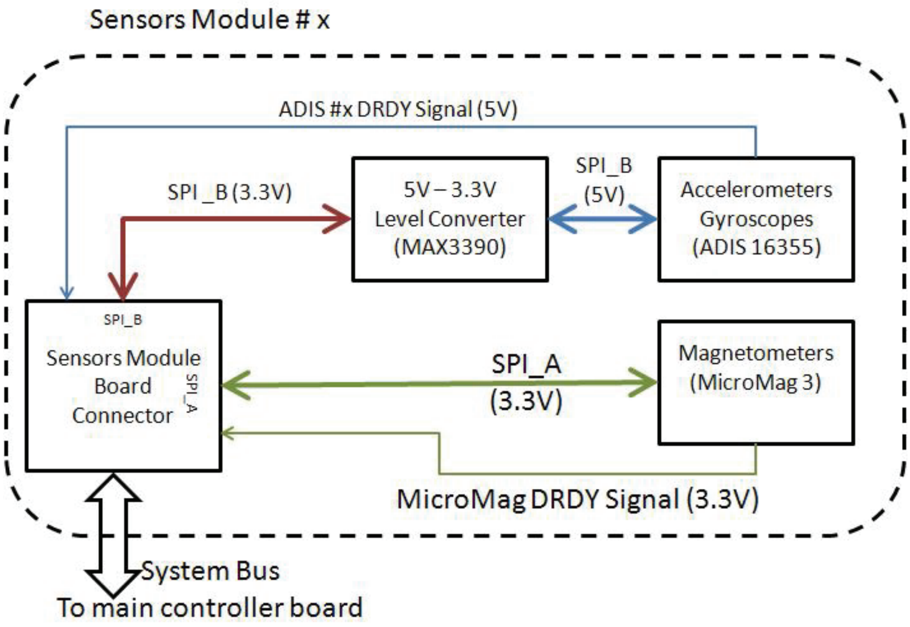

Figure 5.3: Sensor module internal circuitry structure

Due to the limitation of the input/output terminals on the level translator chip, the data ready line for the ADIS sensor had to be sent to the controller module, maintaining its high voltage levels (5V Logic). As a solution, another level translator was mounted on the main controller circuitry to convert all the data-ready signals streaming in from all the ADIS16355 sensors. The controller and communication circuits will be discussed in more detail in the next section. The complete printed sensor circuit board 3D design was assembled using Solid Works CAD software as shown in Figure 5.4.

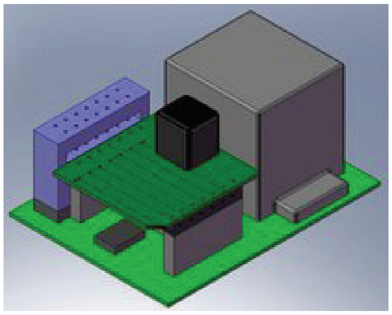

Figure 5.4: Sensor module PCB CAD model

The corresponding printed circuit board of the sensor model is shown in Figure 5.5.

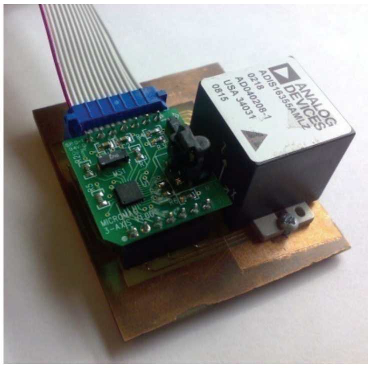

Figure 5.5: PCB implementation of an integrated sensor module

### 5.1.1.3 Main Controller and Communications Module

Because of its high bit rate and full duplicity, the Serial peripheral interface (SPI) communication protocol was used to communicate between sensors and the main microcontroller. Data was tested using National Instrument's LabVIEW running on a Microsoft Windows XP platform. Although preliminary results proved successful, the decision was made to change the controller architecture as well as the speed and power consumption. Figure 5.6 shows the block diagram of connections used on the main controller board. The high voltage level (5V) data ready lines extending from the ADIS16355 modules to the controller were reduced using the voltage level translator, also shown in Figure 5.6.

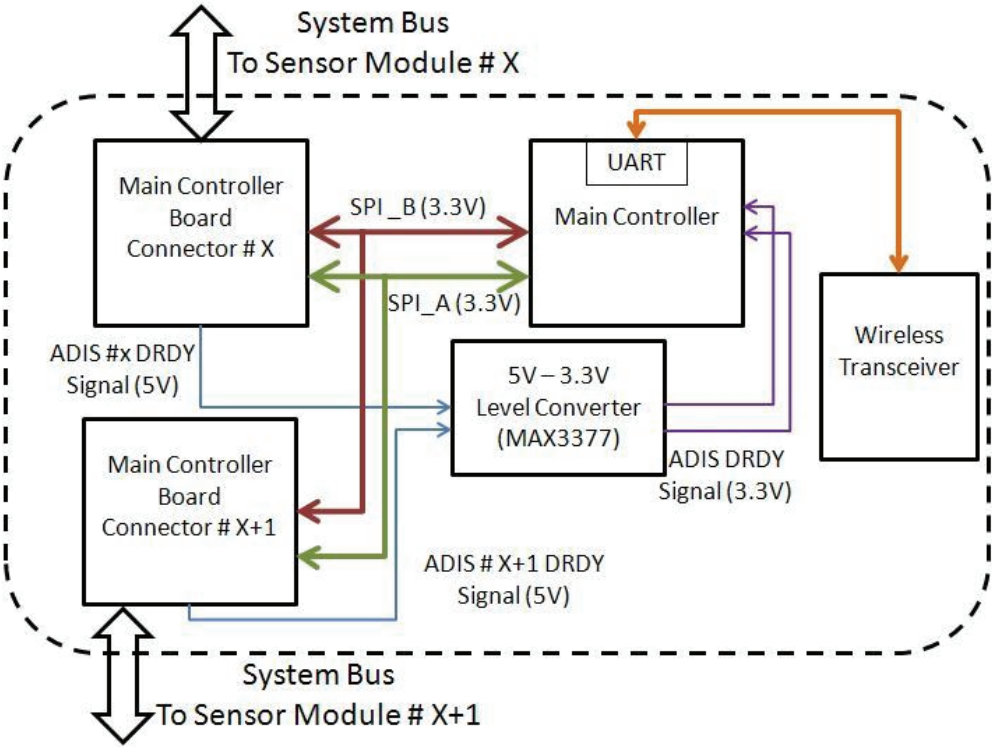

Figure 5.6: Main controller modular circuit structure

The microcontroller was programmed to initialize the sensors as well as perform the sensor calibration and filtering prior to transmitting to the host PC. First, transmitting data wirelessly to the host PC was tested using a commercial grade off-the-shelf serial over Bluetooth connection (BlueSmirf Gold from Sparkfun Electronics). However, this communication method proved inconsistent because it lacked compatibility to be further extended to cover the whole body as future work using wireless networking. Finally, the Zigbee protocol was used to manage the wireless data communication between the BAN and the host PC. This arrangement improved overall signal performance and filtered out the discontinuities appearing via the Bluetooth module because of buffering problems.

#### 5.1.1.4 Embedded Software Implementation

The software development for this project was split into two main categories, embedded software and PC-based software, according to the platform type. The embedded software was developed using IAR EW430 embedded workbench C compiler for the Texas instruments microcontroller unit. The host PC-related software is discussed in section 5.1.2.

##### a. Sensors Initialization

Sensor initialization takes place at the beginning of each acquisition session at the embedded level on the microcontroller. The initialization sequence sets the important parameters for each sensor, such as the sampling rate, data ready interrupts, and dynamic range. The calibration function is controlled by the host PC at this phase of the research. Calibration is initiated by the user such that the arm should be held in a horizontal position for some given time. Then, a graphical indicator informs the user of the end of the calibration function. During that period, sensor data are averaged and considered as static biases in the gyroscopes and accelerometers.

##### b. Communication

As stated earlier, communications on the controller module level uses standard SPI protocol. The main concerns faced during the embedded software development include the fact that the controller SPI packet was restricted to only 8-bits at a time, whereas sensors used 16-bit packets. A common solution to this problem, which was tested and verified, is to send two consecutive 8-bit packets with the chip select pin held low as shown in Figure 5.7.

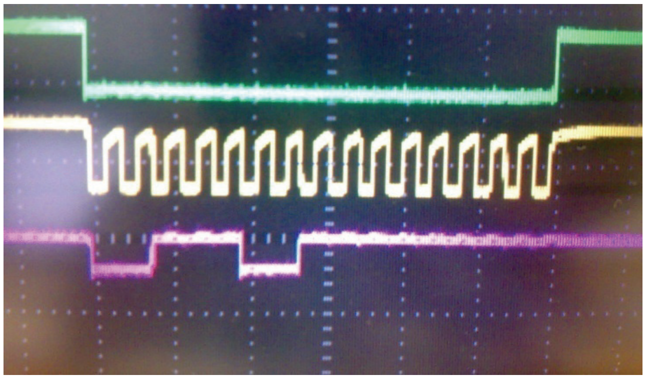

Figure 5.7: 16-Bit SPI word using 2x8-bit sequences

In addition to the communication with the embedded sensors, the main controller handles the wireless communication to the host PC using Zigbee transceivers manufactured by MaxStream, shown in Figure 5.8. This simple communication system proved successful for a distance range of up to 30 m indoors. It can be further extended to larger ranges using Xbee-Pro modules that support up to 90 m indoor coverage.

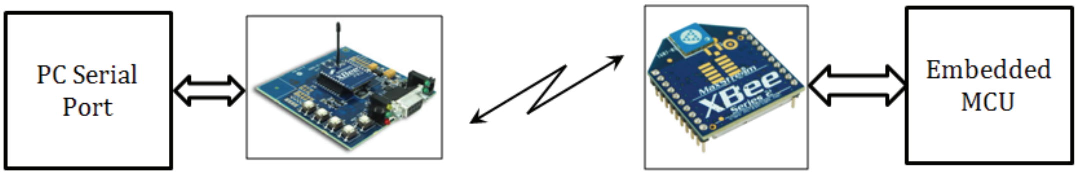

Figure 5.8: Wireless communication to the host PC using Zigbee™

### 5.1.2 Host PC System Design

The host PC system is composed of another transceiver that communicates wireless with the BAN's main controller. Furthermore, the data is fed to the designed PC software via a Serial (RS232) link for further signal processing. The software program on the PC analyzes the sensor data and estimates the orientation angles and the position of the points of interest (i.e. elbow or wrist with respect to the shoulder's NED frame).

#### 5.1.2.1 Data Acquisition

As soon as the data is correctly acquired from the sensor module, it is organized in the form of packets by the MCU for sending to the PC. Next, the sensor data is acquired from the serial port of the PC using RS232 IEEE standard. Then signal processing takes place, in which raw Euler angles are calculated using LabVIEW graphical programming language. Moreover, the position of the points of interest is calculated through a cross software script that connects the LabVIEW program to Matlab to apply the forward kinematics methods (Homogenous Transformation). The software program has been designed so that the user has the option to choose whether or not data logging of all raw calculated values should occur. The raw orientation and position output results are then displayed on a graphical user interface (GUI), as shown in Figure 5.9.

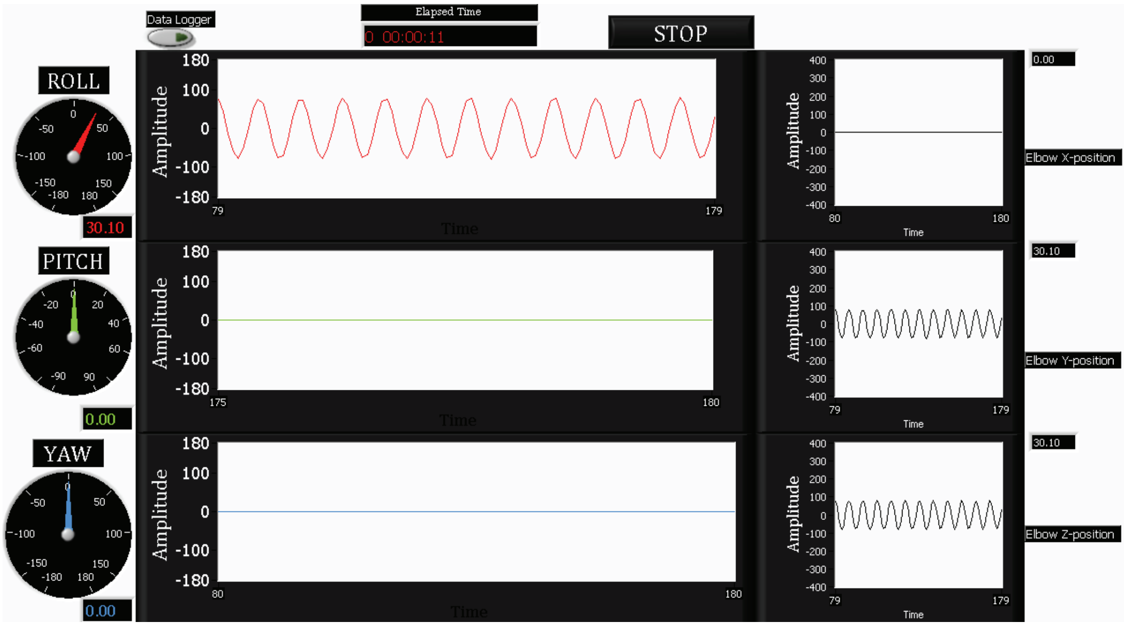

Figure 5.9: LabVIEW implemented Graphical User Interface (GUI)

#### 5.1.2.2 Signal Processing

The two EKF. algorithms elaborated upon in Chapter 3 are implemented in Matlab. The programs load the input from the logged data acquisition sessions using the LabVIEW environment mentioned in the previous section. The output estimated angles are saved in a comma-delimited log file for further processing.

The forward kinematics was done by Soft Integration using the CH IDE linear programming environment. This specific environment has been chosen for its well-established libraries supporting both Denavit Hartenberg's methods and dual number data types. The original programming environment was designed by mechanical and aeronautical engineer and Professor H. Cheng [44].

## 5.2 Sensor Calibration

Calibration can be defined as the process of comparing the data of the unit under test (UUT) to a reference system to help minimize the error of the measuring device. This section explains the calibration of the inertial sensors and the setups involved.

In static conditions, the complete system is fixed in a predefined orientation. Then, sensor data are acquired and logged by the embedded system and the host PC for further studies. Moreover, joint angles and the 3D position of selected points on the arm are compared with data of the corresponding reference system.

The experiment procedure begins by fixing the sensor module in an equilibrium state to log raw inertial sensor data, as shown in Figure 5.10. These data were used to calculate static biases used in Chapter 2 as well as the construction of the covariance matrices discussed in implementing the EKF. in Chapter 3. During data acquisition in this orientation, angular rate measurements are zero in the ideal case. Accelerometers on the other hand show zero acceleration in the x and y axes, and 1 in the z axis because of earth's gravity vector.

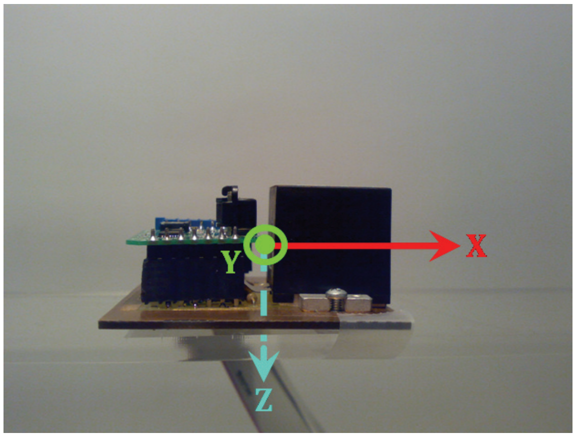

Figure 5.10: Sensor Module in Equilibrium state

After the calibration step is complete, a simple mechanism was needed to measure decoupled orientation angles. The main design consideration was to implement the mechanism in such a way that each angle can be set irrelevant from the other angles. A five degrees-of-freedom arm CAD model was designed according to the specifications mentioned above, as shown in Figure 5.11. The offset between rotation axes of the joints was not taken into consideration during orientation validations. However, these offsets generated some errors during position validation of the biomechanical model in Chapter-4. The offsets were then manually accounted for because in the real mechanism (i.e. human arm) the joints axes are considered coincide.

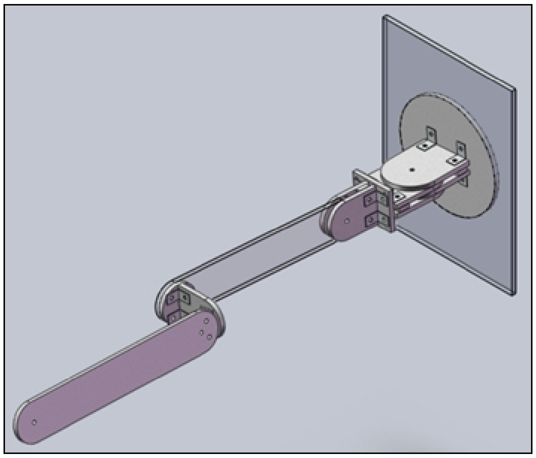

Figure 5.11: Five DOF arm CAD model

The CAD design of the arm model was made in the department's workshop using a Laser cutting machine. Plexiglas material was chosen as the main building material so as to avoid using iron-core parts that would affect magnetic field measurements during data acquisition. The final model is shown in Figure 5.12.

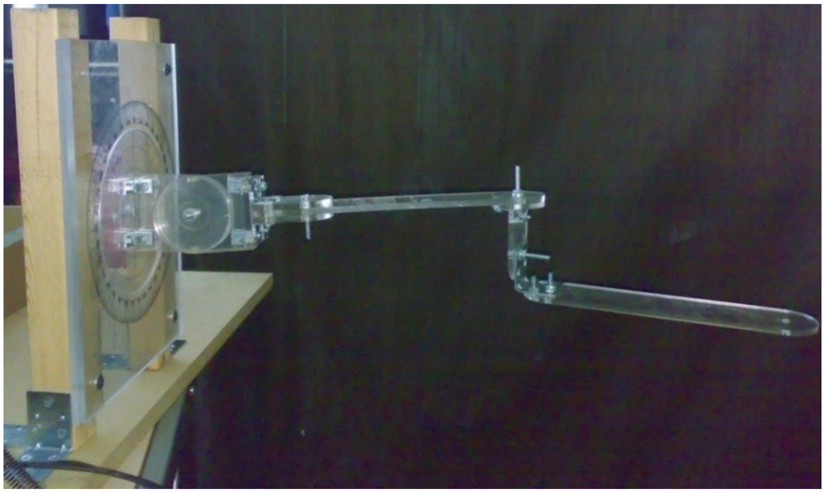

Figure 5.12: Implemented arm model used in experimental tests

## 5.3 Orientation Validation Test Setup

For static orientation calibration, the sensor module was placed on the link joining the shoulder's spherical joint to the elbow joint, because the spherical joint can rotate in all three degrees of freedom concerning orientation – roll, pitch and yaw. In order to insure that the link is fixed at the required orientation, the reference Microstrain's GX2 AHRS shown in Figure 5.13 was first mounted in the correct position, and the attached screws were tightened to fix the model in place.

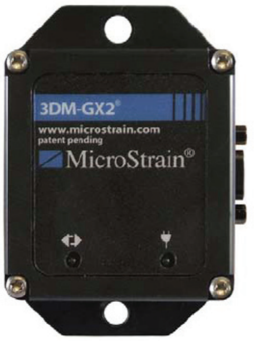

Figure 5.13: Microstrain GX-2 AHRS system

Different orientation angles for each degree of freedom are shown in Figure 5.14 through Figure 5.16.

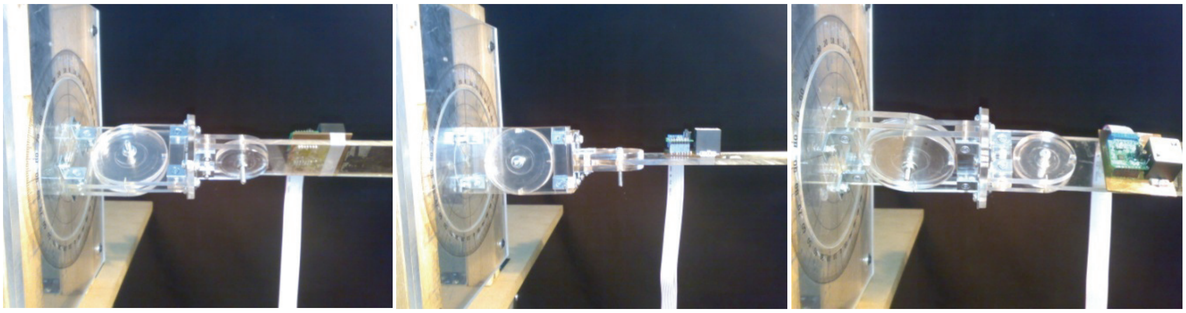

Roll angle of $-45^0$ Roll angle of $0^0$ Roll angle of $45^0$

Figure 5.14: Roll testing in different orientations

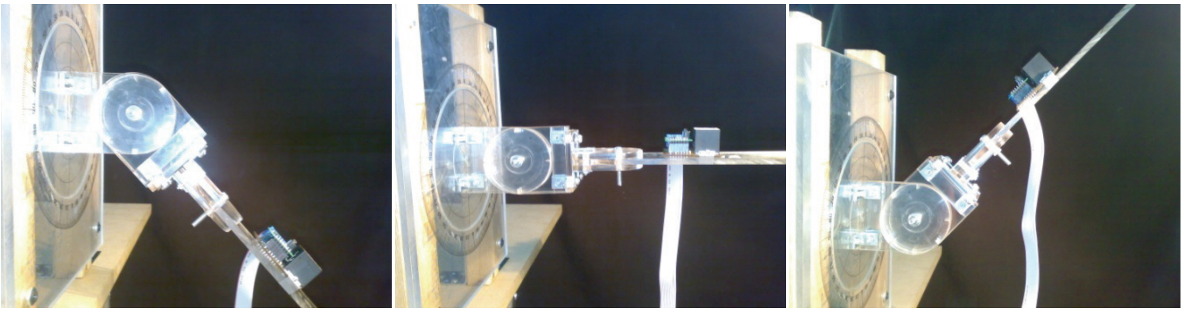

Pitch angle of $-45^0$ Pitch angle of $0^0$ Pitch angle of $45^0$

Figure 5.15: Pitch testing in different orientations

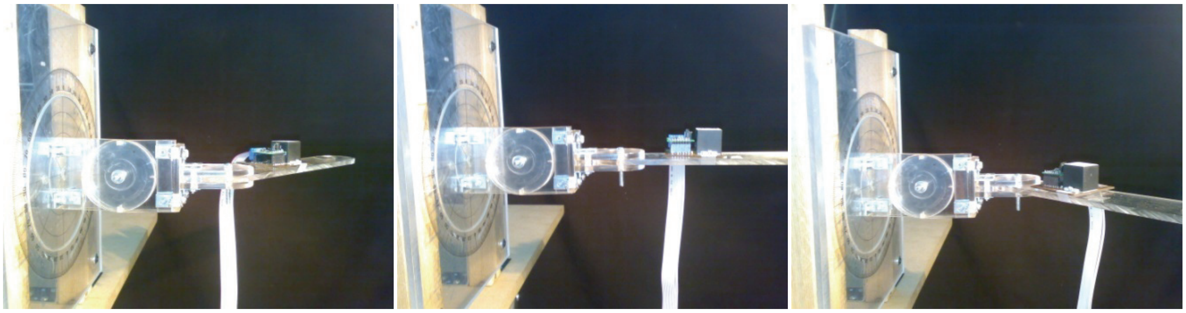

Yaw angle of $-45^0$ Yaw angle of $0^0$ Yaw angle of $45^0$

Figure 5.16: Yaw testing in different orientations

During testing of the Yaw angle, it was observed that the measurements were greatly affected by surrounding materials containing iron or iron alloys. To emphasize that point, the evaluation board for the tri-axial magnetic field sensor from PNI Corp. was pointed toward north as accurately as possible, as shown in Figure 5.17. Then, yaw measurements were also taken, given the same orientation after placing a cast iron handle near the sensor, as shown in Figure 5.18. Furthermore, the same experiments was repeated but after replacing the iron handle with a conventional wrist watch, as shown in Figure 5.19, to simulate a probable situation during a rehabilitation session.

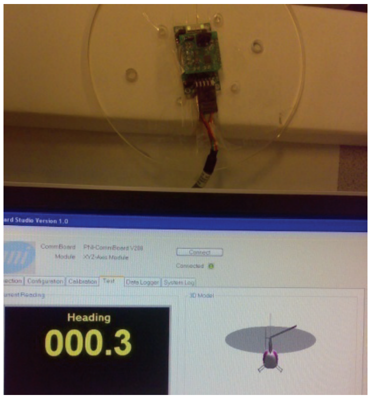

Figure 5.17: Heading angle without hard-iron disturbances

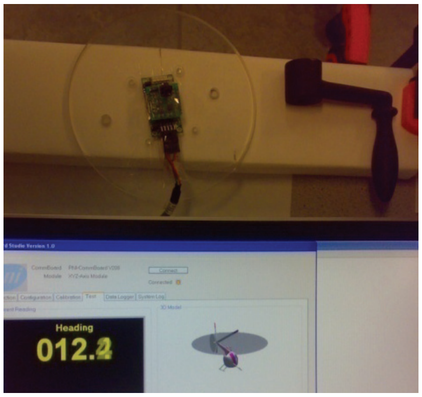

Figure 5.18: Heading angle with hard-iron disturbances (iron handle)

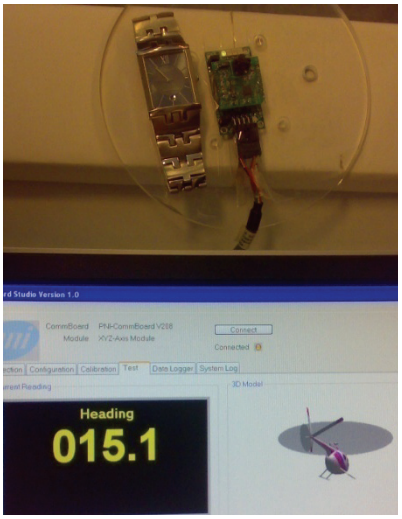

Figure 5.19: Heading angle with hard-iron disturbances (wrist watch)

Results showed that the heading angle was affected to nearly $12^0$ in the case of the iron handle and $15^0$ in the case of the wrist watch. These results show that compensating for magnetic disturbances is a must, a point mentioned in recommendations for future work.

Furthermore, dynamic orientation tests had to be made to verify the performance of the EKF algorithms discussed in Chapter 3. At first, the implemented sensor module was mounted on top of the GX-2 reference orientation sensor as shown in Figure 5.20 to start the acquisition, data-logging and verification of the unit under test (UUT). After that, both sensor modules were moved randomly by hand to ensure non linearity of orientation.

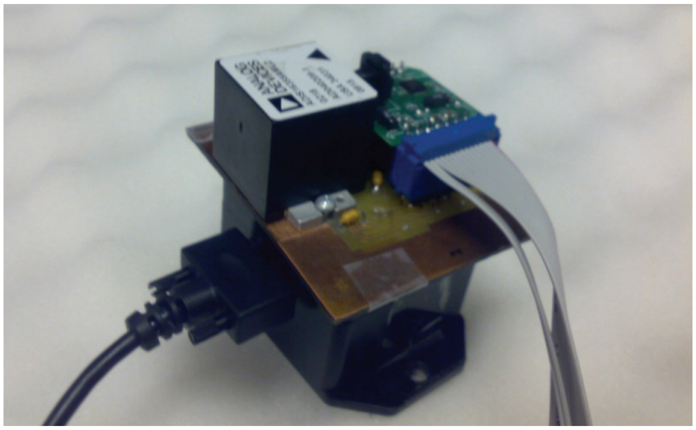

Figure 5.20: Implemented sensor mounted on reference sensor

Having different sampling rates of both modules introduced a major challenge during comparison between their data. The solution to that problem was introduced by having the data logging software (i.e. LabVIEW) poll the GX-2 orientation data after each packet received by the implemented sensor module. In this case, data from both systems was almost perfectly synchronized.

## 5.4 Position Validation Test Setup

Position validation data was produced using the biomechanical model compared with a real-time state-of-the-art visual motion tracking system (Visualeyez from Phoenix Technologies Inc.) seen in Figure 5.21. The vision tracking system is composed of three cameras to perform triangulation and provide the position of active markers mounted on the target body.

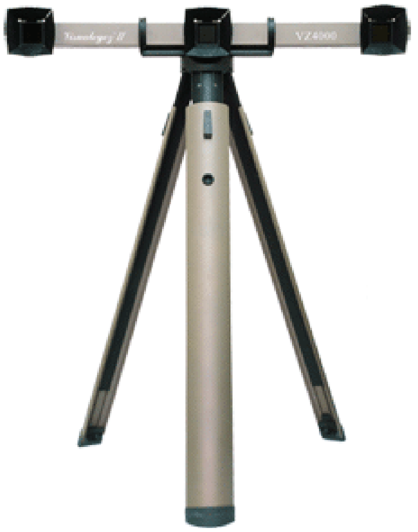

Figure 5.21: Visualeyez motion tracking system by Phoenix Technologies

The active vision system markers were first placed as shown in Figure 5.22. The first three markers shown on the left of the picture form the coordinate reference frame (CRF). However, since the system doesn't allow setting real-time CRF markers unless they are more than 10 cm apart, their position data was first logged, and then the CRF was created before data logging.

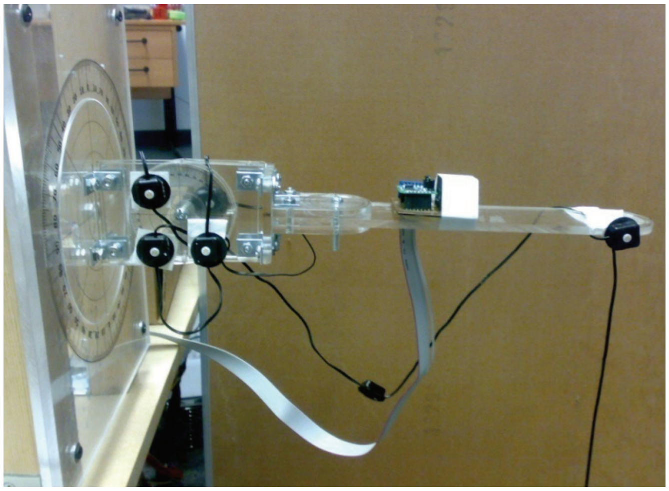

Figure 5.22: Active markers placed on the arm model for position validation

During the data acquisition/logging, the sampling time synchronization problem was faced like the one faced with the Microstrain's GX-2 sensor. However, this problem was partially solved by setting the vision system to start capturing data using an external trigger and maintain a sampling rate of 17 Hz. Nevertheless, since the implemented module sampling rate was not exactly 17 Hz, this generated some time shifting error as can be seen in the experimental results of Chapter 4.

Dynamic motion experiments rotating about the sensor's y-axis (i.e. pitch) and the z-axis (i.e. yaw) were implemented as shown in Figure 5.23 and Figure 5.24. The main goal of these motions was to log the position of the elbow marker seen mounted at the tip of the artificial arm model in Figure 5.23 and compare it with the output of the position calculation algorithms from the biomechanical model. A last positioning test was made to combine 3D rotations (roll, pitch and yaw), but unfortunately it was not successful because only one vision tracker was available at the time of experiment that lead to the occurrence of  losses of line-of-sight.

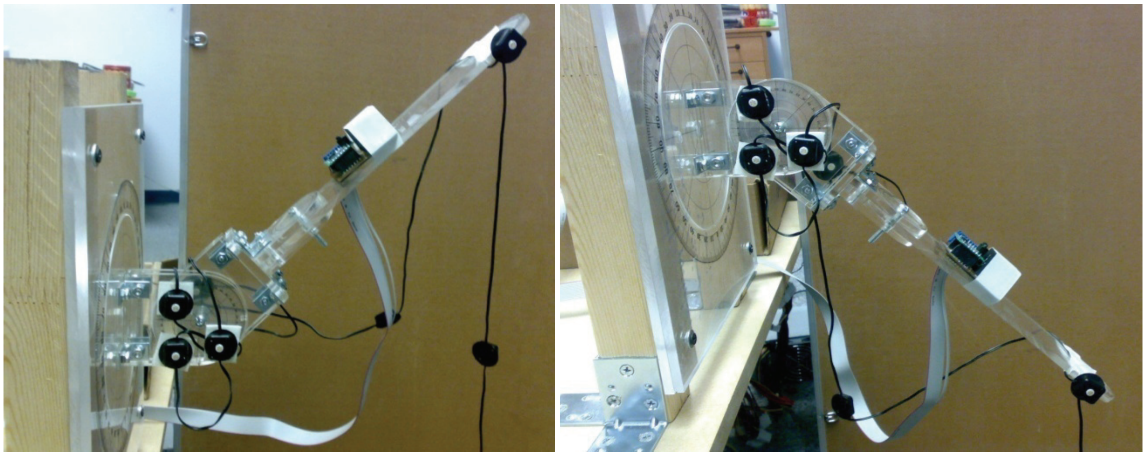

Figure 5.23: Pitch motion positioning validation test

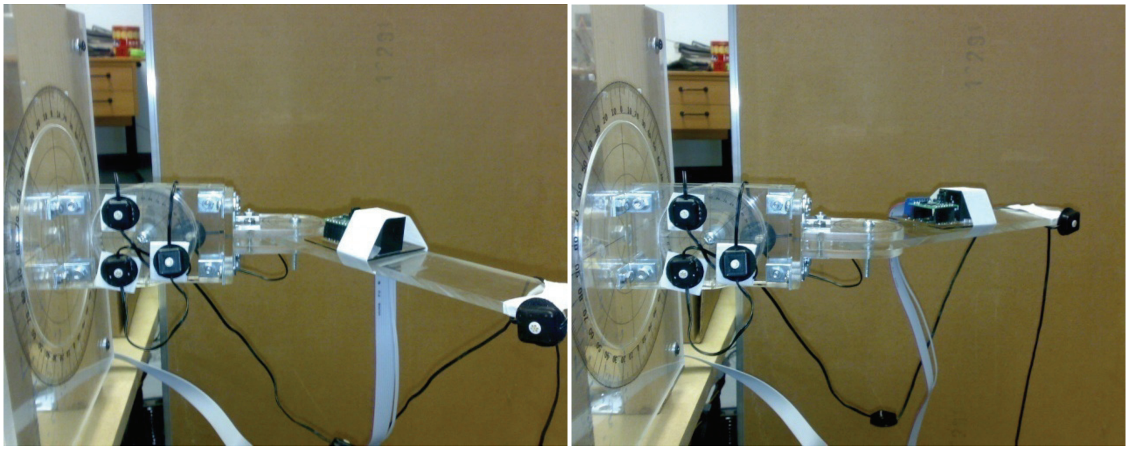

Figure 5.24: Yaw motion positioning validation test

Position comparison results showed that the position of the elbow given by the vision system had slight offsets due to the placement errors of the markers forming the reference frame. This formed misalignment errors for the position tracking. These fixed misalignment errors were manually subtracted later from the results before comparing to the implemented inertial sensor module.

# Chapter 6: CONCLUSION AND FUTURE WORK

## 6.1 Conclusion

In this thesis, the main objective was to characterize the human arm motion using kinematics for rehabilitation monitoring. The approach taken towards achieving that objective was to use a biomechanical model of the human arm accompanied with inertial sensors to estimate joint angles and positions of points of interest on the arm. As stated earlier, these motion parameters  can be further used for comparing saved exercise trajectories with the ones performed by the rehabilitation subjects.

To obtain the joint angles, two Extended Kalman Filters algorithms were studied and implemented. The first EKF. sensor fusion algorithm was used to estimate Euler angles. The corresponding experiments showed conveniently accurate results in the Roll and Pitch angles. However, a drawback of the developed Euler angles estimator is its high vulnerability to external magnetic interferences as well as singularities. The second EKF. algorithm (Quaternion-based EKF) was designed to overcome the disadvantages of the Euler-based one. Singularity problems were solved by using quaternions instead of Euler angles to describe orientation. Furthermore, its complementary nature – it concentrates on estimating the errors of the states not the states themselves – gave it more immunity to external interferences.

The biomechanical model of the human arm assumes a simplified five-degrees-of-freedom structure of the arm. Furthermore, three forward kinematics algorithms were studied and compared to obtain the human arm's 3D position. First, mathematical simulations were performed to compare performances of the DH and the DQ algorithms. Results showed that the dual quaternion method is faster than the DH homogenous transformation, especially for high degrees-of-freedom systems. Finally, the joint angles governing the model were later taken from the outputs of the EKF. estimators.

Although the yaw angle estimation showed high performance dependency on the surrounding electromagnetic disturbances, the complete system (orientation and local positioning) showed consistency over time. The advantage of stability of the estimated information can exceed the importance of highly accurate systems only stable for tens of seconds. Another notable aspect is that the objectives of the research include providing data for comparison of 3D trajectories using Artificial Intelligence in future work, not determination of trajectories themselves.

In addition, the proposed system algorithms and implementation can be used efficiently for stroke rehabilitation monitoring and assessment based on the human arm kinematic information (i.e. 3D-position, joint-angles, etc…). The system can also be further modified to include dynamical data such as velocities and accelerations of the given points of interest. Other advantages of the system are the relatively low total cost, low power consumption, and portability – it is battery-powered and wireless.

## 6.2 Future Work and Recommendations

Future work planned for this research includes implementing soft and hard iron interference compensation for the magnetometers. Such compensation is needed for indoor environments such as clinics, hospitals, and homes, where the magnetic interferences are generally unknown.

Extending the number of sensor nodes to cover the human body should be researched. In this area, general human body rehabilitation can be monitored and assessed by studying motion of any given body part at any given time. Moreover, having the coordinate reference frame as dynamic (i.e. fixed on the body not NED frame) would facilitate relative positioning of the points of interest in 3D space. This can be easily done by describing position of the points with respect to a chosen frame of a sensor as shown in Chapter 4.

Another way to contribute significantly to the rehabilitation field is introducing the kinematics data to artificial intelligence algorithms (Neural Networks, Fuzzy Logic, Combined Neuro-Fuzzy, etc…) for trajectory pattern recognition. This capability can be developed to compare the results of various exercises performed by rehabilitation subjects.

Finally, it is recommended that an interactive graphical user-friendly interface be designed in a video-gaming theme. This development would strongly encourage rehabilitation patients to perform their recommended exercises actively.

# APPENDICES

## Appendix A: ADIS 16350 Inertial Sensor Specifications

| Parameter | Condition | Typical Value |
|---|---|---|
| Gyro-sensitivity | 25°C, dynamic range = ±300 °/s<br>Sensitivity Vs Temperature at 25°C | 0.07326 °/s/LSB<br><1% |
| Gyro-Bias | Bias Vs Temp. at 25°C | <4% |
| Gyro-axis non-orthogonality | Different from 90° ideal at 25°C | ± 0.05° |
| Gyro-axis misalignment | Relative to base plate and guide pins at 25°C | ± 0.5° |
| Gyro-freq. response (3dB) | Bandwidth<br>Sensor Resonant Freq. | 350 Hz<br>14 kHz |
| Accelerometer | dynamic range<br>initial | ±10 g<br>25 m*g*/LSB |
| Accelerometer-axis non-Orthogonality | Different from 90° ideal at 25°C | ± 0.25° |
| Accelerometer-axis misalignment | Relative to base plate and guide pins at 25°C | ± 0.5° |
| Accelerometer in-Run bias stability | 1σ at 25°C<br>Velocity random walk at 25°C | 0.7 m*g*<br>2 m/s/$\sqrt{h}$ |
| Accelerometer-temperature coefficient |  | 4 m*g*/°C |
| Accelerometer - frequency response (3dB) | Bandwidth<br>Sensor Resonant Freq. | 350 Hz<br>10 kHz |

## Appendix B: PNI MicroMag-3 Magnetic Sensor Specifications

| Parameter | Condition | Typical Value |
|---|---|---|
| Power Consumption | 3VDC | <500 μA |
| Magnetic Field Measurement Range | | ± 1100 μT<br>± 11 Gauss |
| Resolution | 1/Gain (μT) | 0.015 μT<br>0.00015 Gauss |
| Sampling Rate | 3 VDC | Up to 2000 sample/sec |
| Linearity | Error from best fit straight line at ±300 μT | 1% |
| Sensor Frequency | 3VDC, $R_b$=43Ω within earth's magnetic field | 175 KHz |
| Operating Temperature | | -20 to 70 C |

# REFERENCES

[1] Canadian Institute for Health Information (CIHI), "Average admission, discharge and change in total function scores of inpatient rehabilitation clients by RCG," CIHI, Canada, Tech. Rep. NSR309, 2008.

[2] A. Ramchandani, K. Carroll, R. Buenaventura, J. Douglas and Justin Liu. (2008, Wii-habilitation increases participation in therapy. *Virtual Rehabilitation, 2008* pp. 69-69.

[3] P. POUND, M. BURY and S. EBRAHIM. (1997, /9/1). From apoplexy to stroke. *Age Ageing 26(5),* pp. 331-337. Available: http://ageing.oxfordjournals.org

[4] World Health Organization, *Cerebrovascular Disorders: A Clinical and Research Classification.* ,1st ed.Geneva: WHO, 1979, pp. 82.

[5] J. L. M. Christopher and D. L. Alan, "Mortality by cause for eight regions of the world: Global Burden ofDisease Study," *The Lancet,* vol. 349, pp. 1269, 1997.

[6] r. A. D. Geoff, F. Marc, M. Malcolm and M. D. Stephen, "Stroke," *The Lancet,* vol. 371, pp. 1612, 2008.

[7] L. Oujamaa, I. Relave, J. Froger, D. Mottet and J. -. Pelissier, "Rehabilitation of arm function after stroke. Literature review," *Annals of Physical and Rehabilitation Medicine,* vol. 52, pp. 269, 2009.

[8] G. Prange, T. Krabben, B. Molier, H. van der Kooij and M. Jannink. (2008, A low-tech virtual reality application for training of upper extremity motor function in neurorehabilitation. *Virtual Rehabilitation, 2008* pp. 8-12.

[9] P. H. Wilson, J. Duckworth, N. Mumford, R. Eldridge, M. Guglielmetti, P. Thomas, D. Shum and H. Rudolph. (2007, A virtual tabletop workspace for the assessment of upper limb function in traumatic brain injury (TBI). *Virtual Rehabilitation, 2007* pp. 14-19.

[10] M. S. Cameirao, S. Bermudez i Badia, E. D. Oller and P. F. M. J. Verschure. (2008, Using a multi-task adaptive VR system for upper limb rehabilitation in the acute phase of stroke. *Virtual Rehabilitation, 2008* pp. 2-7.

[11] S. Attygalle, M. Duff, T. Rikakis and Jiping He. (2008, Low-cost, at-home assessment system with wii remote based motion capture. *Virtual Rehabilitation, 2008* pp. 168-174.

[12] S. Balasubramanian, Ruihua Wei, M. Perez, B. Shepard, E. Koeneman, J. Koeneman and Jiping He. (2008, RUPERT: An exoskeleton robot for assisting rehabilitation of arm functions. *Virtual Rehabilitation, 2008* pp. 163-167.

[13] B. Dellon and Y. Matsuoka. (2008, Feedback distortion to augment controllability of human limb motion. *Virtual Rehabilitation, 2008* pp. 22-27.

[14] P. Pyk, D. Wille, E. Chevrier, Y. Hauser, L. Holper, I. Fatton, R. Greipl, S. Schlegel, L. Ottiger, B. Ruckriem, A. Pescatore, A. Meyer-Heim, D. Kiper and K. Eng. (2008, A paediatric interactive therapy system for arm and hand rehabilitation. *Virtual Rehabilitation, 2008* pp. 127-132.

[15] H. Zhou, T. Stone, H. Hu and N. Harris. (2008, 1). Use of multiple wearable inertial sensors in upper limb motion tracking. *Med. Eng. Phys. 30(1),* pp. 123-133.

[16] G. Lanfermann, R. Willmann, J. Te Vrugt, A. Timmermans, E. Bongers, N. Lambert and V. Van Acht, "Philips stroke rehabilitation exerciser," in 2007,

[17] H. Junker, O. Amft, P. Lukowicz and G. Tröster. (2008, 6). Gesture spotting with body-worn inertial sensors to detect user activities. *Pattern Recognit 41(6),* pp. 2010-2024.

[18] D. Roetenberg, P. J. Slycke and P. H. Veltink. (2007, Ambulatory position and orientation tracking fusing magnetic and inertial sensing. *Biomedical Engineering, IEEE Transactions on 54; 54(5),* pp. 883-890.

[19] H. Zheng, N. Black and N. Harris. (2005, 08/28). Position-sensing technologies for movement analysis in stroke rehabilitation. *Medical and Biological Engineering and Computing 43(4),* pp. 413-420. Available: http://dx.doi.org/10.1007/BF02344720

[20] E. Foxlin, "Motion tracking requirements and technologies," in *Handbook of Virtual Environment Technology* ,1st ed., vol. 1, K. Stanney, Ed. Lawrence Erlbaum Associates, CRC Press, 2002, pp. 163.

[21] Crossbow Technologies, "Theory of operation of angular rate sensors (application note)," Crossbow Technologies,

[22] J. Geen and D. Krakauer, "New iMEMS Angular-Rate-Sensing Gyroscope," *Analog Devices Dialogue,* vol. 37, pp. 12, March 2003. 2003.

[23] Analog Devices. (2008, February, 2008). ADIS16350/ADIS16355 high precision tri-axis inertial sensor data sheet (rev. A). ADI, Available: http://www.analog.com/static/imported-files/data_sheets/ADIS16350_16355.pdf

[24] D. Simon, "Non linear kalman filtering," in *Optimal State Estimation Kalman, H-Infinity and Nonlinear Approaches* ,1st edition ed., vol. 1, Anonymous USA: Wiley-Interscience, 2006, pp. 395.

[25] H. Weinberg. (1999, Dual axis, low *g,* Fully integrated accelerometers. Analog Devices,

[26] B. L. Stevens and F. L. Lewis, *Aircraft Control and Simulation.* ,2nd ed.USA: Wiley-Interscience, 2003, pp. 680.

[27] E. Bekir, *Introduction to Modern Navigation Systems.* Singapore: World Scientific Publishing Company, 2007, pp. 256.

[28] PNI Corp., "PNI-11096 3-axis magneto-inductive sensor driver and controller with SPI serial interface," PNI Corp., Tech. Rep. 07, February, 2003, 2003.

[29] D. Gebre-Egziabher, G. H. Elkaim, J. D. Powell and B. W. Parkinson. (2000, A gyro-free quaternion-based attitude determination system suitable for implementation using low cost sensors. *Position Location and Navigation Symposium, IEEE 2000* pp. 185-192.

[30] A. J. Hanson, *Visualizing Quaternions.* ,1st ed., vol. 1, Canada, US: Morgan Kaufmann, 2006, pp. 600.

[31] A. M. Sabatini. (2006, Quaternion-based extended kalman filter for determining orientation by inertial and magnetic sensing. *Biomedical Engineering, IEEE Transactions on 53; 53(7),* pp. 1346-1356.

[32] D. Roetenberg, H. J. Luinge, C. T. M. Baten and P. H. Veltink. (2005, Compensation of magnetic disturbances improves inertial and magnetic sensing of human body segment orientation. *Neural Systems and Rehabilitation Engineering, IEEE Transactions on 13; 13(3),* pp. 395-405.

[33] H. Arisawa, T. Sato and T. Tomii. (2002, Human-body motion simulation using bone-based human model and construction of motion database. *Conceptual Modeling for New Information Systems Technologies* pp. 115-126. Available: http://dx.doi.org/10.1007/3-540-46140-X_10

[34] T. Harada, T. Gyota, Y. Kuniyoshi and T. Sato. (2007, Development of wireless networked tiny orientation device for wearable motion capture and measurement of walking around, walking up and down, and jumping tasks. *Intelligent Robots and Systems, 2007. IROS 2007. IEEE/RSJ International Conference on* pp. 4135-4140.

[35] S. Kurata, M. Makikawa, H. Kobayashi, A. Takahashi and R. Tokue. (1998, Joint motion monitoring by accelerometers set at both near sides around the joint. *Engineering in Medicine and Biology Society, 1998. Proceedings of the 20th Annual International Conference of the IEEE 4; 4*pp. 1936-1939 vol.4.

[36] K. Abdel-Malek, Z. Mi, J. Yang and K. Nebel. (2006, Optimization-based trajectory planning of the human upper body. *Robotica 24(06),* pp. 683. Available: http://journals.cambridge.org/action/displayAbstract?fromPage=online&aid=534704&fulltextType=RA&fileId=S0263574706002852RD 2006

[37] M. Treiber, "Dynamic Capture of Human Arm Motion using Inertial Sensors and Kinematical Equations," 2004.

[38] J. Lenarcic and A. Umek. (1994, Simple model of human arm reachable workspace. *Systems, Man and Cybernetics, IEEE Transactions on 24; 24(8),* pp. 1239-1246.

[39] J. J. Craig, *Introduction to Robotics: Mechanics and Control.* ,3rd ed.Prentice Hall, 2004, pp. 408.

[40] N. A. Aspragathos and J. K. Dimitros. (1998, A comparative study of three methods for robot kinematics. *Systems, Man, and Cybernetics, Part B: Cybernetics, IEEE Transactions on 28; 28(2),* pp. 135-145.

[41] J. McCarthy, "Dual quaternions," in *Introduction to Theoritical Kinematics* P. Denning, Ed. The MIT Press, 1990, pp. 62.

[42] J. K. Davidson and K. H. Hunt, "Describing the screw," in *Robots and Screw Theory: Applications of Kinematics and Statics to Robotics* Anonymous USA: Oxford University Press, 2004, pp. 23.

[43] J. Kim and V. Kumar. (2007, 22 March 2007). Kinematics of robot manipulators via line transformations. *Journal of Robotic Systems 7(4),* pp. 649.

[44] H. H. Cheng. (1994, 12/01). Programming with dual numbers and its applications in mechanisms design. *Engineering with Computers 10(4),* pp. 212-229. Available: http://dx.doi.org/10.1007/BF01202367